

Numerical modelling of a gas diffusion-based CO₂ electrolyser with flowing catholyte

MSc Thesis report

V. Konderla



Numerical modelling of a gas diffusion-based CO₂ electrolyser with flowing catholyte

MSc Thesis report

by

V. Konderla

to obtain the degree of Master of Science
at the Delft University of Technology,
to be defended publicly on Wednesday January 24, 2022 at 13:30.

Student number: 5145511
Project duration: January 11, 2021 – January 24, 2022
Thesis committee: Dr. ir. D. A. Vermaas, TU Delft, supervisor
Prof. dr. ir. J. T. Padding, TU Delft
Dr. ir. J. W. Haverkort, TU Delft

An electronic version of this thesis is available at <http://repository.tudelft.nl/>.

Abstract

Electrochemical CO₂ reduction may present a solution to close the carbon cycle and to utilise CO₂ emissions. However, for this technology to have a significant impact, it has to be successfully implemented on an industrial scale. Numerical simulations can aid with the study of process parameters and reactor design. To date, several numerical models describing CO₂ electrolyzers have been developed. Most numerical studies focus on mass transfer phenomena and electrochemical reactions in the catalyst layer (CL). Most recently, a model of a 2D electrolyser with a partially flooded CL investigated the relationship between local pH, current density distribution, and gas flow rate on the single pass conversion of CO₂ and the faradaic efficiency for the product CO. However, this study did not consider a fully flooded CL, which might be a more realistic assumption for the conditions in an electrolyzer. Further, most numerical models only focus on a length scale of tens of mm.

The overall aim of this project is to develop and utilise a numerical model that can describe phenomena arising in the flooded CL. First, the general operation of the electrolyser is addressed, and this is extended for the effect of liquid flow rate, electrolyser length, and operating pressure. To investigate the performance and limitations arising at the large-scale, the model is scaled-up to describe a one meter long electrolyser. The study is concluded with two considerations that could improve the electrolyser performance. These points were addressed by developing a numerical model of a gas diffusion-based CO₂ electrolyser in COMSOL Multiphysics. To investigate the effect of electrolyser length and to include variations arising from the fluid flow, the model was developed in 2D. We assessed the performance of the electrolyser in terms of current density, reflecting rate of species formation, and of faradaic efficiency for CO (FE), reflecting selectivity towards the desired product.

Investigating the small-scale electrolyser we find that at high current density (200 mA cm⁻²), the pH in the CL immediately increases by 3 units and further diagonally increases from pH 10.1 the inlet to 12.2 around the outlet. When operating the electrolyser with excess of CO₂ supply, we find the CL to perform the best near the gas phase boundary (311 mA cm⁻², 95% FE), while the regions close to the electrolyte are underperforming (250 mA cm⁻², 89% FE). This shows that the performance in certain regions of the CL needs to be improved.

When scaling-up the electrolyser to a length of one meter we find that the performance does not change dramatically when operating at excess of gas supply. However, if a high CO₂ conversion should be achieved, the long electrolyser shows a 10% decrease in FE, and CO₂ conversion compared to a small-scale electrolyser, at the same level of current density (115 mA cm⁻²). Analysing the current density locally, we find that difference between the inlet and outlet can be as large as 100 mA cm⁻². Next, we find that FE can fall to almost 50% around the outlet. This shows that when adding extra length to the long electrolyser, this extra length only adds a fraction of its potential performance.

The uneven utilization of the catalyst can be improved by varying the catalyst loading along the electrolyser length. This improves the FE by around 5% while using 40% less catalyst. We also find that while the current density is slightly lower, the amount of product generated per mass of catalyst has significantly increased. This shows that carefully engineering the catalyst loading can save the amount of catalyst needed and could potentially improve the cost-effectiveness of the CO₂ electrolyser.

In all cases the performance over the CL is unevenly distributed. To achieve a higher performance, research needs to find ways how to enhance the performance also in the poorly utilised regions of the CL. Scaling-up the electrolyser just by extending its length proves inefficient and inevitably leads to a lower performance. The beneficial buffering effect provided by the electrolyte at small-scale does not translate to a large-scale. Research needs to find alternative ways how to effectively scale-up the electrolyser. At this moment, performance of large-scale CO₂ electrolyzers seem satisfactory only when operating at very low CO₂ conversion. From the investigated parameters that address the performance issues, higher operating pressure and smart catalyst loading seem only promising options, however, other options should be found to speed up the development.

Contents

1	Introduction	1
2	Theory	3
2.1	On electrochemical CO ₂ reduction	3
2.2	Possible configurations of the CO ₂ electrolyser.	3
2.3	Technological requirements for economic feasibility	5
2.4	Description of the modelled electrolyser.	6
2.5	Theoretical background of electrochemical CO ₂ reduction.	7
2.5.1	Cathodic half-cell	7
2.5.2	Anodic-half cell	8
2.5.3	Homogeneous reactions in the liquid phase	9
2.6	Recent development in the CO ₂ electrolyser modelling	9
2.7	Research question	13
3	Methodology	15
3.1	Fundamental considerations	15
3.2	Governing equations	16
3.2.1	Species transport in the gaseous phase	16
3.2.2	Species transfer through the gas/liquid interface	19
3.2.3	Species transport in the liquid phase	21
3.2.4	Homogeneous reactions in the liquid phase	22
3.2.5	Electrochemical reactions	23
3.2.6	Charge-transfer.	25
3.2.7	Gas flow inside the gas diffusion layer	26
3.2.8	Electrolyte and gas velocity profile.	26
3.3	Model development and description.	29
3.3.1	Boundary conditions	29
3.3.2	Model parameters	29
3.3.3	Initial values.	29
3.3.4	Optional solver configurations	31
3.3.5	Solver configuration	31
3.3.6	Solver configuration for CO ₂ electrolyser with 1 m length	35
3.4	Quantifying electrolyser performance	36
3.5	Approach to answering the research question	37
4	Results and Discussion	41
4.1	Model validation	41
4.1.1	Numerical and analytical/empirical predictions	43
4.2	Phenomena governing the electrolyser performance.	44
4.2.1	Behaviour at low current density < 10 mA cm ⁻²	45
4.2.2	Behaviour at higher current density > 10 mA cm ⁻²	45
4.2.3	Local salting-out effect	49
4.3	Parametric study	51
4.3.1	Liquid flow rate	51
4.3.2	Electrolyser length	53
4.3.3	Operating pressure.	54

4.4	CO ₂ electrolyser with 1 m length	56
4.4.1	Overall performance	56
4.4.2	Performance within the catalyst layer	57
4.4.3	Produced gas mixture	59
4.4.4	Understanding the reduction in performance	59
4.5	Strategies to improve the performance of long electrolysers	63
4.5.1	Fluid flow configuration	63
4.5.2	Variable catalyst loading	64
5	Conclusion	67
6	Recommendations	69
	Bibliography	73
A	Initial values	75
B	Optional solver configurations	77
C	Model validation	81
C.1	1D model	81
C.2	Long electrolyser	83
C.2.1	Numerical and analytical predictions	84
D	Supporting results	85
D.1	Phenomena governing the electrolyser performance.	85
D.1.1	Behaviour at higher current density > 10 mA cm ⁻²	85
D.1.2	Local salting-out effect	86
D.2	Parametric study	87
D.2.1	Liquid flow rate	87
D.2.2	Electrolyser length	88
D.2.3	Operating pressure	89
D.3	CO ₂ electrolyser with 1 m length	90
D.3.1	Reaching high single pass conversions	91
D.4	Strategies to improve the performance of long electrolysers	92
D.4.1	Fluid flow configuration	92
D.4.2	Variable catalyst loading	93

Initialisms

BPM Bipolar membrane.

CL Catalyst layer.

COER CO evolution reaction.

FE Faradaic efficiency.

GDE Gas diffusion electrode.

GDL Gas diffusion layer.

HER H₂ evolution reaction.

MEA Membrane electrode assembly.

MPL Micro porous layer.

OER O₂ evolution reaction.

RHE Reversible hydrogen electrode.

Nomenclature

Electrochemistry

α	Transfer coefficient	–
η	Overpotential	V
η_a	Activation overpotential	V
j	Current density	mA cm ⁻²
ϕ_l	Electrolyte potential	V
ϕ_s	Electric potential	V
σ	Electrical conductivity	S m ⁻¹
σ^{eff}	Effective electrical conductivity	S m ⁻¹
FE	COER faradaic efficiency	–
FE ^{loc}	COER local faradaic efficiency	–
a_i	Activity of species i	mol m ⁻³
a_s	Specific area	m ⁻¹
E	Electrode potential	V
E^0	Standard reduction potential	V
E_{eq}	Equilibrium potential	V
F	Faraday's constant	C mol ⁻¹
i	Net current	mA
i_0	Exchange current	mA
j	Current density	mA cm ⁻²
j^{loc}	Local current density	mA cm ⁻²
j_0	Exchange current density	mA cm ⁻²
$j_{\text{COER}(y)}$	COER current density as a function of electrolyser length	mA cm ⁻²
j_{tot}	Total current density	mA cm ⁻²
n_e	Number of electrons exchanged in a charge-transfer reaction	–
r_{np}	Nanoparticle radius	m
z_i	Charge number of species i	–

Liquid phase

J_i	Diffusion molar flux of species i	mol m ⁻² s ⁻¹
N_i	Molar flux of species i	mol m ⁻² s ⁻¹

\mathbf{u}_i	Velocity of species i	m s^{-1}
\mathbf{u}	Molar average velocity	m s^{-1}
μ_l	Electrolyte dynamic viscosity	Pa s
\bar{u}	Average liquid velocity	m s^{-1}
\mathcal{D}_i	Diffusivity of species i in the solvent	$\text{m}^2 \text{s}^{-1}$
$\mathcal{D}_i^{\text{eff}}$	Effective diffusivity of species i in the solvent	$\text{m}^2 \text{s}^{-1}$
Pe	Péclet number	—
Re	Reynolds number	—
Sh	Sherwood number	—
c	Total concentration	mol m^{-3}
C_i	Logarithmic concentration of species i	—
c_i	Concentration of species i	mol m^{-3}
k	Rate constant of a homogenous reaction	
K_w	Equilibrium constant of water dissociation	$\text{mol}^2 \text{m}^{-6}$
r	Reaction rate of a homogeneous reaction	$\text{mol m}^{-3} \text{s}^{-1}$
R_i	Molar based rate of formation/consumption of species i per unit volume	$\text{mol m}^{-3} \text{s}^{-1}$
$R_{ct,i}$	Molar based rate of formation/consumption of species i per unit volume due to charge-transfer reactions	$\text{mol m}^{-3} \text{s}^{-1}$
$R_{h,i}$	Molar based rate of formation/consumption of species i per unit volume due to homogeneous reactions	$\text{mol m}^{-3} \text{s}^{-1}$
u_y	Velocity vector component in y direction	m s^{-1}
Gaseous phase		
κ^0	Permeability of a porous medium	m^2
κ^{eff}	Effective permeability of a porous medium	m^2
λ	Mean free path	m
\mathbf{J}_i^m	Diffusion mass flux of species i	$\text{kg m}^{-2} \text{s}^{-1}$
\mathbf{N}_i^m	Mass flux of species i	$\text{kg m}^{-2} \text{s}^{-1}$
\mathbf{v}_c	Correction velocity	m s^{-1}
\mathbf{v}	Mass average velocity	m s^{-1}
μ_g	Gas dynamic viscosity	Pa s
ω_i	Mass fraction of species i	—
\bar{u}_g	Average gas velocity	m s^{-1}
ρ	Total mass concentration	kg m^{-3}
ρ_i	Mass concentration of species i	kg m^{-3}
\mathcal{D}_i^m	Mixture-averaged diffusion coefficient of species i	$\text{m}^2 \text{s}^{-1}$

$\mathcal{D}_{i,j}$	Maxwell-Stefan diffusivity between species i and j	$\text{m}^2 \text{s}^{-1}$
$\mathcal{D}_{i,j}^{\text{eff}}$	Effective diffusivity between species i and j	$\text{m}^2 \text{s}^{-1}$
D_i	Combined diffusion coefficient of species i	$\text{m}^2 \text{s}^{-1}$
D_i^k	Knudsen diffusion coefficient of species i	$\text{m}^2 \text{s}^{-1}$
$j_{\text{COER,asmp}}$	Assumed COER current density	mA cm^{-2}
M_n	Mass-averaged molar mass	kg mol^{-1}
p	Relative pressure	Pa
p_{CO_2}	Partial pressure of CO_2	Pa
p_{abs}	Absolute pressure	Pa
R_i^m	Mass based rate of formation/consumption of species i per unit volume	$\text{kg m}^{-3} \text{s}^{-1}$
$u_{y,g}$	Velocity vector component in y direction	m s^{-1}
x_i	Molar fraction of species i	—
$X_{\text{CO}_2,\text{asmp}}$	Assumed CO_2 conversion	—
X_{CO_2}	CO_2 conversion	—
Gas/liquid interface		
$\Delta_{\text{sol}}H_{\text{CO}_2}$	Enthalpy of CO_2 dissolution	J mol^{-1}
c_g	Gas solubility in salt solution	kmol m^{-3}
c_s	Salt concentration	kmol m^{-3}
$c_{g,0}$	Gas solubility in pure water	kmol m^{-3}
$c_{i g/l}$	Concentration of species i at gas/liquid interface	mol m^{-3}
d_p	Pore diameter	m
h_i	Ion specific parameter in Schumpe equation	$\text{m}^3 \text{kmol}^{-1}$
h_T	Gas specific parameter in Schumpe equation	$\text{m}^3 \text{kmol}^{-1} \text{K}^{-1}$
H_{CO_2}	Henry's constant for CO_2	$\text{mol m}^{-3} \text{Pa}^{-1}$
$h_{G,0}$	Gas specific parameter in Schumpe equation	$\text{m}^3 \text{kmol}^{-1}$
$J_{\text{CO}_2 g/l}$	Normal component of the molar flux of CO_2 through gas/liquid interface	$\text{mol m}^{-2} \text{s}^{-1}$
K	Sechenov constant	$\text{m}^3 \text{kmol}^{-1}$
K_s	Sechenov constant for a salt s	$\text{m}^3 \text{kmol}^{-1}$
k_{CO_2}	Mass transfer coefficient of CO_2	m s^{-1}
n_i	Index of ion i in the formula of the salt	—
Others		
\mathbf{n}	Unit vector normal to a boundary	—
ϵ	Porosity	—
ν_i	Stoichiometric coefficient of species i	—

τ	Tortuosity	–
L	Electrolyser length	m
M_i	Molar mass of species i	kg mol ⁻¹
R	Universal gas constant	J mol ⁻¹ K ⁻¹
T	Temperature	K
t	Time	s
W	Width of a domain	m
Z	Out of plane size of the electrolyser	

Introduction

Since the start of the industrial revolution, the concentration of CO₂ in the atmosphere has been steadily rising, trapping the solar energy in the Earth's vicinity and causing the planet to warm up. This change in climate can have vast consequences, most notably including the need for agricultural adjustments, especially challenging for developing regions; increasing amounts of secondary pollutants in urban environments, more frequent natural disasters, spread of diseases such as malaria or cholera to the world's temperate zones, and more. In an effort to reduce the impact of climate change, the global societal trend is to shift to more sustainable technologies and reduce the increasing CO₂ and other greenhouse gas emissions.^{1,2}

CO₂ emissions primarily originate from the combustion of fossil fuels,¹ and they are still expected to be the main source of energy in upcoming years. The reason for this is found in the chemical industry and transportation.³ In the chemical sector, fossil fuels are often used as feedstock, for example in the production of plastics. In air and heavy-duty transportation, hydrocarbons are used as fuels. Finding a suitable alternative is in both cases very challenging.^{4,5}

One possible solution to some of the addressed problems is CO₂ capture and subsequent utilisation. CO₂ can be captured from the air or directly from point sources of pollution. Using renewable electricity, CO₂ can then be converted to value-added chemicals in CO₂ electrolyzers. Products of the electrolyser can serve, for example, as feedstock in the chemical industry. Additionally, with the increasing deployment of wind and solar energy sources, fluctuations in the power supply can be expected and thus the energy storage technology must improve. Products of CO₂ electrolyzers can also serve as large-scale and long-term seasonal energy storage where excess renewable energy is converted and stored in the form of chemical bonds. For these reasons, CO₂ electrolysis in combination with renewable electricity has the potential to reduce CO₂ emissions and dependence on fossil fuels. Furthermore, with the production of value-added chemicals, the technology can bring profit to the market.^{2,4,5}

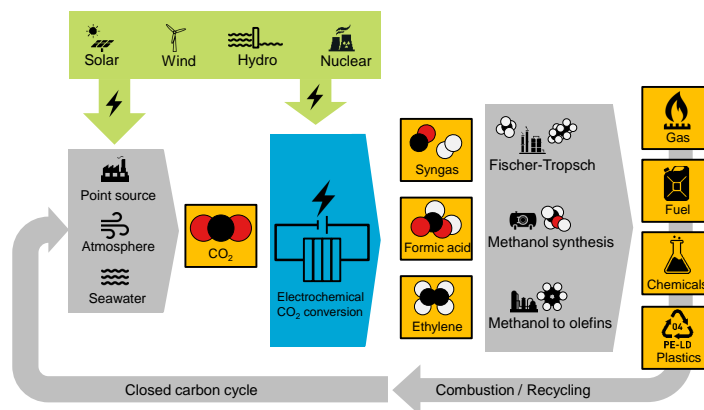


Figure 1.1: CO₂ conversion and utilisation with outlined closed carbon cycle. Schematic borrowed from Lorenz Baumgartner.

Figure 1.1 illustrates the above-outlined process. In the electrolyser, CO₂ can be converted to a variety of products such as CO, formic acid, or syngas where H₂ is obtained from water electrolysis or also from the CO₂ electrolyser. These products can then be optionally upgraded in mature industrial units, e.g. in Fischer-Tropsch synthesis,⁵ conveniently utilising existing processes without the need to build new ones. Subsequently, the industrial use of these products commonly results in the re-emission of CO₂ and when combined with CO₂ capture this can again provide the CO₂ for the electrolyser. This way the carbon cycle is closed.

Nevertheless, for this technology to have a significant impact on the future of energy systems and reduction of CO₂ emissions, it has to be successfully implemented on an industrial scale covering a non-negligible portion of the global energy system. However, up to today, no large-scale CO₂ electrolyser system has been deployed due to both technical and economical barriers. To make this technology feasible, literature reports minimum requirements in terms of cell voltage, current density, faradaic efficiency, and stability.²

Numerical modelling can be efficiently used to assess some of these metrics. Such models can also cost-effectively predict the performance of large-scale electrolysers. However, when delving into the literature we find that so far all these models focused only on length scales in order of tens of mm but non considered a large-scale model.⁶⁻¹² In this thesis project, we will try to fill in this missing piece. Before developing a large-scale model, we need to start at a small-scale. Most recently, Kas *et al.*⁶ published a numerical model on a gas diffusion-based CO₂ electrolyser with a partially flooded catalyst layer. In their study, authors elaborate on the distribution of current density, its relation to pH, gas flow, the concentration of buffer ions, and more. We aim to continue in the similar manner but focus on the flooded catalyst layer. Thereafter, using the same approach we aim to investigate the effect of different parameters and finally proceed to a large-scale model. The research questions can be summarized as follows.

- How is the pH, current density, and faradaic efficiency distributed inside the catalyst layer, and what shapes this distribution?
- How is the CO₂ solubility affected and can it influence the electrolyser performance?
- How does the electrolyser performance change with varying liquid flow rate, electrolyser length, and operating pressure?
- How does a large-scale electrolyser compare to a small-scale in terms of current density, faradaic efficiency, and CO₂ conversion? What limitations arise?
- Is it possible to improve the electrolyser performance by changing the fluid flow configuration or by varying the catalyst loading?

To answer these questions we aim to develop a numerical model using COMSOL Multiphysics. The model should be developed in 2D and it should correspond to the gas diffusion-based electrolyser. It should primarily focus on the phenomena occurring at the cathode.

With this thesis project, we hope to generate more understanding of the operation of CO₂ electrolyser. Knowing the distribution of different metrics inside the catalyst layer, we could identify the underperforming regions and indicate what should be optimized. Knowing the effect of different parameters, we could identify which parameters should be treated with priority and we could help to guide an experimental study. Knowing how the performance of a large-scale electrolyser changes, we could name these limitations and identify what needs to be improved. Knowing whether fluid flow arrangement or changing catalyst loading has any influence, we could try to indicate a direction which experimental research should take.

2

Theory

2.1. On electrochemical CO₂ reduction

In electrochemical CO₂ reduction up to 16 different products can be formed. However, only a few of these products are formed with considerably high selectivity. **Table 2.1** summarizes some of these products. Evolution of both CO and formate involves two electrons and can be performed with high selectivity. On the other hand, formation of multiple electron products is reported with a lower selectivity. Apart from CO₂ electroreduction, a competing reaction in the form of the hydrogen evolution reaction, HER, can occur at the cathode.^{2,3}

Table 2.1: Products of electrochemical CO₂ reduction with their common catalysts. Products shown here are reported to reach faradaic efficiency (section 2.3) over 50%. Standard potential, E^0 , for these reactions is provided vs RHE at 298.15 K^{3,5,13,14}

Catalyst	Reaction	Main product	E^0 [V]
Ag, Au	$\text{CO}_2 + \text{H}_2\text{O} + 2\text{e}^- \longrightarrow \text{CO} + 2\text{OH}^-$	CO	-0.11
Sn, In, Ti, Pb, Sn/Cu, SnO ₂	$\text{CO}_2 + \text{H}_2\text{O} + 2\text{e}^- \longrightarrow \text{HCOO}^- + \text{OH}^-$	HCOO ⁻	-0.02
Pd/SnO ₂ , ¹⁵ Mo/Bi ¹⁶	$\text{CO}_2 + 5\text{H}_2\text{O} + 6\text{e}^- \longrightarrow \text{CH}_3\text{OH} + 6\text{OH}^-$	CH ₃ OH	0.02
Cu	$2\text{CO}_2 + 8\text{H}_2\text{O} + 12\text{e}^- \longrightarrow \text{C}_2\text{H}_4 + 12\text{OH}^-$	C ₂ H ₄	0.07
CuO/Cu ₂ O	$2\text{CO}_2 + 9\text{H}_2\text{O} + 12\text{e}^- \longrightarrow \text{C}_2\text{H}_5\text{OH} + 12\text{OH}^-$	C ₂ H ₅ OH	0.08
Competing reaction	$2\text{H}_2\text{O} + 2\text{e}^- \longrightarrow \text{H}_2 + 2\text{OH}^-$	H ₂	0.00

The choice of catalyst determines which products of CO₂ electroreduction will be formed (**Table 2.1**). The choice of main product should be carefully assessed, taking into consideration both economical and technological aspects. Techno-economic analyses agree that with recent achievements in lab-scale electrolyzers, CO and formate are currently the most promising targets. Nevertheless, limited market size and difficulties connected to storage and transportation for both CO and formate make the production of ethylene, ethanol, or propanol more attractive. These could thus potentially achieve even higher economical yield. However, at present, the C₂+ carbon products are limited by the price of the electricity and more importantly, need considerable improvements in catalytic performance.^{2,3}

2.2. Possible configurations of the CO₂ electrolyser

Throughout the research history, different types of CO₂ electrolyzers were designed. Here, electrolyzers are divided into four main types (**Figure 2.1**). The depicted flow of reactants and products highlights electrolyzers' functionality.

Early reactor designs, referred to as H-cells (**Figure 2.1a**), are limited by the maximum achievable current density. These electrolyzers use liquid-liquid configuration. Gaseous CO₂ is firstly dissolved in the catholyte, then it diffuses through the electrolyte to the cathode surface. The typical diffusion pathway is on a scale of 50 μm. For this exact diffusion pathway, Burdyny *et al.*¹⁷ show that the upper limit in terms of current density towards CO₂ reduction is below 35 mA cm⁻². At higher current densities, CO₂ cannot diffuse to the electrode surface fast enough and the H-cell becomes limited by

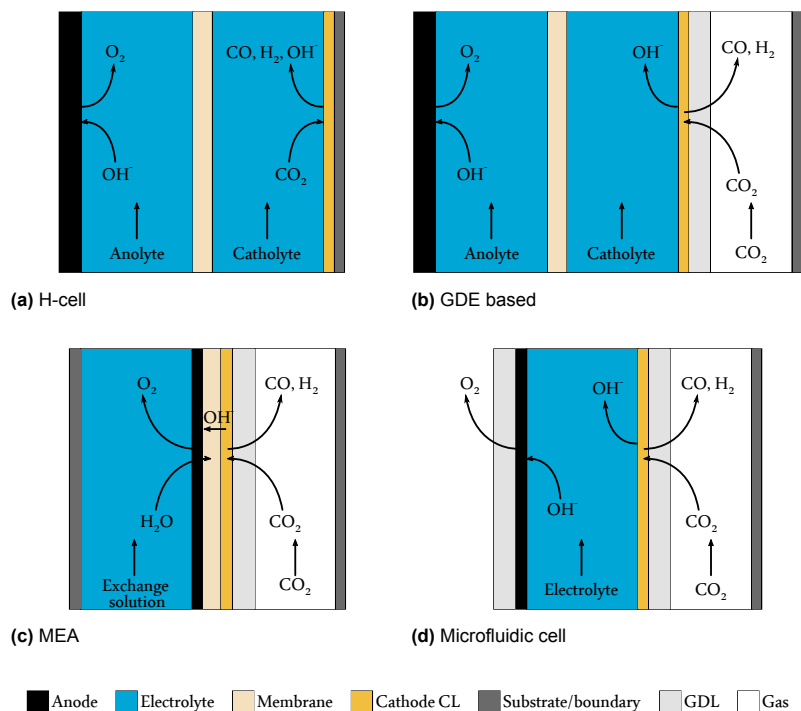


Figure 2.1: Overview of the different types of CO₂ electrolyzers as based on:^{2,14,17}

diffusion, i.e. mass transfer limited. If the current density were to be increased further, H₂ would be produced. Scale up of the H-cell electrolyser could thus be possible, but, due to the limited current density, uneconomical.^{2,17}

The next generation of CO₂ electrolyser aim to tackle the low current density achieved in H-cells. **Figure 2.1b** presents CO₂ electrolyzers, which utilize gas diffusion electrodes, GDE, and two flowing electrolytes. A schematic and the description of the operating principle of GDE are presented in **Figure 2.2**. The inherent advantage of a GDE is the reduction in diffusion path, which is now restricted only to the gas-liquid interface and thin electrolyte film. This diffusion path is scaled down from roughly the 50 μm in H-cell to about 50 nm in GDE based cell.¹⁷ Additionally, a GDE offers substantially more catalytically active sites than the planar electrodes. Consequently, GDE based design can achieve significantly higher current densities.^{2,9,17} The use of liquid electrolytes enables precise control of the reaction environment, but also presents a major drawback. Utmost, the two electrolytes are responsible for high ohmic losses. Next, the liquid electrolyte can cause instability as a result of impurity deposition on the catalyst surface or liquid penetration to the gas channel. Finally, using flowing electrolytes brings substantial complexity into this reactor design. Salt precipitation may also occur.² High ohmic loss can be partially avoided by placing the anolyte on the opposite side of the anode resulting in one of the possible modifications to this cell design.

To further decrease the cell potential, the distance between the electrodes should be decreased or the conductivity of the electrolyte increased. This is achieved in a membrane-electrode-assembly, MEA, design (**Figure 2.1c**). MEA is characterised by the removed electrolyte and membrane directly in contact with the cathode. This is known as zero-gap configuration. Various configurations exist. Configuration with an exchange solution provides the necessary humidity to the membrane. Alternatively, an exchange solution can be removed and humidity can be provided through the humidification of the gas stream. With the removal of the liquid electrolytes, the main advantages follow from the disadvantages of the previous design.² The ohmic overpotential can decrease by as much as 40%.¹⁰ Stability-wise, an MEA might be considered more stable, provided that the water management is well controlled. Water is required for the COER, however, too much water can result, for example, in GDE flooding. Flooded GDE then starts to favour HER.^{18,19} Some of the disadvantages reported in MEA electrolyzers include challenges in sustaining high selectivity and high current density at the same time, product crossover or precipitation of cations at higher current densities.^{2,10}

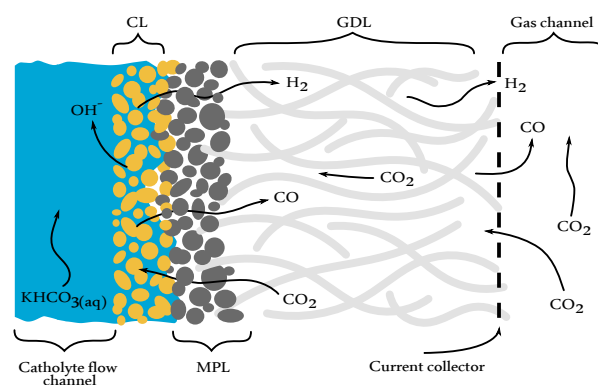


Figure 2.2: Schematic of GDE highlighting the operating principle. GDE comprises of catalyst layer, CL, microporous layer, MPL, and gas diffusion layer, GDL. Gaseous CO_2 is fed to the electrolyser via a gas channel. This CO_2 then diffuses through the GDL and MPL until reaching the CL. There, CO_2 reacts on the catalyst surface to produce CO. Another reaction often occurring at the catalyst surface is H_2 evolution. Then, the produced CO, or H_2 , diffuse through MPL and GDL and leave from the top of the gas channel together with unreacted CO_2 .

Another type of electrolyser that use GDE is referred to as microfluidic reactors (**Figure 2.1d**). These operate without the use of a membrane and utilize only a single electrolyte flow channel.²⁰ Without the membrane, the reactor design is simplified and the ohmic loss is reduced. However, the product crossover relies only on laminar electrolyte flow.² Similarly to the designs described above, a flowing electrolyte offers flexibility in operating conditions.²⁰ Among the disadvantages of the microfluidic reactor types belong its more complicated pressurising of reactants and products¹⁴ and more importantly, the complication of maintaining a laminar flow barrier when scaling up the electrolyser.²

2.3. Technological requirements for economic feasibility

Techno-economic analyses set minimum requirements for the CO_2 electrolyser to become economically feasible. The electrolyser feasibility can be assessed based on current density, FE, cell voltage, and stability. Keeping these metrics in consideration, we can at the end of this project discuss how well the current laboratory electrolyser stand in comparison to these requirements.

Current density

Current density reflects the intensity of product formation normalized to the geometrical, i.e. visible, surface area. Current density thus governs the capital cost of the electrolyser. With a higher current density the electrolyser can be made smaller, and thus cheaper, while maintaining the same production rate.² Most of the studies agree that the current density should be higher than 200 mA cm^{-2} .^{3,17} Some studies even reporting minimum current density of 300 mA cm^{-2} or 400 mA cm^{-2} .^{2,4}

Faradaic efficiency

FE is defined as a ratio between the charge consumed in the formation of the desired product to the total charge supplied. FE reflects product selectivity. Higher FE thus reduces total current needed. In the downstream processing, higher purity of the main product decreases the separation cost. FE of at least 80% is required.² To remark, producing syngas (mixture of CO and H_2) is not of interest due to its market price. Syngas price is roughly ten times lower than price of pure CO. Process producing syngas would be inherently unprofitable.³

Single-pass conversion

Single-pass conversion can be defined as ratio of the amount of product produced to the amount of CO_2 fed into the electrolyser. If a large fraction of CO_2 feed is converted, then the separation and recycling cost can be substantially decreased. Achieving high single-pass conversion of CO_2 is highly desired.⁴

Cell voltage

Cell voltage correlates to electricity consumption. To minimize the electricity consumption, the cell voltage should be minimized. A link between cell voltage and FE can also be made. Having voltage

efficiency defined as the ratio between applied cell voltage and thermodynamically determined voltage, then, energy efficiency is a product of FE and voltage efficiency. Energy efficiency directly reflects the amount of energy stored in the main product over the total energy input. Maximizing the energy efficiency means minimizing cell voltage and maximizing FE. As a result, for FE of 90%, cell voltage should not exceed 1.8 V.²

Thus finding appropriate operating conditions for the CO₂ electrolyser is crucial yet a complicated task. It is doubted how well catalyst performance, and material development as a whole, translate from low to higher, practically relevant current densities. And the complexity is further elevated by the reactions inside the electrolyser which strongly depend on the local environment.¹⁷

This makes scaling up this technology particularly challenging. Further, Jeanty *et al.*²¹ have shown that the performance of the electrolyser degrades when the electrolyser is scaled up. To illustrate, they achieved a stable FE of around 60% at 150 mA cm⁻² using an electrode area of 10 cm². However, when the area was scaled up by a factor of 10, the FE dropped to 50%. This shows that for a certain set of operating parameters, the performance does not translate well when scaling up. It is therefore crucial to understand how the electrolyser behaves under different currents and how exactly the operating parameters influence its performance. To address some of these issues, this project focuses on the modelling of the CO₂ electrolyser.

2.4. Description of the modelled electrolyser

A numerical model of the electrolyser is developed in accordance with the experimental lab-scale electrolyser. This experimental electrolyser was developed by Lorenz Baumgartner in our research group. The schematic of this electrolyser is presented in **Figure 2.3**. This electrolyser uses a GDE with two flowing electrolytes and it is thus equivalent to the second generation of electrolysers (**Figure 2.1b**).

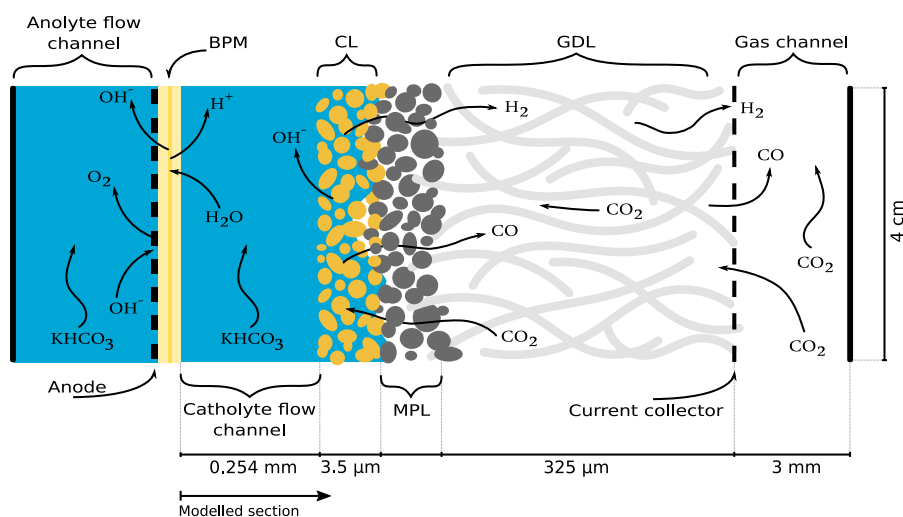


Figure 2.3: Schematic of the modelled laboratory CO₂ electrolyser. Arrows highlight its operating principle. Modelled section starts with BPM boundary. Out of plane dimension of the electrolyser is 4 mm, other length scales are included in the figure.

The anolyte is now placed at the outer side of the anode, unlike the general GDE based design. As anolyte, aqueous solution of 0.5 M KHCO₃ is used. Between the anolyte and ion-exchange membrane, titanium mesh coated with IrO₂ is placed and is serving as an anode. At the surface of the anode oxygen evolution reaction, OER, takes place, producing electrons which are then collected from the anode via current contacts. Adjacent to the anode is the ion-exchange membrane. In this case, bipolar membrane, BPM, is used. BPM is composed of anion and cation exchange membrane layer where the interface between these two types of membranes is referred to as interfacial layer. In the interfacial layer water dissociation takes place producing OH⁻ and H⁺ ions. OH⁻ ions are leaving the BPM through the anion exchange layer into the anolyte, while H⁺ ions are leaving the BPM through the cation exchange layer into the catholyte.²² Buffer solution of KHCO₃ saturated with 1 atm of CO₂ is used as catholyte. Catholyte flows in parallel to the anolyte in a laminar flow regime and is in direct contact with GDE which serves as cathode. Real structure of GDE is shown in **Figure 2.4**. Porous

CL provides a catalytically active surface for the electrochemical reactions. As CL, silver nanoparticles bound with Nafion ionomer are used. CO₂ is thus reduced to CO in what is known as CO evolution reaction, COER. Another profound electrochemical reaction occurring in the CL is H₂ evolution reaction, HER. Following the CL is the MPL, which is a porous medium doped with a hydrophobic polymer, and prevents the GDL from flooding. GDL is in contact with the gas channel. GDL distributes gas in its porous structure, provides mechanical stability, and electrical contact. In this work, Freudenberg GDL with MPL layer is used. In contact with GDL is meshed current collector which supplies electrons to the system. These electrons are by conduction through the solid porous phase of GDE delivered to the catalyst/electrolyte interface where are consumed in COER, or HER. Next to the current collector is a gas channel which feeds the GDE with CO₂.

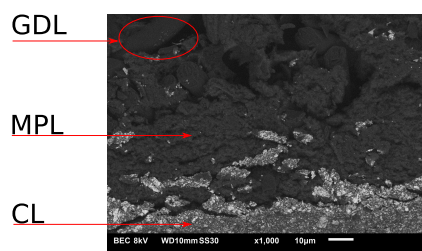


Figure 2.4: Part of GDE as viewed with scanning electron microscope when zoomed in on MPL.

2.5. Theoretical background of electrochemical CO₂ reduction

When applying a voltage across the cell, a reduction reaction is taking place at the cathode while an oxidation reaction occurs at the anode. To supply and extract charge from reduction and oxidation reactions, the charge is transported in the electrodes and in the outer circuit by electrons, and in the electrolyte phase by ions.²³

2.5.1. Cathodic half-cell

The electrolyte distribution inside the CL has a crucial impact on electrolyser performance and modelling results. Three cases of liquid distribution are distinguished in the modelling studies. Pores of the CL can be completely dry (gas+solid)⁸ or completely flooded (liquid+solid). CL can also be wetted by the electrolyte. This means that a film of electrolyte is covering the pores of the CL and the gas diffuses in between the liquid films. In terms of electrolyser performance, the latter is favoured because it minimizes the diffusional path of for a liquid CO₂ between the gaseous phase and catalyst surface.⁹ In certain modelling studies, CO₂ is assumed to react at the catalyst surface directly from the gaseous phase⁸ However, it is now commonly believed that for COER to occur a double phase interface (liquid/solid) is needed.^{17,24} **Figure 2.5** summarizes the species transport in the vicinity of CL.

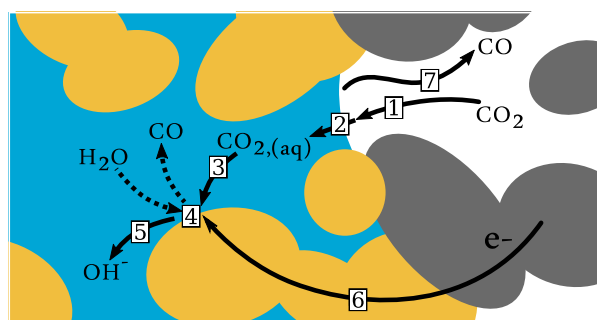
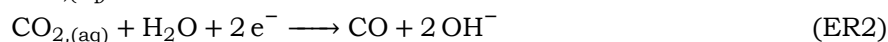
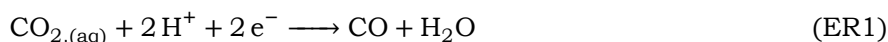


Figure 2.5: Zooming on the COER occurring in the vicinity of CL. (1) CO₂ is diffusing from the gas channel towards the CL layer, (2) transfer through the gas/liquid interface and dissolves in the electrolyte. (3) CO_{2,(aq)} diffuses towards the catalyst surface and (4) is reduced to CO at the catalyst surface. (5) produced OH⁻ ion diffuses out of the reaction zone. (6) electrons are supplied to the COER via conduction. (7) produced CO diffuses to the gas channel. Numbers also indicate the specific phenomena included in the developed model. Dashed lines represent phenomena that are neglected in the model (water required for COER is not considered in description of the COER rate, newly formed CO and H₂ are assumed to form directly on the gas/liquid interface). Figure was composed based on the work by Nesbitt *et al.*²⁴

COER

Depending on the local environment, COER can proceed via acidic pathway, ER1, or alkaline pathway, ER2.²⁵ Alkaline pathway prevails inside the CL as the pH rapidly increases during the electrolyser operation.⁶



$$E^0 = -0.11\text{ V vs. RHE} \quad T=298.15\text{ K, (aq)}^{13}$$

Above, the equilibrium potential for the two reactions should differ. However, in the CO₂ electrolysis literature, often the indicated value is used for both reactions.²⁵ It is briefly elaborated on in subsection 3.2.5.

HER

Parasitic reaction occurring inside the CL is the H₂ evolution reaction, HER. HER proceeds via both acidic and alkaline pathways, ER3 and ER4, respectively.^{10,13} In CO₂ electrolysers, alkaline environment establishes around the cathode leading to HER to proceed via alkaline pathway.^{6,7}



$$E^0 = 0.00\text{ V vs. RHE} \quad T=298.15\text{ K, (aq)}^{23}$$



$$E^0 = -0.83\text{ V vs. RHE} \quad T=298.15\text{ K, (aq)}^{23}$$

2.5.2. Anodic-half cell

The anodic side was an objective of this work, therefore, less attention is paid to this part of electrolyser.

OER

The OER can proceed via acidic or alkaline pathway, ER5 or ER6, respectively.²⁶ However, the reactant for the alkaline pathway gets quickly depleted in the considered electrolyser. This is because the feed electrolyte is around neutral pH and does not supply enough OH⁻ ions in comparison to the reactant of the acidic pathway. This means that the acidic pathway will prevail and locally acidic region will form around the anode. To support this claim, El-Shafie *et al.*¹² and Kotb *et al.*¹¹ model CO₂ electrolyser and consider only the acidic pathway as well.

Another source of OH⁻ for the alkaline pathway could originate from the OH⁻ ions produced at the cathode. However, as we later see in the results, OH⁻ ions do not diffuse close enough to the anode to contribute to the alkaline OER.



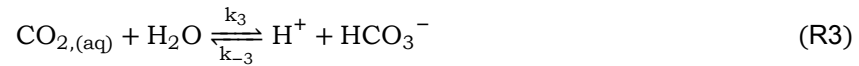
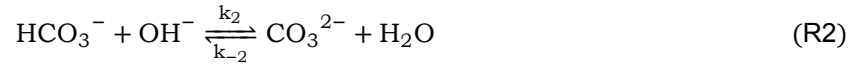
$$E^0 = 1.23\text{ V vs. RHE} \quad T=298.15\text{ K, (aq)}^{23}$$



$$E^0 = 0.40\text{ V vs. RHE} \quad T=298.15\text{ K, (aq)}^{23}$$

2.5.3. Homogeneous reactions in the liquid phase

Electrolyte has a crucial effect on the electrochemical reactions inside the CL. Four homogeneous reactions involving carbon species, R1 to R4 shown below, and water self-ionization, R_w, can occur in the liquid phase. R1 and R2 prevail in the alkaline environments, while R3 and R4 prevail in acidic. Each reaction rate can be described by a forward and a backward rate constant, e.g. k_1 and k_{-1} , respectively. **Table 2.2** gives an overview of these reaction rate constants.



The R1 stoichiometry shows that this reaction will be responsible for the unwanted consumption of CO_{2,(aq)}. This reduces the amount of available reactant for COER. Rate of this reaction will increase with increasing pH. As the pH inside the CL rises (follows from the alkaline COER and HER stoichiometry), the R2 reaction will reduce the rate at which this pH increases (buffering effect). The OH⁻ ions will be predominantly consumed in R2 and only in the second place in R1. This follows from reaction rate constants which show that in comparison to R1, R2 is a substantially faster reaction (**Table 2.2**).^{6,13,27} When adding H⁺ ions into the KHCO₃ solution. The R3 backward reaction will prevail as the amount of available HCO₃⁻ is the highest. The concentration of CO₃²⁻ will be minimal.

Table 2.2: List of the reaction rate constants.²⁸

Reaction	Forward rate constant	Unit	Backward rate constant	Unit
R1	2.23	m ³ mol ⁻¹ s ⁻¹	5.23 · 10 ⁻⁵	s ⁻¹
R2	6 · 10 ⁶	m ³ mol ⁻¹ s ⁻¹	1.25 · 10 ⁶	s ⁻¹
R3	3.71 · 10 ⁻²	s ⁻¹	8.7 · 10 ¹	m ³ mol ⁻¹ s ⁻¹
R4	5.94 · 10 ¹	s ⁻¹	1.24 · 10 ⁹	m ³ mol ⁻¹ s ⁻¹
Rw	1	mol m ⁻³ s ⁻¹	1 · 10 ⁸	m ³ mol ⁻¹ s ⁻¹

The above stoichiometry reveals why KHCO₃ is chosen as electrolyte. First, KHCO₃ provides the buffering effect and reduces the amount of CO_{2,(aq)} consumed in the reaction with OH⁻ ions. Second, according to alkaline HER pathway, its rate can be mitigated in neutral or alkaline environments. This favours the choice of KHCO₃ which equilibrium pH is 7.55 (500 mM KHCO₃ saturated with 1 atm of gaseous CO₂). Finally, when saturating the electrolyte with gaseous CO₂, the HCO₃⁻ and CO₃²⁻ species inherently occur.

2.6. Recent development in the CO₂ electrolyser modelling

The objective of this section is to gather, assess and utilize published methods and findings from papers describing different CO₂ electrolyser models. This section helps to define a research question and tries to point out the way how to newly and relevantly contribute to this field of research. **Table 2.3** provides an overview of the considered modelling studies with their general description. Discussion is primarily focused on GDE based electrolyzers and gathers most of the modelling studies published in the literature. All considered models are assuming a steady state and were developed using commercial COMSOL software.

Table 2.3: Overview of the discussed research papers focusing on the modelling of CO₂ electrolyzers

Research group	Electrolyzer type	Main product	Electrolyte	Max. current [mA cm ⁻²]	Dimensions
Wu <i>et al.</i> 2014 ⁸	Microfluidic cell	CO	KCl	80	2D
Kotb <i>et al.</i> 2017 ¹¹	H-cell	CH ₃ OH	KHCO ₃	20	2D
Hashiba <i>et al.</i> 2018 ²⁹	H-cell	CH ₄	KCl, KHCO ₃ , KH ₂ PO ₄ +K ₂ HPO ₄	90	1D
Weng <i>et al.</i> 2018 ⁹	GDE based	CO	KHCO ₃	1000	1D
Weng <i>et al.</i> 2019 ¹⁰	MEA	CO	KHCO ₃	1000	1D
El-Shafie <i>et al.</i> 2020 ¹²	GDE based	CH ₃ OH	KHCO ₃	10	2D
Yang <i>et al.</i> 2020 ⁷	GDE based	HCOO ⁻	KOH	200	2D
Kas <i>et al.</i> 2021 ⁶	GDE based	CO	KHCO ₃	1000	2D

Wu *et al.* 2014⁸

Group around Wu *et al.*⁸ developed one of the first numerical models of the GDE in COMSOL and their model can be used as a good basis for the description of the gas related phenomena. Regarding the aspects of their model, the authors did not include liquid phase and assume COER reaction to proceed at the gas/solid interface rather than at the liquid/solid interface. The study investigates effects of feed CO₂ concentration, feed flow rate, channel length and GDE porosity. Increasing electrode length is shown to have detrimental effect on both FE and current density towards COER. They explain this by increasing dilution of the reactant. CO₂ conversion on the contrary increases as a result of more active sites. GDL porosity is shown to have minimal effect on the electrolyser performance.

The major shortcomings of their model lie in omitting the liquid phase and the assumption of the COER kinetics. In the work published by Nesbitt *et al.* 2020,²⁴ double-phase interface, i.e. liquid/solid, and triple-phase boundary, i.e. gas/liquid/solid, is compared as to determine which interface is responsible for the COER. They conclude with liquid/solid interface to be primary reaction pathway for COER.

Kotb *et al.* 2017¹¹

Another numerical model, now describing only the liquid phase, was developed by Kotb *et al.*¹¹ They model H-cell configuration (**Figure 2.1a**) with KHCO₃ as electrolyte, but omit the homogeneous reactions. They find current distribution along the cathode surface and in the electrolyte flow direction reaching maximum just at the inlet. Then, with increasing distance, HER starts to dominate, and finally, current stabilizes just before the outlet. The authors explain this solely by a fast reactant depletion.

Hashiba *et al.* 2018²⁹

The work published by these authors investigates effect of different electrolytes. For this end, Hashiba *et al.*²⁹ focused on modelling of the liquid boundary layer adjacent to the CL. They find KHCO₃ supporting higher currents than the KCl electrolyte. They explain this by KHCO₃ being able to buffer increasing local pH and thus limit the consumption of CO₂ via R1. Further, they explain the effect of phosphate buffer and influence of pKa on the pH profile.

Weng *et al.* 2018⁹ & 2019¹⁰

The first model developed in 2018 considers only CL and GDL in 1D. The concept of CL saturation is introduced into the governing equations representing the partially flooded CL. The authors, nevertheless, also consider fully flooded CL. They find pH strongly increasing in the CL and at high currents the local current distribution inside the CL shifts from being evenly distributed throughout the whole domain to only the edges of the CL. Next, Weng *et al.*⁹ report that change in catalyst loading, i.e. width of CL, negatively influences current density in the kinetically controlled regime, that is at low overpotentials. However, in mass-transfer limited regime, that is at higher overpotentials, lower CL width results in an increase of current. This effect is displayed in **Figure 2.6**. Finally, an increase in current density is reported for increasing CL porosity and electrolyte flow rate. Limitation of this model originates from its 1D nature which precludes itself from capturing the effects arising along the electrolyte flow direction.

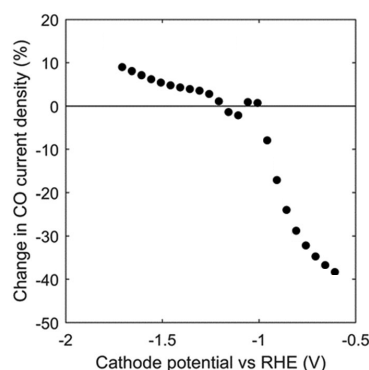


Figure 2.6: Effect of decreased catalyst loading (simulated by manipulating the width of CL) on COER current density as a function of cathode potential. The negative change in current density occurs in the kinetically controlled regime, while, the increase in current density occurs in the mass transfer limited regime. In the latter regime, the thinner CL is responsible for a lower mass-transfer resistance. Figure adopted from:⁹

The model developed in 2019 focuses on MEA, but still considers Ag catalyst and KHCO₃ electrolyte. This study can be used to, for example, reuse the electrochemical kinetic parameters. Contrary to previous studies, in this model authors assume COER current density to be proportional to the concentration of CO₂ in the liquid phase to the power of 1.5.

El-Shafie *et al.* 2020¹²

Model developed by these authors is one of the first 2D models including both liquid and gaseous phases. To match the experimental data, the authors couple number of fitting parameters with exchange current density and CO₂ flux through the gas/liquid interface. The authors investigate the effect of gas and electrolyte flow rate, and feed CO₂ concentration. Most notably, generation of a main product, in this case CH₃OH, is found to decrease with increasing electrolyte flow rate and then rapidly increase at very high flow rates. This variation in product generation is explained by electrolyte flow rate effecting the capillary forces in the CL. However, in the model, variable product generation is captured by fitting parameters which correlate exchange current density and electrolyte flow rate. Main limitation of this model is the maximum current density which is around 10 mA cm⁻².

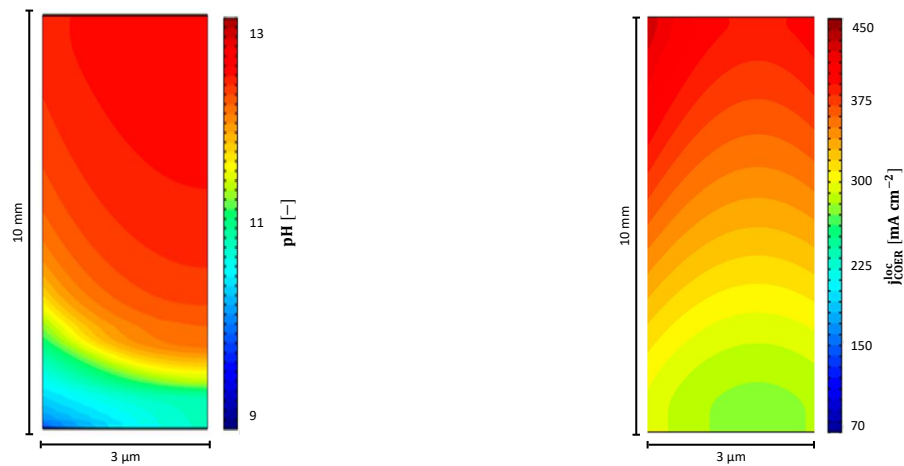
Yang *et al.* 2020⁷

Another 2D model of the GDE based electrolyser was developed by Yang *et al.*⁷ They consider only the cathodic half-cell and focus on HCOO⁻ as the main product while using KOH as electrolyte. CL is assumed to be partially flooded. Their investigations covers gas flow rate, feed CO₂ concentration, and catalyst loading and porosity. As the authors couple CL porosity with catalyst loading, it is firstly found that higher CL porosity has a rather positive impact on the current density towards the main product. This is explained as a result of interplay of different parameters such as specific surface area, conductivity or effective diffusion coefficients. However, when a higher catalyst loading is used, the ideal CL porosity shifts from around 80% % to 50%. They explain this shift by increase in CL width which follows from a higher catalyst loading at constant porosity. This then negatively influence CO₂ partial pressure and finally product generation.

Kas *et al.* 2021⁶

Finally, the most recently published 2D model focuses on phenomena in the local environment of the CL. CL is assumed partially flooded (gas+liquid+solid). First, authors show the depletion of HCO₃⁻ and how this depleted boundary layer increases from the inlet to the outlet. As a result of HCO₃⁻ depletion and COER, the authors visualize a distinct pH distribution inside the CL. They relate that to the COER current distribution. Both are presented in **Figure 2.7**. Further, the authors point out how depletion of gaseous CO₂ along the gas channel increases the relative formation of HER, i.e. decreases the FE. It is then shown that this decrease in FE can be compensated by a higher gas flow rate which, however, substantially lowers the CO₂ conversion. One of the main limitations of this model is the neglected migration of the charged species and possible the water self-ionization reaction. Further drawback is the modelled electrolyser length which is restricted to 14 mm. However, these authors show how the

variations along the flow direction have a great impact and the electrolyser performance. It should be assessed on more industrially relevant scales too.



(a) pH distribution inside the CL at -1.3 V vs. RHE

(b) COER current density distribution inside the CL at -1.3 V vs. RHE

Figure 2.7: Distribution of (a) pH and (b) COER current density inside the CL. In both cases electrolyte flow on the left from the bottom to the top. GDL is on the right. According to Kas *et al.*,⁶ diagonally increasing pH distribution is a result of depletion of buffer capacity. The top left and bottom right corners of the CL have the highest and the lowest diffusion layer thickness for the HCO_3^- ions. Regarding COER current distribution, the authors claim it to be governed by the local concentration of CO_2 . It decreases in the direction of the flow due to electrochemical reaction and also decreases in the regions of high pH as a consequence of enhance rate of R1. Figure adopted from:⁶

2.7. Research question

The two important metrics characterizing performance of a CO₂ electrolyser are total current density and faradaic efficiency. Understanding how these metrics evolve while applying a voltage across the cell, and understanding how these metrics are distributed inside the CL is a crucial step in successfully developing this technology. Thus the primary goal of this thesis project is to bring more understanding into the operation of a CO₂ electrolyser. Specifically, we aim to link the electrolyser performance to the phenomena occurring in the background and answer the following.

- When do disturbances in the cathode local environment start to influence the electrolyser performance?
- What is the pH distribution inside the CL and what is its cause?
- How is the current and FE distributed inside the CL and what is its cause?
- How is the CO₂ solubility affected and can it influence the electrolyser performance?

We try to answer the above set of questions for a chosen set of parameters. However, the electrolyser performance can be significantly influenced by various parameters. We thus conduct a parametric study where we try to answer how exactly the electrolyser performance changes and we try to explain what is the reason behind these changes. We focus on the following parameters.

- Liquid flow rate
- Electrolyser length
- Operating pressure

If a CO₂ electrolyser should successfully contribute to the mitigation of climate change, it needs to be scaled up. However, scaling up this technology has not been investigated yet. We thus try to answer the following questions.

- What is the difference in FE, current density and CO₂ conversion, when a laboratory electrolyser is scaled up to the industrially sized one?
- What limitations arise at the industrial scale?
- What causes these limitations?

Electrolyser performance is not only given by the catalyst activity but it also depends on the local cathodic environment. In the last section, we consider two variations in the electrolyser configuration, specifically, the following.

- What effect does a fluid flow configuration have on the electrolyser performance?
- What effect does a varying catalyst loading have on the electrolyser performance?

To find the answers to these questions, we aim to develop a numerical 2D model. Such model should include all the relevant phenomena. It should be robust and converge also at high current densities. It should primarily focus on the description of the cathode, but should also include the influence arising from the anodic compartment. The model will be developed in COMSOL.





3

Methodology

3.1. Fundamental considerations

The model development starts by defining its scope. The primary goal of this study is to investigate electrolyser performance as determined by the cathode. Under this consideration, anodic half-cell compartment is neglected. Effect of the anode, or the BPM, will be accounted for only via a boundary condition. The primary focus is set on the cathodic half-cell and the electrolyte channel. The model is developed in 2D so to capture spatial variations along the fluid flow direction. **Table 3.1** visualizes these modelled domains, modelled phenomena, and the variables that are solved for. These variables are c_i , concentration of chemical species i , ϕ_s and ϕ_l , electric (solid) and electrolyte (liquid) potential, respectively, ω_i , mass fraction of chemical species i , and p relative pressure.

Table 3.1: Modelled physical phenomena with their dependent variables and considered parameters.

Domain	Catholyte	CL	GDL	Gas channel
Illustration				
Phase	(l)	(s)+(l)	(s)+(g)	(g)
Considered phenomena	Convection Diffusion Migration Homogeneous reactions Charge-transfer	Diffusion Migration Electrochemical reactions Homogeneous reactions Charge-transfer Phase transfer	Diffusion Convection Charge-transfer	Convection Diffusion
Dependent variables	$c_{\text{CO}_2(\text{aq})}$, c_{H^+} , c_{OH^-} , $c_{\text{HCO}_3^-}$, $c_{\text{CO}_3^{2-}}$, ϕ_l	$c_{\text{CO}_2(\text{aq})}$, c_{H^+} , c_{OH^-} , $c_{\text{HCO}_3^-}$, $c_{\text{CO}_3^{2-}}$, ϕ_s , ϕ_l	ω_{CO_2} , ω_{CO} , ω_{H_2} , ω_{N_2} , ϕ_s , p	ω_{CO_2} , ω_{CO} , ω_{H_2} , ω_{N_2}
Parameters	D_i , k , ρ_l , μ_l , u_y	D_i , k , $\epsilon_{s,\text{CL}}$, $\sigma_{s,\text{CL}}$, E^0 , j_0 , α , a_s , r_{np} , H_{CO_2} , $\Delta_{\text{sol}}H_{\text{CO}_2}$, K_s , k_{CO_2}	$D_{i,j}$, $\sigma_{s,\text{GDL}}$, ϵ_{GDL} , μ_g , λ , κ^0 , p_{abs}	$D_{i,j}$, p_{abs} , $u_{y,g}$

The next step is to determine the model assumptions. The model assumes steady state and isothermal conditions. The MPL is omitted. Electrolyte flow is single-phase and laminar. Transport of aqueous species is based on the dilute theory. Material properties are assumed isotropic. GDL is assumed to be

free of liquid at all times. If more detailed assumptions are needed, they are provided in their applicable sections below.

Special considerations have to be made in respect to CL. The CL is assumed to be fully flooded with the liquid. Convection is assumed not to apply. COER happens on the liquid/solid interface. The active area is equal to the specific surface area. The generated gaseous products, CO and H₂, are assumed to appear directly at the gas/liquid interface.

3.2. Governing equations

To successfully predict the real functionality of the CO₂ electrolyser, relevant governing equations have to be identified and successfully set up in the simulation software. Often, the choice of governing equations offers limited flexibility and can be directly taken from the previous modelling studies. Open to the discussion are, for example, relevant kinetic equations describing electrochemical reactions. For clarity, we provide all the governing equations and relations in one section.

3.2.1. Species transport in the gaseous phase

Governing equations in the gaseous phase often work on a mass basis while the description of liquid phase often works on a molar bases. Here, we provide the definitions for both directly. Equation 3.1 defines molar and mass fraction, x_i and ω_i , respectively. c stands for total molar concentration of all species in a considered domain, and ρ stands for total mass concentration of all species in a considered domain. Equation 3.2 defines a relation between total and species concentrations, where n stands for the total number of species present in a considered domain.

$$x_i = \frac{c_i}{c}, \quad \omega_i = \frac{\rho_i}{\rho} \quad (3.1)$$

$$c = \sum_{i=1}^n c_i, \quad \rho = \sum_{i=1}^n \rho_i \quad (3.2)$$

Equation 3.3 defines molar and mass flux of species i , \mathbf{N}_i and \mathbf{N}_i^m , respectively. Vectors are in this work denoted in bold. Mass based terms will be for clarity denoted with superscript m. \mathbf{u}_i represents velocity of species i .

$$\mathbf{N}_i = c_i \mathbf{u}_i, \quad \mathbf{N}_i^m = \rho_i \mathbf{u}_i \quad (3.3)$$

Equation 3.4 defines average velocity in the mixture, where \mathbf{u} stands for molar average velocity and \mathbf{v} refers to mass average velocity.³⁰

$$\mathbf{u} = \sum_{i=1}^n x_i \mathbf{u}_i, \quad \mathbf{v} = \sum_{i=1}^n \omega_i \mathbf{u}_i \quad (3.4)$$

Diffusion flux of species i is defined relative to the flux of the mixture as whole. Thus, Equation 3.5 defines molar and mass diffusion flux, \mathbf{J}_i and \mathbf{J}_i^m , respectively.³¹

$$\mathbf{J}_i = c_i(\mathbf{u}_i - \mathbf{u}), \quad \mathbf{J}_i^m = \rho_i(\mathbf{u}_i - \mathbf{v}) \quad (3.5)$$

Rearranging and substituting for the terms above, yields Equation 3.6.³⁰

$$\mathbf{J}_i = \mathbf{N}_i - c_i \mathbf{u}, \quad \mathbf{J}_i^m = \mathbf{N}_i^m - \rho_i \mathbf{v} \quad (3.6)$$

Finally, Equation 3.7 presents the conservation of chemical species in the per mass basis form.

$$\rho \frac{\partial \omega_i}{\partial t} = -\nabla \cdot \mathbf{N}_i^m + R_i^m \quad (3.7)$$

The law sets accumulation of species per unit volume, $\frac{\partial \omega_i}{\partial t}$, equal to the rate at which species enter or leave the unit volume, and are created or consumed in the unit volume, R_i^m .³¹ Assuming steady-state, the term representing the accumulation of species i becomes zero. It is assumed that no reactions occur in the gaseous phase, thus the R_i^m reduces to zero and the conservation law reduces to Equation 3.8.

$$\nabla \cdot \mathbf{N}_i^m = 0 \quad (3.8)$$

From Equation 3.8, it follows to describe the diffusion flux. Diffusion can be modelled using Fick's law, mixture-average model, or using general Maxwell-Stefan equations. The mixture-averaged model is often the choice in the description of the GDE. This model, assumes diffusion flux to be proportional only to the molar fraction gradient. However, mixture-averaged diffusion coefficients provide a better description than simple diffusion coefficients used in Fick's law. Diffusion coefficients appearing in Fick's law are constant and applicable to only binary diffusion or very dilute solutions. Compared to the Maxwell-Stefan description, the mixture-averaged model is less rigorous but also less computationally expensive. Equation 3.9 introduces mass diffusion flux as used in the mixture-averaged model.³²

$$\mathbf{J}_i^m = -\rho_i \mathcal{D}_i^m \frac{\nabla x_i}{x_i} \quad (3.9)$$

Above, \mathcal{D}_i^m stands for the mixture-averaged diffusion coefficient. To substitute for the molar gradient, Equation 3.10 defines mass-averaged molar mass, M_n . Equation 3.11 gives the relation between x_i and ω_i , where M_i is the molar mass of species i . When both are combined with Equation 3.9, Equation 3.12 is obtained which describes \mathbf{J}_i^m .

$$M_n = \left(\sum_i^n \frac{\omega_i}{M_i} \right)^{-1} \quad (3.10)$$

$$x_i = \frac{\omega_i M_n}{M_i} \quad (3.11)$$

$$\mathbf{J}_i^m = -\rho \mathcal{D}_i^m \nabla \omega_i - \omega_i \rho \mathcal{D}_i^m \frac{\nabla M_n}{M_n} \quad (3.12)$$

If the diffusion occurs in porous media, then, effective diffusion coefficient, $\mathcal{D}_{i,j}^{\text{eff}}$, is defined to account for porosity. The effective diffusion coefficient is a result of a product of Maxwell-Stefan diffusivity, $\mathcal{D}_{i,j}$ and a function $f(\epsilon, \tau)$. $\mathcal{D}_{i,j}$ characterizes diffusivity between species i and j . It is a tabulated value. $f(\epsilon, \tau)$ characterizes a porous medium with porosity ϵ and tortuosity τ . It can be evaluated from a Bruggeman model which is presented in Equation 3.14.³³ The Bruggeman relation is widely used but its validity for porous electrodes has been questioned recently.³⁴

$$\mathcal{D}_{i,j}^{\text{eff}} = f(\epsilon, \tau) \mathcal{D}_{i,j} \quad (3.13)$$

$$f(\epsilon, \tau) = \epsilon^{\frac{3}{2}} \quad (3.14)$$

$$(3.15)$$

However, \mathcal{D}_i^m is used in the \mathbf{J}_i^m above. \mathcal{D}_i^m can be derived when combining Maxwell-Stefan equations, Equation 3.16, where ideal gas, isobaric, and isothermal conditions are assumed, with Equation 3.9, which was converted to molar basis. In this derivation, a limiting case is assumed which states that the species i is diffusing through $n - 1$ stagnant gases ($\mathbf{N}_j = 0, j \neq i$). When all combined, Equation 3.17 describing mixture-averaged diffusion coefficient is obtained³⁰

$$\nabla x_i = \sum_{\substack{j=1, \\ j \neq i}}^n \frac{x_i \mathbf{N}_j - x_j \mathbf{N}_i}{c \mathcal{D}_{i,j}^{\text{eff}}} \quad (3.16)$$

$$\mathcal{D}_i^m = \frac{1 - x_i}{\sum_{\substack{j=1, \\ j \neq i}}^n \frac{x_j}{\mathcal{D}_{i,j}^{\text{eff}}}} \quad (3.17)$$

When the mean free path, λ , of a molecule is comparable to a characteristic length of the system, in this case the average pore diameter, Knudsen diffusion can occur. This type of diffusion thus describes a transport, where individual molecules are more likely to move by collisions with pore walls rather than by interaction with other molecules. To account for this type of transport Knudsen diffusion coefficient, D_i^k , is introduced. D_i^k can be computed from Equation 3.18, where T is the temperature in K and R is the universal gas constant. λ is assumed to be equal to the pore diameter of GDL.

$$D_i^k = \frac{\lambda}{3} \sqrt{\frac{8RT}{\pi M_i}} \quad (3.18)$$

Gaseous species transport inside GDE can thus be described with two diffusion coefficients. Mixture-averaged diffusion coefficient, \mathcal{D}_i^m , and Knudsen diffusion coefficient, D_i^k . These are combined in one such that species conservation law can be used. Therefore, the two diffusion mechanisms are assumed to occur in series which gives D_i as shown in Equation 3.19.

$$D_i = \left(\frac{1}{\mathcal{D}_i^m} + \frac{1}{D_i^k} \right)^{-1} \quad (3.19)$$

Additionally, it should be elaborated on the mass diffusion flux. Starting from the definition of diffusion flux, then summing up the diffusion flux over all the species and further using the definition of mixture averaged velocity results in Equation 3.20. It is found that sum of diffusion fluxes over all species in a fluid mixture will always be zero.³¹

$$\sum_{i=1}^n \mathbf{J}_i^m = 0 \quad (3.20)$$

The same, however, does not hold for mass diffusion flux which is described in Equation 3.12. For that reason, correction velocity, \mathbf{v}_c , is introduced. It is if found from the condition above. \mathbf{v}_c is thus defined by Equation 3.21.³²

$$\mathbf{v}_c = \sum_{i=1}^n \omega_i \mathcal{D}_i^m \frac{\nabla x_i}{x_i} \quad (3.21)$$

\mathbf{v}_c then creates an additional component of the diffusion flux of species i . It is simply added to the Equation 3.12. Finally, to account for both types of diffusion, diffusion coefficient \mathcal{D}_i^m in Equation 3.12 and Equation 3.21 is simply substituted by the combined diffusion coefficient D_i leading to the final expression for the diffusion flux expressed in Equation 3.22.³²

$$\mathbf{J}_i^m = -\rho D_i \nabla \omega_i - \omega_i \rho D_i \frac{\nabla M_n}{M_n} + \rho \omega_i \sum_{i=1}^n \frac{M_i}{M_n} D_i \nabla x_i \quad (3.22)$$

Recalling the Equation 3.6, so described mass diffusion flux is then substituted into \mathbf{N}_i^m and \mathbf{N}_i^m into the species conservation law giving the final equation describing transport of gaseous species inside GDL.³¹ \mathbf{v} appearing in the \mathbf{N}_i^m can be obtained from Darcy's law as described in subsection 3.2.7.

The chemical species conservation law above can be constructed for each species providing thus n equations. However, only $n-1$ equations are independent. Consequently, the last species is calculated from Equation 3.23 which stands for mass constraint.³⁰

$$\sum_{i=1}^n \omega_i = 1 \quad (3.23)$$

3.2.2. Species transfer through the gas/liquid interface

In this model, we assume that CO_2 is the only gaseous species that dissolves in the liquid phase. This is supported by first, the solubility of CO and H_2 , which is substantially lower than the solubility of CO_2 . Specifically, Henry's constant for H_2 and CO is in comparison to Henry's constant for CO_2 lower by over a factor of 400 and 30, respectively.³⁵ Second, the partial pressure of H_2 and CO in GDE can be expected to be substantially lower than the CO_2 partial pressure. This means that even if the Henry's constants were same, a lower amount of H_2 and CO would be dissolved. Therefore, we will consider CO_2 as only species to transfer via the gas/liquid interface. If the CO_2 is dissolved in the liquid, it will be further always denoted as $\text{CO}_{2,(aq)}$. Newly formed H_2 and CO will be assumed to directly appear at the gas/liquid interface already in the gaseous form.

The transport of species through an interface can be determined as product of a certain driving force and a proportionality constant. In this case, the driving force is a difference in concentration. We start by assuming that very close to the gas/liquid interface, the CO_2 concentration in the liquid will approach an equilibrium value, $c_{\text{CO}_{2,(aq)}|_{\text{eqlb}}}$. The $c_{\text{CO}_{2,(aq)}|_{\text{eqlb}}}$ can be calculated from Henry's constant, H_{CO_2} , and CO_2 partial pressure, p_{CO_2} as in the Equation 3.24.

$$c_{\text{CO}_{2,(aq)}|_{\text{eqlb}}} = H_{\text{CO}_2} p_{\text{CO}_2} \quad (3.24)$$

The next concentration should correspond to the CO_2 concentration in the bulk of the liquid. However, we can expect CO_2 concentration to vary significantly in both x and y direction over the whole porous structure of the CL. Thus, the question is what we define as bulk when it comes to the CL. Here, we use the concentration of the dissolved CO_2 at the gas/liquid surface, $c_{\text{CO}_{2,(aq)}|_{g/l}}$ as a bulk concentration. This is one of the assumptions that could be better addressed in a future study. We remark that this will not lead to the interface attaining a constant equilibrium concentration, because the CO_2 still enters the liquid phase with a certain rate.

To determine the rate at which the gaseous CO_2 enters the liquid phase, Equation 3.25 defines CO_2 mass transfer coefficient, k_{CO_2} . The characteristic diffusion length is in this case represented by a d_p which stands for a CL pore diameter. In this study, k_{CO_2} is taken from the study by Kas *et al.*⁶

$$k_{\text{CO}_2} = \frac{D_{\text{CO}_{2,(aq)}}}{d_p} \quad (3.25)$$

Combining all together, Equation 3.26 gives the equation describing the rate at which CO_2 transfer via the gas/liquid interface, where $J_{\text{CO}_2|g/l}$ represents a molar flux in $\text{mol m}^{-2} \text{s}^{-1}$. Positive value of $J_{\text{CO}_2|g/l}$ refers to the CO_2 entering the CL.

$$J_{\text{CO}_2|g/l} = k_{\text{CO}_2} (c_{\text{CO}_{2,(aq)}|_{\text{eqlb}}} - c_{\text{CO}_{2,(aq)}|_{g/l}}) = k_{\text{CO}_2} (H_{\text{CO}_2} p_{\text{CO}_2} - c_{\text{CO}_{2,(aq)}|_{g/l}}) \quad (3.26)$$

Now it remains to determine the value of H_{CO_2} . Values of Henry's constants can be found in literature.³⁵ However, equilibrium constants generally vary with temperature.³⁶ To correct for the operating temperature, a general form of Van 't Hoff equation, Equation 3.27, is be used. Adjusting the equation to this case gives the Equation 3.28.

$$\frac{d \ln H_{i,vH}}{dT} = \frac{\Delta_{\text{sol}} H_i}{RT^2} \quad (3.27)$$

$$H_{\text{CO}_2,vH} = H_{\text{CO}_2,\text{ref}} \exp\left(-\frac{\Delta_{\text{sol}} H_{\text{CO}_2}}{R} \left(\frac{1}{T} - \frac{1}{T_{\text{ref}}}\right)\right) \quad (3.28)$$

Above, subscript vH denotes the Henry's constant which is corrected with Van 't Hoff relation. $\Delta_{\text{sol}} H_{\text{CO}_2}$ expresses the enthalpy of CO_2 dissolution, and T_{ref} is the temperature at which the literature value of Henry's constant, $H_{\text{CO}_2,\text{ref}}$ is provided.³⁵ In this study, we use 293.15 K as the operating temperature, T .

Salting-out effect

The concentration of ions inside the CL can substantially increase during the electrolyser operation.^{6,9} It is also known that the gas solubility generally decreases with increasing salt concentration. This phenomenon is known as the salting-out effect and can be estimated using the Sechenov relation presented in Equation 3.29.

$$\log \frac{c_{g,0}}{c_g} = K c_s \quad (3.29)$$

In the Equation 3.29, $c_{g,0}$ and c_g represents gas solubility in pure water and salt solution, respectively. c_s denotes salt concentration and K is the Sechenov constant.³⁷ The Sechenov equation however holds for a single salt only. Later, Schumpe extended this model to mixed salt solution and published the Equation 3.30.

$$\log \frac{c_{g,0}}{c_g} = \sum (h_i + h_G) c_i \quad (3.30)$$

In the Schumpe equation (Equation 3.30), the gas solubility in salt solution is calculated based on ion specific constants: h_i and h_G . h_i is a tabulated value and can be found in literature.³⁸ h_G is also a tabulate value, but it can be further corrected for a specific temperature by Equation 3.31. $h_{G,0}$ and h_T are tabulated values which can be taken from a paper by Weisenberger and Schumpe.³⁹

$$h_G = h_{G,0} + h_T (T - 298.15) \quad (3.31)$$

Next, Equation 3.32 links the K for a single salt to the ionic constants. In Equation 3.32, n_i stands for index of ion i in the salt formula.³⁹

$$K = \sum (h_i + h_G) n_i \quad (3.32)$$

The equation above allows us to calculate K for each salt separately. Each salt will thus have its own Sechenov constant which we denote as K_s . The reduced gas solubility can then be calculated from the Equation 3.33, where effect of each ion is considered, and the Equation 3.34, where effect of each salt is considered. Salt concentration is represented by c_s .

$$K_s = \sum_i (h_i + h_G) n_i \quad (3.33)$$

$$\log \frac{c_{g,0}}{c_g} = \sum_s K_s c_s \quad (3.34)$$

To clarify, the c_i is recovered as a product of c_s and n_i . Thus, for the Equation 3.34 to correlate with the Schumpe equation (Equation 3.30), we need to carefully choose the c_s . This means that c_s must be equal to the c_i which has the the lowest value of n_i and further the c_s must be divided by this n_i .

Now returning to the modelled CO₂ electrolyser. During the electrolyser operation, concentration of HCO₃⁻, CO₃²⁻, and OH⁻ will change dramatically. However, since electroneutrality is assumed, each anion is compensated by K⁺ cation. This means that in each instant we find three different salts in the electrolyte. These are KHCO₃, K₂CO₃, and KOH. Using the above equations, we can calculate K_s for each one of these salts. The c_s of each salt is in this case directly equal to the anion concentration in the considered salt. **Table 3.2** gives the ionic constants used to calculate the K_s . **Table 3.3** gives the calculated K_s for each salt found in the electrolyser.

Table 3.2: Model parameters used to estimate the K_s ³⁹

Model parameters	Unit	Species	Value
		H ⁺	0
		K ⁺	0.0922
h_i	m ³ kmol ⁻¹	HCO ₃ ⁻	0.0967
		CO ₃ ²⁻	0.1423
		OH ⁻	0.0839
$h_{G,0}$	m ³ kmol ⁻¹	CO ₂	-0.0172
$h_T \times 10^3$	m ³ K ⁻¹ kmol ⁻¹	CO ₂	-0.338

Table 3.3: K_s calculated for the 3 different salts found in the electrolyte

Salt	K_s [m ³ kmol ⁻¹]
KHCO ₃	0.1579
K ₂ CO ₃	0.2802
KOH	0.1451

Finally, it remains to find an expression for the new Henry's constant which considers the salting-out effect. First, the $c_{g,0}$ and c_g in Equation 3.34 are substituted with Henry's law leading to Equation 3.35. Second, rearranging and evaluating the sum then gives Equation 3.36. H_{CO_2} appearing in Equation 3.36 is the final equation for Henry's constant used in the model.

$$\log\left(\frac{H_{CO_2,vH} p_{CO_2}}{H_{CO_2} p_{CO_2}}\right) = \sum K_s c_s \quad (3.35)$$

$$H_{CO_2} = H_{CO_2,vH} 10^{-\left(K_{KHCO_3} c_{HCO_3^-}|_{g/l} + K_{K_2CO_3} c_{CO_3^{2-}}|_{g/l} + K_{KOH} c_{OH^-}|_{g/l}\right)} \quad (3.36)$$

Without having to explicitly consider the K⁺ ions, the Equation 3.36 thus allows us to determine the effect each salt has on the reduction of H_{CO_2} . When solving the model, Equation 3.36 uses the concentration of anions directly from the gas/liquid interface similarly to the $c_{CO_2,(aq)}|_{g/l}$.

3.2.3. Species transport in the liquid phase

Concentration of species i in the liquid phase can be evaluated from the conservation law. For a liquid phase, the conservation law is expressed in a per molar basis (Equation 3.37).³¹

$$\frac{\partial c_i}{\partial t} = -\nabla \cdot \mathbf{N}_i + R_i \quad (3.37)$$

$$R_i = R_{h,i} + R_{ct,i} \quad (3.38)$$

Steady-state is assumed making the $\frac{\partial c_i}{\partial t}$ to be zero. Dissolved species, however, undergo various reactions and R_i is thus divided to $R_{h,i}$ and $R_{ct,i}$. $R_{h,i}$ represents volumetric rate of species formation, or consumption, arising from homogeneous reactions (R1, R2, R3, R4). $R_{ct,i}$ represents source, or sink, originating from charge-transfer reactions (COER, HER, OER). R_i will be evaluated in later sections.

Total flux, \mathbf{N}_i , in a liquid phase is further extended for species migration. Migration is applicable to species that carry a non-zero charge. Nernst-Planck equation is used for the description of this flux. Its derivation follows from Maxwell-Stefan equations, which describe the balance between the diffusional driving force acting on species i and the frictional force between species i and j . To abridge the derivation, Equation 3.39 directly presents the resulting diffusional flux, \mathbf{J}_i . This flux arises due to various driving forces such as a gradient in pressure, temperature, or chemical potential. In this case, only electrical and concentration gradients are considered. Finally, it is assumed that the electrolyte solution is dilute and ideal.

$$\mathbf{J}_i = -c\mathcal{D}_i\nabla x_i - c_i z_i \mathcal{D}_i \frac{F}{RT} \nabla \phi_l \quad (3.39)$$

In Equation 3.39, \mathcal{D}_i is diffusivity of species i in the solvent at infinite dilution. It is a tabulated value that can be found in literature. z_i is the charge number of species i , F is Faraday's constant, and ϕ_l is the electrolyte potential.^{30,31}

The molar flux of species in the electrolyte is then given in Equation 3.40 by recalling the definition of diffusional flux (Equation 3.6). This equation is known as Nernst-Planck equation. Terms on the right-hand side represent diffusion, migration, and convection, respectively.³¹

$$\mathbf{N}_i = -c\mathcal{D}_i^{\text{eff}}\nabla x_i - c_i z_i \mathcal{D}_i^{\text{eff}} \frac{F}{RT} \nabla \phi_l + c_i \mathbf{u} \quad (3.40)$$

In Equation 3.40, \mathcal{D}_i can be substituted with $\mathcal{D}_i^{\text{eff}}$ which represents effective diffusivity of species i applicable to a porous domain. $\mathcal{D}_i^{\text{eff}}$ is evaluated based on $f(\epsilon, \tau)$. To evaluate $f(\epsilon, \tau)$, we use the Bruggeman model (subsection 3.2.1).

Finally, assuming electroneutrality, the K^+ distribution can be computed using the charge conservation equation presented in Equation 3.41.

$$\sum_{i=1}^n c_i z_i = 0 \quad (3.41)$$

$$(3.42)$$

3.2.4. Homogeneous reactions in the liquid phase

Homogeneous reactions occurring in the liquid phase were already introduced in the subsection 2.5.1. All these reactions, including the water self-ionization, are modelled as rate reactions that can proceed in both forward and backward directions. The following equations present the net reaction rate for each reaction.

$$r_{R1} = k_1 c_{\text{CO}_2(\text{aq})} c_{\text{OH}^-} - k_{-1} c_{\text{HCO}_3^-} \quad (3.43)$$

$$r_{R2} = k_2 c_{\text{HCO}_3^-} c_{\text{OH}^-} - k_{-2} c_{\text{CO}_3^{2-}} \quad (3.44)$$

$$r_{R3} = k_3 c_{\text{CO}_2(\text{aq})} - k_{-3} c_{\text{H}^+} c_{\text{HCO}_3^-} \quad (3.45)$$

$$r_{R4} = k_4 c_{\text{HCO}_3^-} - k_{-4} c_{\text{H}^+} c_{\text{CO}_3^{2-}} \quad (3.46)$$

$$r_{\text{RW}} = k_w - k_{-w} c_{\text{OH}^-} c_{\text{H}^+} \quad (3.47)$$

The rate of species formation or consumption, $R_{h,i}$, is obtained by multiplying the net reaction rate with a stoichiometric coefficient of species i in the considered reaction.⁴⁰

$$R_{h,i} = \nu_{i,R1} r_{R1} + \nu_{i,R2} r_{R2} + \nu_{i,R3} r_{R3} + \nu_{i,R4} r_{R4} + \nu_{i,\text{RW}} r_{\text{RW}} \quad (3.48)$$

When a reaction occurs in a porous medium, the reaction rate must be adjusted. The net reaction rate presented above is a volume based where this volume corresponds to the liquid volume. The equations above can be applied to the electrolyte channel without any modification. However, when

describing the reaction rate inside the CL, each net reaction rate, e.g. r_{R1} , must also be related to the liquid fraction. Thus, net reaction rate of R1 is obtained as in Equation 3.49, where $\epsilon_{l,CL}$ stands for the liquid porous fraction of the CL. Reaction rate for the remaining equations is obtained analogously.³²

$$r_{R1} = \epsilon_{l,CL}(k_1 c_{CO_2,(aq)} c_{OH^-} - k_{-1} c_{HCO_3^-}) \quad (3.49)$$

3.2.5. Electrochemical reactions

To describe the electrochemical reactions, the equilibrium potential is calculated from Nernst equation (Equation 3.50).

$$E_{eq} = E^0 + \frac{RT}{n_e F} \ln \left(\frac{a_O^{v_O}}{a_R^{v_R}} \right) \quad (3.50)$$

In Equation 3.50, n_e represents stoichiometric number of electrons involved in the charge-transfer reaction, a and v refer to activity and stoichiometric coefficient of oxidized, O , and reduced, R , form of species, respectively.²³

To find the the equilibrium potential for COER, terms in the Nernst equation have to be adjusted according to reaction stoichiometry. As pointed out in subsection 2.5.1, the alkaline pathway dominates the COER and we thus follow this stoichiometry. However, if we strictly follow this stoichiometry, we find that the $E_{eq,COER}$ is different to that often published in the COER literature. The COER literature often provides the $E_{eq,COER}$ as follows.

$$E_{eq,COER} = E_{COER}^0 - \frac{\ln(10)RT}{F} \text{pH} \quad (3.51)$$

$$(3.52)$$

If the stoichiometry of the alkaline pathway was followed then the equation above is missing the following term: $-\frac{RT \ln(K_w)}{F}$, where K_w is equilibrium constant for water dissociation. This is a common misinterpretation in the COER literature as also Nesbitt *et al.*²⁵ point out. The missing term arises in cases where alkaline COER is presented as the main CO evolution reaction, but the expression for the equilibrium potential is derived from the acidic COER.²⁵ Despite the missing term, we use the expression for the equilibrium potential, as presented above. This is because the kinetic parameters derived by these authors are directly related to the poorly defined $E_{eq,COER}$ and are thus self consistent.

Further, in the derivation of the equilibrium potential, the activity of H^+ , or OH^- , was set equal to its concentrations. Activity of water was assumed to be unity. Activity of both CO_2 and CO were neglected. To find the equilibrium potential for HER, similar assumptions as above are considered. The alkaline pathway is considered. Equation 3.53 gives the formulation for $E_{eq,HER}$.

$$E_{eq,HER} = E_{HER}^0 - \frac{\ln(10)RT}{F} \text{pH} \quad (3.53)$$

To find the equilibrium potential for HER, similar assumptions as above are considered. The acidic pathway is considered. Equation 3.54 gives the formulation for $E_{eq,HER}$.

$$E_{eq,OER} = E_{OER}^0 - \frac{\ln(10)RT}{F} \text{pH} \quad (3.54)$$

Next, Equation 3.55 defines overpotential, η , in respect to the applied electrode potential, E . η expresses the extra potential on top of the equilibrium potential necessary to drive an electrochemical reaction.²³

$$\eta = E - E_{eq} \quad (3.55)$$

In this work, the current density is calculated based on the activation overpotential, η_a , as in Equation 3.56. In Equation 3.56 ϕ_s stands for electric potential (solid) and ϕ_l stands for electrolyte potential (liquid).⁴¹

$$\eta_a = \phi_s - \phi_l - E_{eq} \quad (3.56)$$

Relation between overpotential and current density can be described with Butler-Volmer kinetic expressions. Different approximate forms of the current-overpotential relation exist such as the Tafel equation or Butler-Volmer equation. However, since the CO₂ electrolyzers are highly dependent on the local concentration, often, the original form of the current-overpotential equation (Equation 3.57) is used.^{6–10,23}

$$i = i_0 \left(\frac{c_O}{c_O^*} e^{-\frac{\alpha F}{RT} \eta} - \frac{c_R}{c_R^*} e^{\frac{(1-\alpha)F}{RT} \eta} \right) \quad (3.57)$$

Above, i stands for the net current of a certain charge-transfer reaction. That is, it is the difference between cathodic and anodic current. Cathodic current is represented by the first term in the above equation, while the anodic current is represented by the second. c_O and c_R stand for the concentration of oxidized and reduced species form, and c_O^* and c_R^* stand for reference concentration of oxidized and reduced species form. i_0 stands for exchange current and α stands for transfer coefficient. Both these coefficients can be found by fitting the experimental data.²³

Current is for experimental and modelling purposes normalized to unit area. This yields local current density, j^{loc} . Adjusting concentration dependent Butler-Volmer equation for COER, HER, OER results in Equation 3.58, Equation 3.59, and Equation 3.60, respectively, where j_0 denotes exchange current density.

$$j_{\text{COER}}^{\text{loc}} = j_{0,\text{COER}} \frac{c_{\text{CO}_2,(\text{aq})}}{c_O^*} e^{-\frac{\alpha_{\text{COER}} F}{RT} \eta_{a,\text{COER}}} \quad (3.58)$$

$$j_{\text{HER}}^{\text{loc}} = j_{0,\text{HER}} e^{-\frac{\alpha_{\text{HER}} F}{RT} \eta_{a,\text{HER}}} \quad (3.59)$$

$$j_{\text{OER}}^{\text{loc}} = j_{0,\text{OER}} e^{\frac{\alpha_{\text{OER}} F}{RT} \eta_{a,\text{HER}}} \quad (3.60)$$

Since potentials across the cell are applied such that CO₂ is reduced in the CL, anodic component will be negligible in respect to cathodic component of the Butler-Volmer equation for the reduction reaction, and vice versa for the anodic reaction. Thus, at the cathode, c_R is set to zero, and at the anode, c_O is set to zero. Following the stoichiometry, c_O for COER is set to $c_{\text{CO}_2,(\text{aq})}$. Reference concentration, c_O^* , is set to 1 M. The choice of reference concentration is not arbitrary but follows from the conditions at which the kinetic parameters were derived. Thus, since we use the kinetic parameters reported by Weng *et al.*,⁹ we need to use the same reference concentration as they did. Both HER and OER are assumed to be dependent only concentration of water which follows from the stoichiometry. Water supply is assumed to be unlimited. Thus, their concentration dependency is omitted by setting the c_O/c_O^* , or c_O/c_R^* , equal to 1.

Finally, Faraday's law is used to relate the current density to species formation or consumption as follows.²³

$$R_{ct,i} = \frac{j_{\text{COER}}^{\text{loc}} \nu_{i,\text{COER}} a_s}{2F} + \frac{j_{\text{HER}}^{\text{loc}} \nu_{i,\text{HER}} a_s}{2F} + \frac{j_{\text{OER}}^{\text{loc}} \nu_{i,\text{OER}}}{4F} \quad (3.61)$$

From Equation 3.61 follows that the net rate of species formation is expressed on volume basis which is achieved by multiplying the current density with specific area, a_s . a_s represents specific surface area per volume thus having the unit of m^2m^{-3} . $\nu_{i,\text{COER}}$, $\nu_{i,\text{HER}}$, and $\nu_{i,\text{OER}}$ represent stoichiometric coefficients of species i in the corresponding reaction.

From the above equations follow that so-expressed current density is specific to each grid point in the solver. It is also referred to as local current density. Often, however, geometrical current density, i.e.

current over the visible geometrical surface area, is used. To convert between local current density and geometrical current density, Equation 3.62 must be used. Analogously, HER and OER can be converted.

$$j_{\text{COER}} = \frac{a_s \int_0^L \int_W^{W_{\text{GDL}}} j_{\text{COER}}^{\text{loc}} dx dy}{L} \quad (3.62)$$

Above, j_{COER} corresponds to the COER geometrical current density. L , W , and W_{GDL} correspond to electrolyser length, electrolyte width, and CL width, respectively. For better understanding, these length scales are visualized in **Figure 3.1**.

3.2.6. Charge-transfer

Conservation law applies to charge as well. Since the steady-state is assumed, accumulation of charge will be in all cases zero. Depending on a phase, i.e. liquid or solid, charge carriers are either chemical species of non-zero charge or electrons, respectively. The gas phase does not contain any charged particles and thus does not conduct any current.

Regarding GDL, it is assumed that nor electrolyte, nor source, or sink of charge are present, consequently, charge conservation simplifies only to the flux of charge carriers (Equation 3.63).

$$\nabla \cdot \mathbf{j}_{\text{GDL}} = 0 \quad (3.63)$$

Current density in GDL, \mathbf{j}_{GDL} , is calculated from Ohm's law (Equation 3.64), where the electric field is substituted with the negative gradient of electric potential.⁴¹

$$\mathbf{j}_{\text{GDL}} = -\sigma_{\text{GDL}}^{\text{eff}} \nabla \phi_s \quad (3.64)$$

In the description above, effective conductivity, $\sigma_{\text{GDL}}^{\text{eff}}$, is introduced to take into account properties of porous GDL. This conductivity originates from GDL conductivity, σ_{GDL} , which is a tabulate value. $\sigma_{\text{GDL}}^{\text{eff}}$ is thus only corrected with the $f(\epsilon, \tau)$ which is evaluated using the Bruggeman model (subsection 3.2.1). In CL, two phases, liquid electrolyte and solid electrode, are present. This leads to $\mathbf{j}_{l,\text{GDL}}$ and $\mathbf{j}_{s,\text{GDL}}$ which represent current density in liquid and solid phase. Source and sink of charge are determined from electrochemical reactions. In the solid phase, electrochemical reactions are treated as a sink since the electrons coming from the GDL are being consumed in the reactions at the solid-liquid interface. On the other hand, in the liquid phase, electrochemical reactions are treated as a source, because electrons from GDL are transferred to the $\text{CO}_{2,(\text{aq})}$ to yield CO. Or analogically in case of HER. Equation 3.65 summarizes this reasoning and presents the charge conservation law for CL.⁴¹

$$\nabla \cdot \mathbf{j}_{s,\text{CL}} = \nabla \cdot (-\sigma_{s,\text{CL}}^{\text{eff}} \nabla \phi_s) = -a_s j_{\text{COER}} - a_s j_{\text{HER}} = -\nabla \cdot \mathbf{j}_{l,\text{CL}} = -\nabla \cdot (-\sigma_{l,\text{CL}}^{\text{eff}} \nabla \phi_l) \quad (3.65)$$

$\sigma_{s,\text{CL}}^{\text{eff}}$ and $\sigma_{l,\text{CL}}^{\text{eff}}$ are corrected for porosity of CL analogously to $\sigma_{\text{GDL}}^{\text{eff}}$. $\sigma_{s,\text{CL}}$ is a tabulated value. $\sigma_{l,\text{CL}}$ is calculated from the average ion conductivity according to Equation 3.66, where \bar{c}_i stands for average concentration.⁴¹

$$\sigma_{l,\text{CL}} = \frac{F^2}{RT} \sum_i z_i^2 \mathcal{D}_i \bar{c}_i \quad (3.66)$$

Nor sink, nor source of charge is present in the electrolyte domain. The conservation law thus reduces to Equation 3.67, where \mathbf{j}_{EL} stands for current density in electrolyte. \mathbf{j}_{EL} is found from electrolyte conductivity, σ_{EL} , using the Equation 3.68 and σ_{EL} is found from ionic concentration using Equation 3.69.

$$\nabla \cdot \mathbf{j}_{\text{EL}} = 0 \quad (3.67)$$

$$\mathbf{j}_{\text{EL}} = -\sigma_{\text{EL}} \nabla \phi_l \quad (3.68)$$

$$\sigma_{\text{EL}} = \frac{F^2}{RT} \sum_i z_i^2 \mathcal{D}_i \bar{c}_i \quad (3.69)$$

To remark, \bar{c}_i could appear in the final equation describing the charge conservation, however, in our model, it is treated as a constant. This means that we first compute the conductivity ($\sigma_{i,CL}$ and σ_{EL}), and this value is taken as a constant. In the next step the constant conductivity is used to compute the current density. This repeats in each iteration. It is briefly elaborated on in subsection 3.3.5.

3.2.7. Gas flow inside the gas diffusion layer

Commonly, the gas flow through a porous GDL is described with Darcy's law.^{6,7,9,10} Equation 3.70 presents this law. It is an empirical relation between velocity field \mathbf{v} and pressure gradient ∇p with constants of proportionality that are material specific. Fluid is assumed to be Newtonian and flow to be characterized by small Reynolds number.⁴²⁻⁴⁴

$$\mathbf{v} = -\frac{\kappa^{\text{eff}}}{\mu_g} \nabla p \quad (3.70)$$

Above, κ^{eff} refers to the effective permeability of a porous medium and μ_g refers to dynamic viscosity of a gas in GDL. κ^{eff} further corrects for porous properties via Equation 3.71, where κ^0 is the value of permeability from literature.⁴⁵

$$\kappa^{\text{eff}} = \kappa^0 \frac{\epsilon_{\text{GDL}}^3}{(1 - \epsilon_{\text{GDL}})^2} \quad (3.71)$$

To solve for the pressure and velocity, Darcy's law is combined with continuity equation (conservation of mass) presented in Equation 3.72, where steady state and constant density is assumed.⁴⁴

$$\nabla \cdot \mathbf{v} = 0 \quad (3.72)$$

3.2.8. Electrolyte and gas velocity profile

In this model we assume that the gas and liquid velocity profile in the gas and electrolyte channel are not influence by the electrolyser operation. Therefore, it is not necessary to solve for these profiles using numerical model, but we can solve these profiles analytically.

Since both modelled domains are rectangular and CO₂ electrolysers are often operated in a laminar flow regime, velocity profiles can be easily found by solving the equation describing the Poiseuille flow (Equation 3.73).

$$0 = -\frac{dp}{dy} + \mu \frac{d^2 u_y}{dx^2} \quad (3.73)$$

Above, $\frac{dp}{dy}$ is a pressure drop across the length of a channel and μ is the fluid viscosity. Equation 3.73 originates from Navier-Stokes equations where number of assumption were added. Thus, the flow is assumed to be steady, acceleration free, and fully developed at the inlet. Fluid is assumed to be incompressible. Direction of the fluid flow is set parallel to the y -axis as shown in **Figure 3.1**.

Electrolyte velocity profile

Equation 3.74 provides the two required boundary conditions. These are no slip boundary conditions. W and Z represent the width and thickness of the electrolyte channel. These are visualized in **Figure 3.1**. When the Equation 3.73 and Equation 3.74 are solved, Equation 3.75 is obtained, where μ_l represents electrolyte viscosity.

$$u_y|_{x=0} = 0 \quad u_y|_{x=W} = 0 \quad (3.74)$$

$$u_y = \frac{x^2}{2\mu_l} \frac{dp}{dy} - \frac{Wx}{2\mu_l} \frac{dp}{dy} \quad (3.75)$$

To define the liquid velocity magnitude, firstly the Reynolds number, Re , is chosen. To define the Re , hydraulic diameter is used. Using the Re , we can then express the average velocity, \bar{u} , as in Equation 3.76, where ρ_l is density of the electrolyte. The advantage of defining the \bar{u} via the Re is that we always control the validity of the Poiseuille flow which holds for roughly $Re > 1$ and $Re < 2000$.

$$Re = \frac{2\bar{u}\rho_l WZ}{\mu_l (W + Z)} \quad (3.76)$$

To couple the solved velocity profile (Equation 3.75) with \bar{u} , we can use the definition of an average of a function. When adjusted for our case Equation 3.77 is obtained.

$$\bar{u} = \frac{1}{W} \int_0^W u_y dx = -\frac{W^2}{12\mu_l} \frac{dp}{dy} \quad (3.77)$$

The final function describing the velocity profile (Equation 3.78) is obtained by expressing the $\frac{1}{\mu} \frac{dp}{dy}$ from Equation 3.77 and substituting it into Equation 3.75. Velocity component in x direction is not considered.

$$u_y = -\frac{6\bar{u}}{W^2} x^2 + \frac{6\bar{u}}{W} x \quad (3.78)$$

Gas velocity profile

To find a velocity profile inside the gas channel, $u_{y,g}$, Poiseuille flow is solved again using the two no slip boundary conditions (Equation 3.79). New symbols in Equation 3.79 stand for width of the subsequent domains. These are visualized in **Figure 3.1**.

$$u_{y,g} \Big|_{x=W+W_{GDL}+W_{GDL}} = 0 \quad u_{y,g} \Big|_{x=x=W+W_{GDL}+W_{GDL}+W_{GAS}} = 0 \quad (3.79)$$

$$(3.80)$$

To find average gas velocity, \bar{u}_g , we start by assuming, first, a certain desired value of CO_2 conversion, $X_{CO_2,asmp}$, second, a certain maximum current density, $j_{COER,asmp}$. Usually, low value of $X_{CO_2,asmp}$ and a high value of $j_{COER,asmp}$ is used. Such choice leads to the electrolyser operating at excess of gaseous CO_2 . Using the two assumed values, we can then express \bar{u}_g as in Equation 3.81. L represents the length of the electrolyser and p_{abs} represents the absolute operating pressure.

$$\bar{u}_g = \frac{j_{COER,asmp} LZ}{2F} \frac{1}{X_{CO_2,asmp}} \frac{RT}{p_{abs}} \frac{1}{W_{GAS} Z} \quad (3.81)$$

The following explains how the equation for \bar{u}_g is obtained:

- $\frac{j_{COER,asmp} LZ}{2F}$

First, this term converts the assumed value of current density to absolute current. Second, this term converts the amount of CO_2 consumed to mol s^{-1} . The 2 in the denominator refers to two electrons consumed per one molecule of CO_2 . $j_{COER,asmp}$ is always equal to 250 mA cm^{-2} .

- $\frac{1}{X_{CO_2,asmp}}$

This term determines the amount of extra gaseous CO_2 that will be fed to the electrolyser.

- $\frac{RT}{p_{abs}}$

This term converts the consumed CO_2 from mol s^{-1} to $\text{m}^3 \text{ s}^{-1}$ (volumetric flow rate of CO_2).

$$\bullet \frac{1}{W_{\text{GAS}}Z}$$

This term converts the volumetric flow rate to \overline{u}_g .

To clarify, the $X_{\text{CO}_2, \text{asmp}}$ could be achieved only if no mass transfer or other limitations occurred in the electrolyser. Thus, in reality, we could expect the $X_{\text{CO}_2, \text{asmp}}$ to be lower than the real CO_2 conversion. However, $X_{\text{CO}_2, \text{asmp}}$ can be still conveniently used to control the magnitude of the gas flow rate when aiming for a certain CO_2 conversion.

Once the \overline{u}_g is calculated, the gas velocity profile is derived analogously to the electrolyte velocity profile as described above. Thus, Equation 3.82 provides the final equation directly. Velocity component in x direction is not considered.

$$u_{y,g} = -\frac{6\overline{u}_g}{W_{\text{GAS}}^2}(x - W - W_{\text{GDL}} - W_{\text{GDL}})^2 + \frac{6\overline{u}_g}{W_{\text{GAS}}}(x - W - W_{\text{GDL}} - W_{\text{GDL}}) \quad (3.82)$$

In regards to the industrial and laboratory electrolyser. When comparing two electrolyser of different lengths, we want the ratio of the two gas flow rates to be equal to the ratio of the two electrolyser lengths. That is, 2 times longer electrolyser should have 2 times larger gas flow rate. Equation 3.81 satisfies this condition if both $X_{\text{CO}_2, \text{asmp}}$ and $j_{\text{COER, asmp}}$ are set to the same value in each electrolyser.

3.3. Model development and description

The model was developed in a step-by-step fashion starting from 1D. The 1D model only considered CL and GDL and it was set up according to the model developed by Weng *et al.*⁹ The validity of this model was determined by comparing its results with the Weng's model (section C.1). Then, the CL and GDL were extended to 2D to a length scale below 1 mm. Then, the remaining domains were added. Then, the electrolyser length was scaled up.

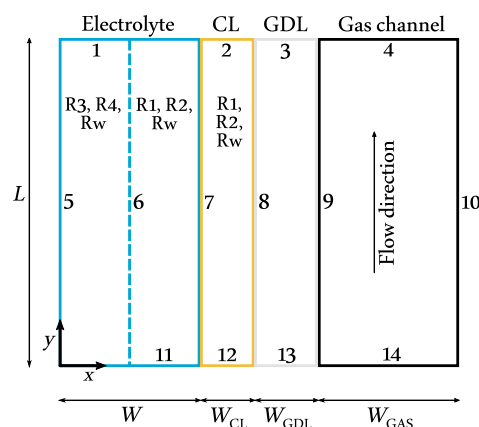


Figure 3.1: Scheme of the modelled electrolyser domains. Boundaries are labelled such that they correspond to the boundary conditions in **Table 3.4**.

Figure 3.1 provides the scheme of the final model. At the left boundary of the electrolyte, anode with a fixed equilibrium potential is placed. This anode generates a flux of H^+ ions equivalent to the amount of current flowing through the cathode. Anode is set up in this way, so that maximum current is limited only by the cathode, which is the main focus of this study. Electrolyte channel is divided into two halves where not all the homogeneous reactions are included. This is elaborated on in subsection 3.3.5. The CL and GDL follow the principle described in section 2.4 and section 2.5. Phenomena included in each domain are summarized in **Table 3.1**.

This model corresponds to a GDE based electrolyser equipped with a bipolar membrane (**Figure 2.1b**). It can be also claimed that this model corresponds to the microfluidic arrangement (**Figure 2.1d**).

3.3.1. Boundary conditions

Boundary conditions are summarized in **Table 3.4**, where the index of the boundary corresponds to the index of the boundary in **Figure 3.1**. \mathbf{n} is the unit vector normal to a boundary. $+\mathbf{n}$ takes a direction in the positive x or y direction. $-\mathbf{n}$ takes a direction in the negative x or y direction. To illustrate, $-\mathbf{n} \cdot \mathbf{J}_{CO_2|g/l}$ in case of electrolyte species at the boundary 8 represents a molar flux entering the CL domain.

3.3.2. Model parameters

Model parameters are presented in **Table 3.6** summarized at the end of this chapter. These parameters were mostly chosen such that they correspond to the laboratory electrolyser developed in our research group.

3.3.3. Initial values

Initial values are computed and summarized in **Table 3.5** for all the dependent variables (**Table 3.1**). Here we provide only the initial values applicable to the case most often modelled. Initial values for the other modelled cases are presented in Appendix A.

Table 3.4: Applied boundary conditions. The firstly occurring terms are elaborated on in subsection 3.3.3 and subsection 3.3.5. Boundary index correlates with the boundary label in **Figure 3.1**

	Boundary index	Boundary condition
Electrolyte species	1	$\mathbf{n} \cdot D_i \nabla c_i = 0$
	2 & 12	$-\mathbf{n} \cdot (\mathbf{J}_i + \mathbf{u}c_i) = 0$
	5	$-\mathbf{n} \cdot (\mathbf{J}_i + \mathbf{u}c_i) = 0, -\mathbf{n} \cdot \mathbf{J}_{c_{H^+}} = \frac{j_{OER}^{loc}}{F}$
	6	$c_{i,left} = c_{i,right}$
	8	$-\mathbf{n} \cdot \mathbf{J}_{CO_2 g/l} = k_{CO_2}(H_{CO_2}p_{CO_2} - c_{CO_2,(aq) g/l}), -\mathbf{n} \cdot \mathbf{J}_i = 0$
	11	$c_i = c_{i,initial}$
Potential distribution	1 & 11	$-\mathbf{n} \cdot \mathbf{j}_{EL} = 0$
	2 & 12	$-\mathbf{n} \cdot \mathbf{j}_{s,CL} = -\mathbf{n} \cdot \mathbf{j}_{i,CL} = 0$
	3 & 13	$-\mathbf{n} \cdot \mathbf{j}_{GDL} = 0$
	5	$\phi_s = \ln(e^{E_{eq,OER,initial}} + aux) V, -\mathbf{n} \cdot \mathbf{j}_{EL} = j_{OER}^{loc}$
	9	$\phi_s = E_{eq,HER,initial}$
Pressure in GDL	3 & 13	$-\mathbf{n} \cdot \rho \mathbf{v} = 0$
	8	$-\mathbf{n} \cdot \rho \mathbf{v} = -k_{CO_2}(H_{CO_2}p_{CO_2} - c_{CO_2,(aq) g/l})M_{CO_2} + \frac{a_s \int_W^{W+W_{CL}} j_{COER}^{loc} dx}{2F} M_{CO} + \frac{a_s \int_W^{W+W_{CL}} j_{HER}^{loc} dx}{2F} M_{H_2}$
	9	$p = p_{initial}$
Gaseous species	3 & 10 & 13	$-\mathbf{n} \cdot \mathbf{J}_i^m = 0$
	4	$-\mathbf{n} \cdot \rho D_i \nabla \omega_i = 0$
	8	$-\mathbf{n} \cdot \mathbf{J}_i^m = -k_{CO_2}(H_{CO_2}p_{CO_2} - c_{CO_2,(aq) g/l})M_{CO_2} + \frac{a_s \int_W^{W+W_{CL}} j_{COER}^{loc} dx}{2F} M_{CO} + \frac{a_s \int_W^{W+W_{CL}} j_{HER}^{loc} dx}{2F} M_{H_2}$
	14	$\omega_i = \omega_{i,initial}$

Table 3.5: Initial values for 0.5 M KHCO₃ electrolyte saturated with CO₂ (i.e. in equilibrium with $p_{CO_2} = 1$ atm).

Variable	Initial value	Unit	Variable	Initial value	Unit
$c_{CO_2,(aq)}$	32.97	mM	$E_{eq,HER,initial}$	-0.44	V
$c_{HCO_3^-}$	498.31	mM	ϕ_l	0	V
$c_{CO_3^{2-}}$	0.84	mM	ϕ_s	-0.44	V
c_{OH^-}	$3.54 \cdot 10^{-4}$	mM	ω_{CO_2}	99.99	%
c_{H^+}	$2.82 \cdot 10^{-5}$	mM	ω_{CO}	0.001	%
$p_{initial}$	0	Pa	ω_{H_2}	0.001	%
$E_{eq,OER,initial}$	0.79	V	ω_{N_2}	0.008	%

Electrolyte species: c_i

The electrolyte entering the electrolyser contains 0.5 M KHCO₃ and is in equilibrium with a CO₂ gas. This gas is at atmospheric pressure. Combining Henry's law and assuming zero net reaction rate for the homogeneous reactions, R1, R2, and Rw, initial values for all the dissolved species can be found.

Electric and electrolyte potential: ϕ_s, ϕ_l

Following the Equation 3.55 and Equation 3.57, current density is only proportional to the difference between ϕ_l and ϕ_s . As a result, ϕ_l is arbitrarily set to 0 V. To readily reach the convergence, current flowing through the cell should be minimal. This condition is satisfied when the potentials are chosen such that η_a is approaching 0 V. This reasoning is visualized in **Figure 3.2**. Initial E_{eq} is calculated from the Equation 3.50. To note, $\eta_{a,COER}$ will be above zero, which should lead to oxidation. However, the anodic part of the Butler-Volmer equation is neglected (Equation 3.58).

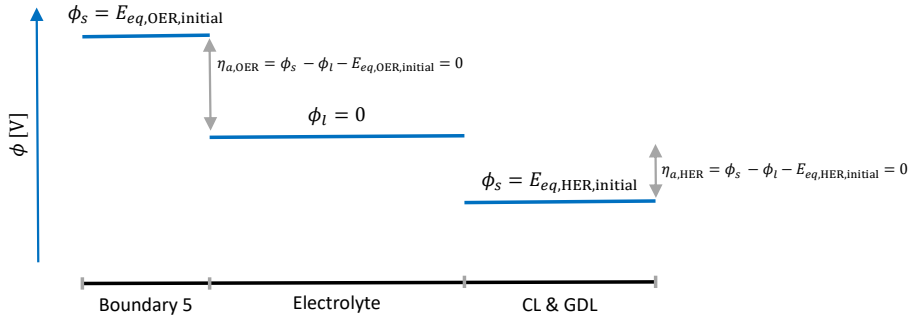


Figure 3.2: Initial setup of ϕ_s and ϕ_l inside the electrolyser. Potentials are chosen such that minimal amount of charge flows through the electrolyser, which, according to Equation 3.57, implies setting η_α to zero.

Gaseous species: ω_i

Initial values are set equal to the inlet value.

Relative pressure: p

It is assumed that the homogeneous reactions at the initial current density will not result in a significant mass sink at the gas/liquid interface. Thus p is set to 0 Pa in the entire domain.

3.3.4. Optional solver configurations

When all the equations and parameters are setup in COMSOL, achieving solver convergence even at low current densities around 1 to 10 mA cm⁻² becomes the main challenge. Most notably, the electrolyte channel was identified as the main source of errors. This is probably because numerous driving forces are acting on each species. These forces are convection, gradient in electric potential and gradient in concentration. Further, species concentration is coupled with fast homogeneous reactions. This all then introduces significant instability into the model.

To achieve model convergence, we came up with number of modifications. These are described in Appendix B and relate to solver description, physics description and others. These methods helped to improve the solver convergence, however, they are not included in the final model. This is because they were surpassed by better solutions.

3.3.5. Solver configuration

All the different methods described in the appendix were finally surpassed by the following set of modifications. These are included in the final model.

Current density description

To satisfy the current conservation, we have two options how to describe the current density vector in the liquid phase (\mathbf{j}_{EL} and $\mathbf{j}_{i,CL}$). First, the \mathbf{j} can be described using the Nernst-Planck equation as in Equation 3.83 (correspond to "Tertiary current distribution" in COMSOL). Second, the \mathbf{j} can be described using the Ohm's law as in Equation 3.84 (correspond to "Secondary current distribution" in COMSOL).⁴¹

$$\mathbf{j} = F \sum_i \left(z_i (-c \mathcal{D}_i^{\text{eff}} \nabla x_i - c_i z_i \mathcal{D}_i^{\text{eff}} \frac{F}{RT} \nabla \phi_l) \right) \quad (3.83)$$

$$\mathbf{j} = -\sigma \nabla \phi_l \quad (3.84)$$

The first equation is more precise and allows to better capture variations in current with respect to distribution of species. The disadvantage of the second equation is that electrolyte and liquid phase in the CL are described with one constant value of conductivity.

However, using the Nernst-Planck equation to describe the \mathbf{j} introduces another condition on the c_i . This thus increases complexity of the model. This means that better meshing is required and the computational time increases. Therefore, in our model, the \mathbf{j} is described using the Equation 3.84.

Using the Ohm's law, the electrolyte potential ϕ_l can be made independent of c_i . As a result, we can completely omit the K^+ ions from the numerical modelling. This thus decreases the number of degrees of freedom and increases the computational speed. We therefore assume that electroneutrality condition is imposed by K^+ ions and that c_{K^+} can be found from this condition.

The question remains what value to use for the liquid conductivity. The number of charged species in the electrolyte increases as a result of COER, HER and OER stoichiometry. The type of charged species changes as a result of homogeneous equations. Thus, we can try to increase the precision by calculating the conductivity based on the average species concentration. Equation 3.85 gives the equation for conductivity used in our model. \bar{c}_i stands for average species concentration calculated by integration across the whole domain.

$$\sigma = \frac{F^2}{RT} \sum_i z_i^2 \mathcal{D}_i \bar{c}_i \quad (3.85)$$

To remark, the \bar{c}_i is omitted from the differentiation. It thus appears as a constant in the solver. This means that σ is firstly computed and then the Equation 3.84 uses σ as a fixed value. This repeats in every iteration.

Logarithmic concentrations

In cases when solver did not converge, concentration of certain species would lower to even negative values. This happened when homogeneous reactions were added to the model. To tackle this issue, it is possible to model logarithm of a concentration rather than the concentration itself. The logarithm of a concentration can attain both positive and negative values and when converted back, it will always result in a concentration with a positive value. Another advantage follows from the reduction in the order of magnitude. To illustrate, c_{H^+} can span over easily more than six orders of magnitude, but when modelled as a logarithmic concentration, its span is reduced to one order of magnitude. Thus, new variables, C_i , with the following properties are introduced.

$$C_i = \ln c_i \quad c_i = e^{C_i} \quad (3.86)$$

Often a gradient of a concentration is required. To find this gradient when using logarithmic concentrations, gradient of an outer and then an inner function has to be evaluated. For this end, chain rule is used. When simplified to only 1D case, the chain rule gives Equation 3.87, then, generalizing for 2D gives Equation 3.88

$$\frac{dc_i}{dx} = \frac{de^{C_i}}{dx} = \frac{de^{C_i}}{dC_i} \frac{dC_i}{dx} = e^{C_i} \frac{dC_i}{dx} \quad (3.87)$$

$$\nabla c_i = \nabla e^{C_i} = e^{C_i} \nabla C_i \quad (3.88)$$

Using the above, the total flux, \mathbf{N}_i , modifies to Equation 3.89.

$$\mathbf{N}_i = -e^{C_i} \mathcal{D}_i^{\text{eff}} \nabla C_i - e^{C_i} z_i \mathcal{D}_i^{\text{eff}} \frac{F}{RT} \nabla \phi_l + e^{C_i} \mathbf{u} \quad (3.89)$$

When homogeneous reactions are added, the species conservation takes the form as in Equation 3.90, where, for simplicity, only one first order reaction is shown.

$$\nabla \cdot \left(-e^{C_i} \mathcal{D}_i^{\text{eff}} \nabla C_i - e^{C_i} z_i \mathcal{D}_i^{\text{eff}} \frac{F}{RT} \nabla \phi_l \right) + e^{C_i} \mathbf{u} \cdot \nabla C_i = k e^{C_i} \quad (3.90)$$

This adjustment is introduced to COMSOL by modifying the equations settings. Using the logarithmic concentrations significantly improves the solver convergence. We also verified this approach against the model with real concentration and no differences between these two models were found.

Segregated solver

During the solver computation, we often observed high oscillations in the error. These oscillations then often caused the model to crash. These oscillations can be expected since the modelled system is highly nonlinear. For example, product of COER influences its own generation. Further, these oscillations are enhanced via current conservation. This means that oscillations at the cathode, will inevitably influence the anode and its local environment and vice versa. This makes the model very unstable. To tackle this issue, the model is divided to two parts shown in **Figure 3.3**. The whole electrolyser is thus solved in three steps follows.

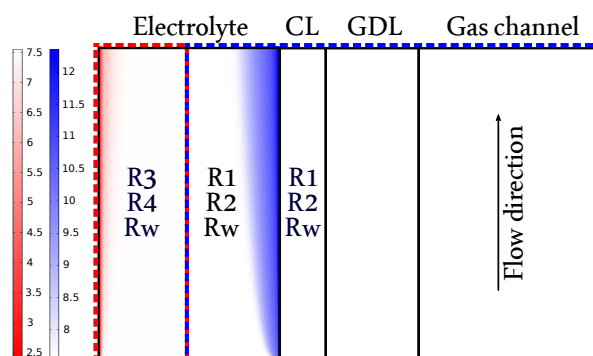


Figure 3.3: Scheme of the modelled domains and their partition to the two modelled blocks. These block are highlighted by the red and blue dashed lines. Each block is firstly solved separately and then both at once. The background in the electrolyte domain is the pH profile solved at $j_{\text{tot}} = 204 \text{ mA cm}^{-2}$. Low pH region establishes in the vicinity of anode (OER producing H^+ ions), while high pH region establishes around the cathode (COER and HER producing the OH^- ions). Labels of the homogeneous reactions highlight at which parts which reactions are included.

1. Right half of the electrolyte channel, CL, GDL, and gas channel (blue block).
Alkaline reactions R1, R2, and Rw are included as the pH will be above the bulk value.
2. Left half of the electrolyte channel (red block).
Acidic reactions R3, R4, and Rw are included as the pH will be below the bulk value.
3. All domains together (blue and red block).
When the convergence criteria are not met, the solver repeats the sequence starting from step 1.

Neglecting acidic reactions in favor of alkaline reactions around the cathode has been previously used in models developed by Kas *et al.*⁶ or Yang *et al.*⁷ Here, we extend the analogous reasoning to the anode, that is, to the acidic region. Influence of the acidic reactions in the alkaline environment, and vice versa, is thus neglected.

For this approach to work, each half of the electrolyte channel is represented by its own physics interface in COMSOL. From this follow two major advantages. First, cathode and anode can be solved separately which makes the model more stable. Second, each half of the electrolyte channel can be set up differently. We use this to separate the homogeneous reactions which thus reduces the coupling between the species.

Finally, this approach holds well when the boundary layers do not evolve further than to the middle of the channel. If, however, certain species influences the bulk concentration in the middle, it is accounted for in the step 3 of the solver sequence. The solver also repeats until the converge criteria are met, meaning that the species distribution is not influenced by middle imaginary boundary.

Damping

Another adjustment reducing the oscillations in the error is the damping factor. Starting from an initial value, or the previous solution, U_0 , to find a solution for the next iteration U_1 COMSOL uses damped Newton method (Equation 3.91).

$$U_1 = U_0 + \lambda_s \delta U \quad (3.91)$$

Above, δU is Newton's step and λ is the damping factor. From Equation 3.91 follows that λ determines the extent to which a new solution contributes to the solution of the next iteration. This means that lower λ reduces the oscillations, however, it increases the computational time.

While the automatic solver firstly uses low value of λ , in the following iterations, it can increase unreasonably. This then leads to overshoots in the error and the model crashes. To restrict these oscillations, we use manual damping and set λ to a constant value of 0.2.

Auxiliary sweep

To solve the model, initial values must be chosen properly. This means that we cannot solve the model for an arbitrary current density immediately, because the real solution is usually far from the solution at zero current and a model would not converge. Thus, the applied voltage across the cell is increased in the step by step fashion using the auxiliary sweep. In this model, the potential at the anode, ϕ_s , is increased using this sweep as in Equation 3.92, while the potential at the further end of the GDL is kept constant.

$$\phi_s = \ln(e^{E_{eq,OER,initial}} + aux) \quad (3.92)$$

Above, the aux represents a variable that serves as an input for the auxiliary sweep. aux is thus automatically increased from 0 to 30 with a step of 0.25 saving the solution at each step. This choice of aux values is arbitrary and follows from the way we define the function describing the anode potential. Here, we use a logarithmic function since the current relates exponentially to the potential (Equation 3.57). This allows us to decrease the potential step size logarithmically while the current increases. This makes the initial values for the next potential step to be closer to the real solution. If, however, the solver would crash, the auxiliary sweep itself can further refine the step size. This makes the auxiliary sweep a robust technique. Auxiliary sweep is terminated when $j_{COER} > 200 \text{ mA cm}^{-2}$

Meshing

Finally, choice of meshing is also crucial. A mapped mesh is used in regions where extremely fine meshing is required. Triangular meshing is used in regions where coarser mesh can be used. Mapped meshing for the liquid species is preferred. This is because the triangular meshing cannot efficiently reach the desired resolution in x direction while at the same time keeping the resolution in y direction coarser. This becomes especially important when varying the geometry scales. **Figure 3.4** shows the meshing near the electrolyser outlet region.

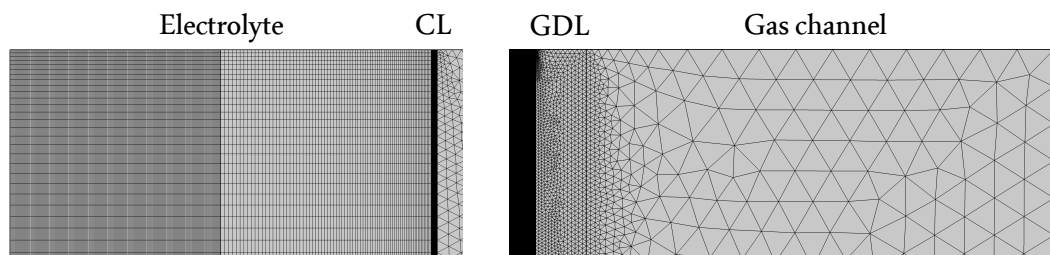


Figure 3.4: Meshing in each domain. Very fine meshing is used in the left half of the electrolyte channel, coarser in the right half. CL uses mapped meshing. Fine triangular mesh is used in the GDL and a coarser one in the gas channel use triangular meshing.

To close up, the model usually contains around 1 to 5 million degrees of freedom, which requires a lot of computational power. This model is thus solved using high performance cluster (hpc11). COMSOL version 5.5 with MUMPS solver is used.

3.3.6. Solver configuration for CO₂ electrolyser with 1 m length

Scaling up the electrolyser length, means scaling up the number of degrees of freedom and thus both computational time and required memory. Further, to reach a desired current density, auxiliary sweep must be used. This means solving for all the current densities below the required one which further increases the computational time. To illustrate, solving electrolyser 10 cm long takes around 5 days and requires almost 100 GB of memory. Both metrics would substantially increase as we aim to model electrolyser larger by factor of 10.

To tackle this issue, we propose a solution sequence shown in **Figure 3.5**. In this approach, the solution sequence goes as follows. 1, The whole length of the electrolyser, 100 cm, is divided into 25 subcells each 4 cm long (**Figure 3.5a**). 2, In the first subcell, auxiliary sweep is used to reach a desired potential or current density (**Figure 3.5b**). 3, Solution is saved and the desired potential is kept constant for all the following subcells. 4, Outlet profile of the first subcell is transferred to the inlet of the second subcell. This sets the inlet boundary conditions. Outlet profile of the first subcell is mapped onto the whole corresponding domain of the second subcell. This sets the initial values for the second subcell. (grey and black arrows in **Figure 3.5**, respectively). 5, The second subcell is solved and solution is saved (**Figure 3.5c**). 6, The step 4 repeats and the third subcell is solved (**Figure 3.5d**). This approach repeats until all the remaining subcells are solved.

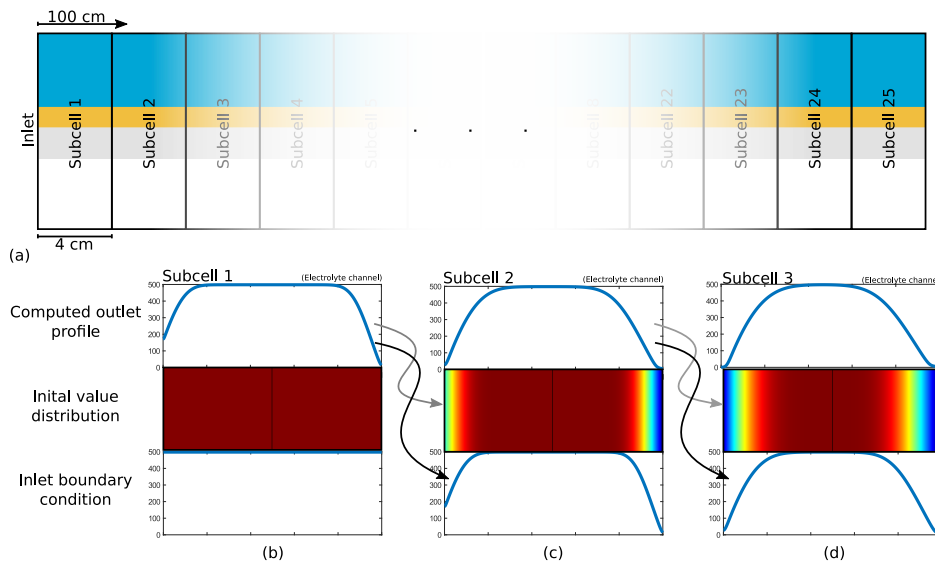


Figure 3.5: Solver solution sequence for the long electrolyser ($L = 100$ cm). (a) whole length of the modelled electrolyser and its partition to 25 subcells. (b) first subcell is solved with auxiliary sweep. Grey and black arrows indicate the way at which the outlet profile as transferred to the second subcell. The second subcell uses this profile as boundary and initial conditions. (c) second subcell is solved at the fixed potential. Outlet profile is transferred to the third subcell. (d) third subcell is solved at the fixed potential. This approach repeats for all the remaining subcells.

This solution sequence requires few assumptions. First, concentration of species at the outlet does not influence concentration at the inlet, meaning that diffusion over this boundary is neglected. Species transport in the electrolyte channel, in the y direction, is thus assumed to be dominated by convection. The same reasoning can be applied to gaseous species in the gas channel. No-flux boundary condition is used for species transport at the inlet, and outlet respectively, of the CL and GDL domains. Thus, species from one subcell cannot influence the species in the other subcell again, not even via diffusion. This may represent a decrease in accuracy for the CL and GDL domains which are dominated by diffusion. The approach was validated against the model full model using no subcells and the two results showed very little difference (section C.2).

The solver configuration is setup in the same manner as described in the earlier section above.

3.4. Quantifying electrolyser performance

In this section we define additional variables. These will be used to describe the performance of the CO₂ electrolyser.

Total current density: j_{tot}

$$j_{\text{tot}} = j_{\text{COER}} + j_{\text{HER}} \quad (3.93)$$

Faradaic efficiency: FE

FE represents a ratio of the charge consumed by COER to the total amount of charge consumed at the cathode. FE thus shows how efficiently the electrons supplied to the electrolyser are used.

$$\text{FE} = \frac{j_{\text{COER}}}{j_{\text{COER}} + j_{\text{HER}}} \quad (3.94)$$

CO₂ conversion: X_{CO_2}

To quantify the amount of gaseous CO₂ that is successfully converted to CO, we define a CO₂ conversion X_{CO_2} . X_{CO_2} represents a ratio of the amount of CO produced to the total amount of gaseous CO₂ entering the electrolyser. This provides an information on the amount of gaseous CO₂ at the outlet and is sometimes referred to as single pass conversion.

$$X_{\text{CO}_2} = \frac{\frac{j_{\text{COER}} L}{2F}}{\int_{W+W_{\text{CL}}+W_{\text{GDL}}}^{W+W_{\text{CL}}+W_{\text{GDL}}+W_{\text{GAS}}} u_{g,y} \frac{p_{\text{absolute}}}{RT} x_{\text{CO}_2} dx} \quad (3.95)$$

Share of CO₂ consumption

To evaluate how efficiently the dissolved CO_{2,(aq)} is utilised, we define a metric called Share of CO₂ consumption. This metric quantifies the percentage of CO_{2,(aq)} consumed in COER, labeled just as COER, and R1, labeled just as R1. These two metrics are normalized by the total amount of CO_{2,(aq)} consumed, that is COER + R1. This evaluation is based on the work by Larrazábal *et al.*⁴⁶ and the definitions go as follows.

$$\text{COER} = \frac{\frac{j_{\text{COER}} L}{2F}}{\frac{j_{\text{COER}} L}{2F} + \int_0^L \int_{W/2}^W r_{R1} dx dy + \int_0^L \int_W^{W+W_{\text{CL}}} r_{R1} \epsilon_{l,\text{CL}} dx dy} \quad (3.96)$$

$$\text{R1} = \frac{\int_0^L \int_{W/2}^W r_{R1} dx dy + \int_0^L \int_W^{W+W_{\text{CL}}} r_{R1} \epsilon_{l,\text{CL}} dx dy}{\frac{j_{\text{COER}} L}{2F} + \int_0^L \int_{W/2}^W r_{R1} dx dy + \int_0^L \int_W^{W+W_{\text{CL}}} r_{R1} \epsilon_{l,\text{CL}} dx dy} \quad (3.97)$$

As follows from the above, both types of the CO₂ consumption are complementary and thus sum up to 100%. The two contributions are reported together in one plot illustrated in **Figure 3.6**. To complete the picture, X_{CO_2} is added to signify the amount of CO_{2,(aq)} consumed.

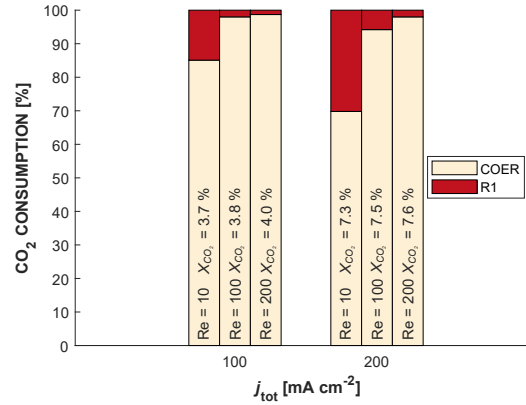


Figure 3.6: An example plot for Share of CO₂ consumption. COER refers to the amount of CO_{2,(aq)} consumed in COER, while R1 refers to the amount of CO_{2,(aq)} consumed in R1. For easier understanding, both types of consumption are normalized by the total amount of CO_{2,(aq)} consumed, i.e. COER + R1. X_{CO₂} roughly indicates the magnitude of the consumed amounts.

Variable as a function of electrolyser length: $j_{\text{COER}}(y)$

In this study we will often focus on the length of the electrolyser. To efficiently visualize a variable in an dependence on the electrolyser length (y -axis), we define a new variable as in Equation 3.98 which is now added a suffix (y). This definition is only reserved for the CL. In Equation 3.98, j_{COER} as a function of the electrolyser length is given as an example. This variable thus represents an average over the x -axis inside the CL and is plotted as a function of y .

$$j_{\text{COER}}(y) = \int_W^{W_{\text{CL}}} a_s j_{\text{COER}} dx \quad (3.98)$$

This definition allows us to study how a certain variable changes with the electrolyser length without a need of a 2D plot. We can thus compare variables between different models more precisely. We can also investigate more variables at once while keeping the evaluation concise and on point.

Visualizing current density inside the CL

To visualize a current density inside the CL, we can directly use the $j_{\text{COER}}^{\text{loc}}$. However, so defined current density has a counter intuitive magnitude. Thus, to simplify the evaluation, if the $j_{\text{COER}}^{\text{loc}}$ is reported in a 2D plot, it will be adjusted as shown in Equation 3.99. Same holds for HER. The name of the variable will remain unchanged.

$$j_{\text{COER}}^{\text{loc}} = a_s W_{\text{CL}} j_{\text{COER}}^{\text{loc}} \quad (3.99)$$

Local faradaic efficiency: FE^{loc}

Local distribution of FE inside of the CL will be referred to as FE^{loc} . This enables to identify regions inside the CL which favor COER less than HER

$$\text{FE}^{\text{loc}} = \frac{j_{\text{COER}}^{\text{loc}}}{j_{\text{COER}}^{\text{loc}} + j_{\text{HER}}^{\text{loc}}} \quad (3.100)$$

3.5. Approach to answering the research question

To answer the research questions, we always adjust the model parameters to fit the current needs. Most of the model parameters are always the same and are given in the **Table 3.6**. Model which uses all the parameters as given by the **Table 3.6** is referred to as Level 2 model. The following sections only focus on the parameters that were modified.

Model validation

This model is adjusted in accordance to the experimental electrolyser reported by Verma *et al.*⁴⁷ Material specific parameters were neglected.

- Non-saturated electrolyte (**Table A.1**)
- $W = 1.5$ mm
- $Re = 2.56$
- $L = 15$ mm

Local salting-out effect

Two model are compared here. One excludes the salting-out effect. It has the H_{CO_2} described with Equation 3.28 and is referred to as Excluding. One includes the salting-out effect. It has the H_{CO_2} described with Equation 3.36 and is referred to as Including.

Parametric study

In the parametric study we take a three level approach. This means that each parameter is investigated at three different magnitudes. The middle level fully corresponds to the parameters given **Table 3.6** and is referred to as Level 2 model.

- Liquid flow rate: $Re = 10/100/200$
- Operating pressure: $p_{abs} = 1/3/5$ atm
- Electrolyser length: $L = 5/20/40$ mm
- Catalyst layer porosity: $\epsilon_{l,CL} = 40/50/60$ %

Long electrolyser

Two models are compared here. One reflecting the long electrolyser, one reflecting the short electrolyser. To investigate the effect of X_{CO_2} , the gas flow rate is varied using the assumed CO_2 conversion, $X_{CO_2,asmp}$. Due to the way $X_{CO_2,asmp}$ relates to the gas flow (subsection 3.2.8), this parameters determines the proportionally same flow rate to both electrolyser. Increasing the value of $X_{CO_2,asmp}$, corresponds to increasing X_{CO_2} .

- $X_{CO_2,asmp} = 10/50/80/120/160\%$

Long electrolyser

This electrolyser is modelled using the approach describe in subsection 3.3.6. 25 subcells are modelled in total. Parameters describing one subcell go as follows.

- $Re = 200$
- $L = 40$ mm

Short electrolyser

This electrolyser is modelled as a whole. It corresponds to one subcell of the long electrolyser.

- $Re = 200$
- $L = 40$ mm

Strategies to improve the performance of long electrolysers

Two models are compared in each section. Both models in each section are supposed to reflect a real CO_2 electrolyser, thus the parameters where chosen as follows and apply to each model.

- $X_{CO_2,asmp} = 80\%$
- $L = 100$ mm

The second of the two models is further adjusted as follows.

Fluid flow configuration

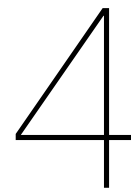
The electrolyte flow is adjusted to flow in the opposite direction. This corresponds to the countercurrent regime.

Variable catalyst loading

$j_{0,COER}$ and $j_{0,HER}$ are linearly decreased from their original value at the inlet to 20% of their original value at the outlet. This corresponds to i_0 linear model.

Table 3.6: Model parameters

	Parameter	Value	Unit	Source
Operating parameters	p_{abs}	1	atm	-
	T	293.15	K	-
	c_{KHCO_3}	500	mM	-
	Re	100	-	-
	pH around RHE	$-\log(c_{\text{H}^+,\text{initial}})$	-	-
Geometry	L	20	mm	-
	W	0.254	mm	-
	W_{CL}	3.5	μm	Experimental
	W_{GDL}	325	microm	48
	W_{GAS}	3	mm	-
	Z	5	mm	-
Electrolyte	ρ_l	998	kg m^{-3}	49
	μ_l	$1 \cdot 10^{-3}$	Pa s	49
	$\mathcal{D}_{\text{CO}_2,\text{(aq)}}$	$1.910 \cdot 10^{-9}$	$\text{m}^2 \text{s}^{-1}$	9
	$\mathcal{D}_{\text{HCO}_3^-}$	$1.185 \cdot 10^{-9}$	$\text{m}^2 \text{s}^{-1}$	9
	$\mathcal{D}_{\text{CO}_3^{2-}}$	$9.230 \cdot 10^{-9}$	$\text{m}^2 \text{s}^{-1}$	9
	$\mathcal{D}_{\text{OH}^-}$	$5.293 \cdot 10^{-9}$	$\text{m}^2 \text{s}^{-1}$	9
	\mathcal{D}_{H^+}	$9.311 \cdot 10^{-9}$	$\text{m}^2 \text{s}^{-1}$	9
CL	$\epsilon_{s,\text{CL}}$	50	%	-
	$\epsilon_{l,\text{CL}}$	$1 - \epsilon_{s,\text{CL}}$	%	-
	$\sigma_{s,\text{CL}}$	25	S m^{-1}	6
	r_{np}	$4 \cdot 10^{-8}$	m^{-1}	Experimental
	k_{CO_2}	$1.56 \cdot 10^{-2}$	m s^{-1}	6
	Saturation	100	%	-
GDL	ϵ_{GDL}	53	%	48
	σ_{GDL}	220	S m^{-1}	9
	κ^0	$1.72 \cdot 10^{-11}$	S m^{-1}	48
	λ	$2 \cdot 10^{-6}$	m	6
Gas	$\Delta_{\text{sol}} H_i$	19954	J mol^{-1}	35
	$H_{\text{CO}_2,\text{ref}}$	$3.4 \cdot 10^{-4}$	$\text{mol m}^{-3} \text{Pa}^{-1}$	35
	ρ_g	1.839	kg m^{-3}	50
	μ_g	$1.469 \cdot 10^{-5}$	Pa s	50
	$X_{\text{CO}_2,\text{asmp}}$	10	%	-
	$\mathcal{D}_{\text{CO}_2,\text{CO}}$	$1.52 \cdot 10^{-5}$	$\text{m}^2 \text{s}^{-1}$	9
	$\mathcal{D}_{\text{CO}_2,\text{H}_2}$	$6.46 \cdot 10^{-5}$	$\text{m}^2 \text{s}^{-1}$	9
	$\mathcal{D}_{\text{CO},\text{H}_2}$	$7.43 \cdot 10^{-5}$	$\text{m}^2 \text{s}^{-1}$	9
	$\mathcal{D}_{\text{CO}_2,\text{N}_2}$	$1.65 \cdot 10^{-5}$	$\text{m}^2 \text{s}^{-1}$	9
	$\mathcal{D}_{\text{CO},\text{N}_2}$	$2.02 \cdot 10^{-5}$	$\text{m}^2 \text{s}^{-1}$	9
	$\mathcal{D}_{\text{H}_2,\text{N}_2}$	$7.79 \cdot 10^{-5}$	$\text{m}^2 \text{s}^{-1}$	9
Electrochemistry	E_{COER}^0	-0.11	V	13
	$j_{0,\text{COER}}$	$4.71 \cdot 10^{-4}$	mA cm^{-2}	9
	α_{COER}	0.44	-	9
	E_{HER}^0	0	V	13
	$j_{0,\text{HER}}$	$1.16 \cdot 10^{-6}$	mA cm^{-2}	9
	α_{HER}	0.36	-	9
	E_{OER}^0	1.23	V	10
	$j_{0,\text{OER}}$	$6.21 \cdot 10^{-5}$	mA cm^{-2}	10
	α_{OER}	1.5	-	10



Results and Discussion

One of the main goals of this report is to expand the understanding of CO₂ electrolyzers. We start with a model validation where we compare predictions of our model to the experimental results and we explain the observed differences. We then provide further comparison to another 2D model reported in the literature. The section is concluded with an explanation of the observed phenomena at high current densities.

In the next section, we present the results of the parametric study. The focus is aimed at the effect of liquid flow rate, electrolyser length and operating pressure. We explain the obtained results and show whether any of these parameters could improve the electrolyser performance.

Successfully scaling up a CO₂ electrolyser is necessary if the carbon cycle should ever be closed. In the penultimate section, we present a model of an electrolyser that approaches industrial scales. The performance of such an electrolyser is compared to that of its laboratory counterpart and we close by discussing the drawn implications.

Finally, improving the performance of the CO₂ electrolyser is not only a question of the catalyst performance but the electrolyser configuration. Fluid flow arrangement and changing catalyst loading are investigated in the last section of this study.

4.1. Model validation

It is necessary to validate the model before we can discuss its implications. We thus adjust our model to match the a CO₂ electrolyser developed by Verma *et al.*⁴⁷ We compare current-voltage relationship (**Figure 4.1a**), and faradaic efficiency, FE, as a function of total current density, j_{tot} , (**Figure 4.1b**). We intentionally avoid plotting voltage in the second figure since not all the components of the electrolyser are included.

To put the results into a wider perspective, we also include data points from the other three sources. Two are experimental, and one is computational. Weng *et al.*⁹ developed a 1D computational model. Their model uses the same parameters as the experimental setup of Verma *et al.*⁴⁷

To make the analysis easier, we should firstly focus only on the low current magnitudes, that is, up to 40 mA cm⁻² (-0.8 V). Our model shows a reasonably good agreement with the published data at this magnitude. We could argue, that the impacts of various changes in the local cathode environment are not as strong as at higher currents and that these minor modifications in the local environment are well captured by the model. Especially, in the **Figure 4.1b**, we can see a substantial improvement in the description of FE when compared to the 1D model developed Weng *et al.*⁹ Because we use the same kinetic parameters, this discrepancy could be attributed to the fact that CL is in our model capturing one extra dimension. The extra dimension allows us to better predict the thickness of the developing HCO₃⁻ boundary layer (**Figure 4.3**). This leads to a more precise prediction of HCO₃⁻ flux into the CL and, in this specific case, to a better buffering of the local pH. The more buffered pH then leads to a higher rate of COER (explained later).

If we now consider higher current magnitudes, that is above 40 mA cm⁻² (more negative than -0.8 V), we observe that the model starts to deviate from the experimental results considerably. Especially, when it comes to the current-voltage relationship. The general trend in the experimental data shows

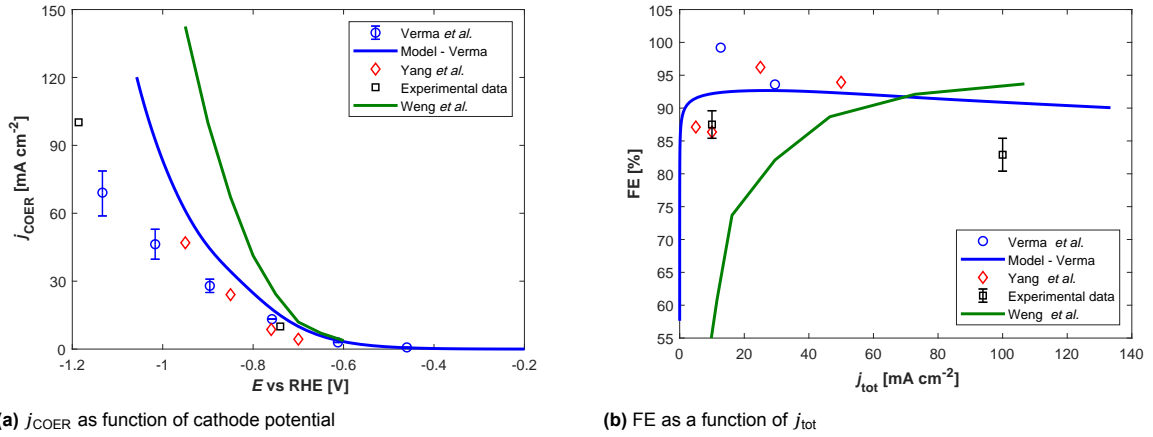


Figure 4.1: Comparison between the results obtained from our model, Model - Verma, and the experimental results published by Verma *et al.*⁴⁷ Electrolyte uses 0.5 M KHCO_3 and is not saturated with CO_2 . The liquid flow rate corresponds to $\text{Re}=2.6$, and the gas is fed in excess. The length of the electrolyser is 15 mm. Data published by Yang *et al.*,⁵¹ and the experimental data measured by Christel Koopman⁵² use GDE based electrolyser, but the geometry and the operating parameters are different. Data published by Weng *et al.*⁹ correspond to a numerical 1D model and are supposed to match the data reported by Verma *et al.*⁴⁷

j_{COER} linearly increasing with the cathode's potential indicating that the experiments are limited by conductivity. However, our model shows j_{COER} to be controlled kinetically which can be inferred from the exponential growth of j_{COER} . This indicates that our model might be missing an ohmic contribution. We could support this as follows. The predicted FE matches well with experimental data, especially around 60 mA cm^{-2} (Figure 4.1b). However, this match is poor in the current-voltage relationship, especially around and after 60 mA cm^{-2} (Figure 4.1a). We can claim that the extra ohmic drop would only change the current-voltage relationship, but not the FE. Thereafter, we could find a good match in both validation plots.

We can identify two possible sources of the missing ohmic contribution. First, it is the RHE positioning. In our model, we assume a null ohmic drop between the RHE and the CL. However, this ohmic drop may become relevant in the experimental setup. Second, and more likely, the computational models are missing to include phenomena that manifest in a form of high resistance. Here we provide two possible explanations.

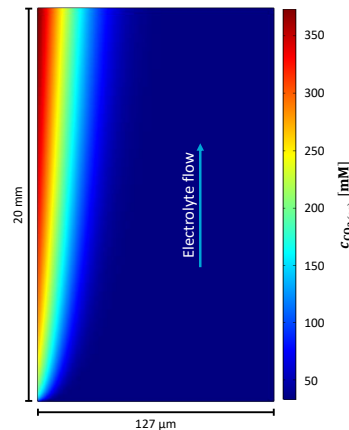


Figure 4.2: $\text{CO}_{2,\text{(aq)}}$ profile in one half of the electrolyte channel closer to the BPM. A result from Model-Verma at $j_{\text{COER}} = 205 \text{ mA cm}^{-2}$.

The second explanation could be related to modelling an electrolyser with a BPM. BPM transfer H^+ ions into the electrolyte channel which leads to a locally acidic pH. According to R3, the production of $\text{CO}_{2,\text{(aq)}}$ is then taking place in this region. This is confirmed by the model as shown in Figure 4.2. The local increase in $\text{CO}_{2,\text{(aq)}}$ then surpasses the solubility limit, which is around 33 mM, and could

subsequently lead to the formation of gas bubbles. This was experimentally confirmed by Yan *et al.*⁵³ and also in our research group. These gas bubbles then result in two changes. First, they stick to the BPM surface, second, they reduce the electrolyte cross-section available for ion conduction. Both of these factors increase ohmic resistance and neither is included in our model. This phenomenon is omitted for the sake of simplicity and could explain the missing ohmic contribution. The electrolyser used by Verma *et al.*⁴⁷ could suffer from the same problem although they do not use the BPM. They use an electrolyser setup analogous to the **Figure 2.1c** where the anode is producing the locally acidic pH. Consequently, this could also lead to gas formation and thus increased resistance.

Finally, H₂ formation at the cathode can also lead to formation of gas bubbles and subsequently to the increased ohmic contribution. However, this effect was also neglected in our model.

Considering FE only, **Figure 4.1b**, we could conclude that FE is well described in our model. Both Yang *et al.*⁷ and Weng *et al.*⁹ report that catalyst loading and the thickness of the CL can substantially affect the j_{COER} and thus the FE. A poorly set CL thickness could explain the variations in FE. Nevertheless, it is important that both experiments and the developed model agree on a downward trend in the FE.

4.1.1. Numerical and analytical/empirical predictions

In addition to the experimental validation, we can also compare our results to the analytical and empirical predictions. This can serve as very approximate validation and could indicate if the model provides any unrealistic conclusions. We can also try to indicate limitations of these predictions.

First, we compare thickness of the HCO₃⁻ boundary layer adjacent to the CL (**Figure 4.3**). Here we choose HCO₃⁻ ions for their buffering capability within the CL (section 4.2). We used the empirical Sherwood-Reynolds-Schmidt correlation, Sh-Re-Sc, as reported by Weng *et al.*⁹ This correlation does not take into account variation of the boundary layer thickness along the flow direction nor in respect to current density. The predicted thickness is around 50 μm and constant over the whole length of the channel. The 2D model captures the evolution of the boundary layer thickness and is able to better describe the flux of HCO₃⁻ ions into the CL. Both predictions are close to each other indicating that the 2D model is predicting the thickness well.

We also highlight the advantage of the 2D model. While the 1D model developed by Weng *et al.*⁹ used the Sh-Re-Sc correlation, we can show that what they describe corresponds to a position in the electrolyser around 18 mm far from the inlet.

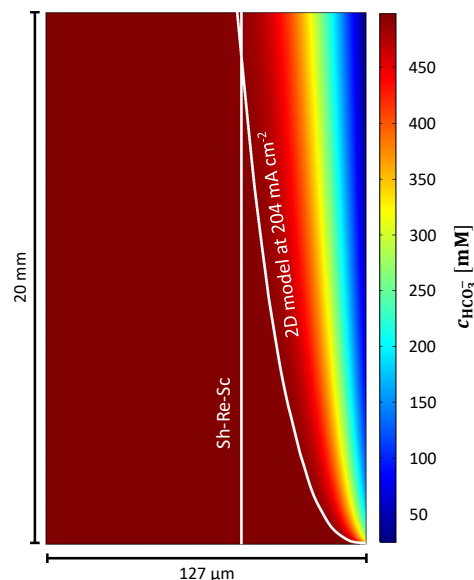


Figure 4.3: Boundary layer thickness calculated from the Sherwood-Reynolds-Schmidt correlation, Sh-Re-Sc, (empirical, described in subsection C.2.1) and the boundary layer thickness obtained from our 2D model (numerical). The numerical result is at $j_{\text{tot}} = 204 \text{ mA cm}^{-2}$. Both correspond to HCO₃⁻ ions. The boundary layer thickness in the 2D model is determined for points where $c_{\text{HCO}_3^-}$ reaches 99% of its feed concentration.

Second, we compare the CO₂ concentration profile, $c_{\text{CO}_2(\text{aq})}$, inside the CL to an analytical prediction (**Figure 4.4**). The two predictions match well close to the CL/GDL boundary, however, closer to the

electrolyte/CL boundary, the two predictions start to deviate more. We argue that this originates from the CO_2 initially dissolved in the electrolyte channel. The sink of $\text{CO}_{2,(\text{aq})}$ in the CL creates a gradient in the $c_{\text{CO}_{2,(\text{aq})}}$ between the electrolyte channel and the CL and thus diffusion forces the $\text{CO}_{2,(\text{aq})}$ to enter the CL. This is captured by the 2D model, but this effect is missing in the analytical prediction. To conclude, the differences between the two predictions are not significant. We can claim that also the prediction of $c_{\text{CO}_{2,(\text{aq})}}$ inside the CL is well described within our model.

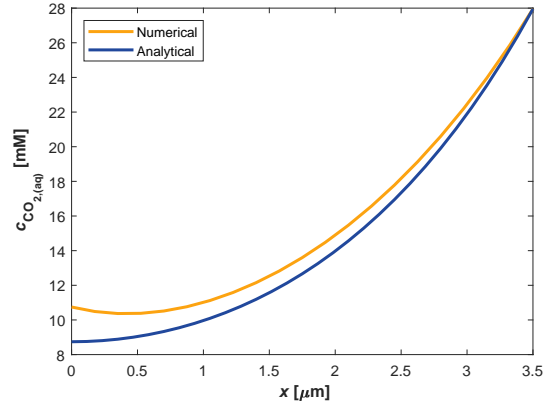


Figure 4.4: Distribution of the dissolved CO_2 , $c_{\text{CO}_{2,(\text{aq})}}$, as a function of position inside the CL, x . $0 \mu\text{m}$ refers to the electrolyte/CL boundary, and $3.5 \mu\text{m}$ refers to the CL/GDL boundary. Numerical stands for the distribution calculated from our 2D model. Analytical stands for the analytical approximation derived by Joe Blake (subsection C.2.1). These profiles correspond to $j_{\text{tot}} = 204 \text{ mA cm}^{-2}$ and are calculated in the middle of the electrolyser height ($y = 10 \text{ mm}$).

4.2. Phenomena governing the electrolyser performance

Before we discuss the observed j_{COER} distribution, we firstly break down the exact relationship between the current and other variables. Current is exponentially dependent on the activation overpotential, η_a , as follows from Equation 3.57. Further, we can expand η_a , in accordance with Equation 3.50 and Equation 3.56. When rearranging the terms we get Equation 4.1 and Equation 4.2 which describe COER and HER, respectively.

$$j_{\text{COER}}^{\text{loc}} = j_{0,\text{COER}} c_{\text{CO}_{2,(\text{aq})}} e^{\frac{\alpha_{\text{COER}} F E_{\text{COER}}^0}{RT}} e^{-\alpha_{\text{COER}} \text{pH} \ln 10} e^{-\frac{\alpha_{\text{COER}} F E}{RT}} \quad (4.1)$$

$$j_{\text{HER}}^{\text{loc}} = j_{0,\text{HER}} e^{\frac{\alpha_{\text{HER}} F E_{\text{HER}}^0}{RT}} e^{-\alpha_{\text{HER}} \text{pH} \ln 10} e^{-\frac{\alpha_{\text{HER}} F E}{RT}} \quad (4.2)$$

Analyzing the two equations above, we can now better understand how current relates to a specific variable. First, the exchange current density follows from the catalyst property and is thus constant throughout the whole CL. COER is directly dependent on the availability of the reactant resulting in $c_{\text{CO}_{2,(\text{aq})}}$.

The first exponential term in each equation above favours HER over the COER. This follows from the value of E^0 . Because the E_{COER}^0 is -0.11 V while E_{HER}^0 is equal to 0 V , the exponential term in COER is smaller than 1 whereas the exponential term in HER is equal to 1. The value of E^0 thus favours HER over COER.

The second exponential term in the equations above reveals how pH affects the current. The negative value in the exponential shows that increasing the pH is detrimental to both COER and HER. However, this effect is dependent on the value of transfer coefficient which is for COER equal to 0.44 and HER equal to 0.36. The absolute value of this exponential term is thus always lower in the case of COER. Here we find that higher pH favours the production of H_2 over the production of CO.

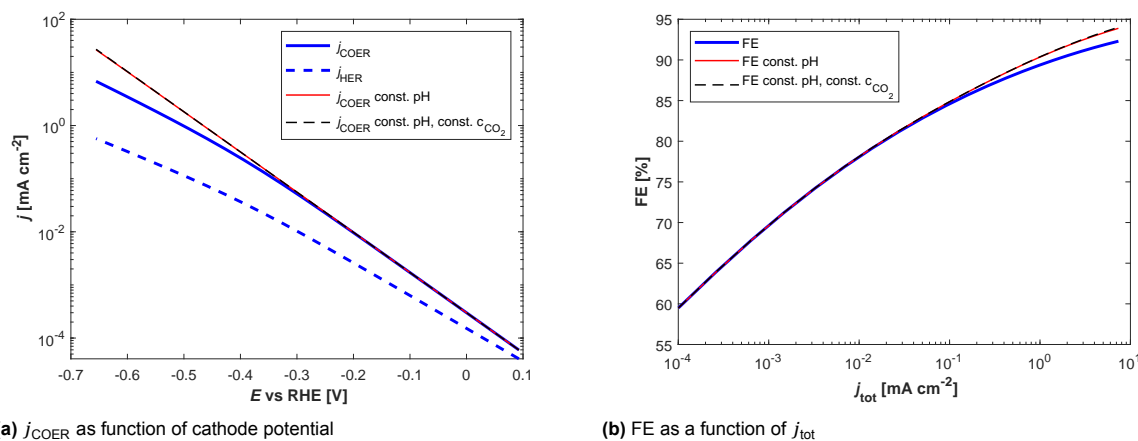
The last exponential term shows why the production of COER exceeds that of HER. The electrode potential, E , is always negative due to the way the voltage is applied across the cell. The exponential term then becomes positive and the extent to which the COER is favored over the HER is determined solely by the value of transfer coefficients. The higher the E , the more COER is favored.

We point out that such analysis is applicable for the current model. However, applicability to a real-world electrolyser may be questionable, because the validity of these equations can be questionable. This was discussed previously in the subsection 3.2.5.

In the next sections, the analysis is split into two sections. One deals with phenomena occurring at low currents, one at higher currents. All subsequent results are taken from the Level 2 model (section 3.5).

4.2.1. Behaviour at low current density $< 10 \text{ mA cm}^{-2}$

To better reveal the phenomena occurring at the low currents, we can use a semi-log axis to plot the j_{COER} and FE (Figure 4.5).



(a) j_{COER} as function of cathode potential

(b) FE as a function of j_{tot}

Figure 4.5: Behaviour at the low current magnitudes. For better visualization semi-log axis is used. Blue lines represent a metric as obtained from the model. Red line represents a metric if the pH inside the CL was maintained at its bulk value, but considers variation in $c_{\text{CO}_2,(\text{aq})}$. Black dashed line represents a metric if both pH and $c_{\text{CO}_2,(\text{aq})}$ inside the CL were maintained at their bulk values. To remark, the prediction around 0.1 V and 0 V which is because only the cathodic branch of the electrode reaction was considered (subsection 3.2.5).

We can expect an exponential relationship between current and electrode potential if the system is free of any mass transfer, conductivity, or other limitations. This follows from Equation 4.1. If we plot this relationship on a semi-log axis, we should then get a linear line. This linear line is visible in **Figure 4.5a**, however, it breaks down around $E = -0.35 \text{ V}$.

The deviation from this ideal performance can be solely attributed to the increasing pH. To prove this, we can compare the blue line and the red line in **Figure 4.5a**. We see that current increases and approaches a linear relationship if the pH was maintained at its bulk value. To judge the effect of reactant supply, we further include the black dashed line. We show that there is no difference between these two lines which indicates that the supply of $\text{CO}_2,(\text{aq})$ is sufficient. We can thus conclude that the decrease in current density can be solely attributed to the effect of pH. To add, average pH inside the CL increased from the bulk value of 7.55 to 8.9 across the considered potential range.

If we now inspect **Figure 4.5b**, we can see a substantial contribution of HER to the j_{tot} . This follows from the exponential terms summarized in Equation 4.1 and Equation 4.2. Both E^0 and pH favor HER and are especially relevant when E is close to zero. This thus explains why we see a low FE in the first half of the figure. However, as E increases, the ratio of COER to HER increases which follows from the last exponential terms in Equation 4.1 and Equation 4.2. That is why we see FE steadily increasing. We can also again see the detrimental effect of pH which by decreasing the j_{COER} results in the decrease of FE. Recall, that increasing pH is more detrimental to COER than to HER.

4.2.2. Behaviour at higher current density $> 10 \text{ mA cm}^{-2}$

At higher current densities, the influence of reactant supply, pH, and buffer supply becomes more relevant. To explain all, we firstly focus on the behaviour of HCO_3^- ions and OH^- ions around the CL. We can then explain the pH profile and $c_{\text{CO}_2,(\text{aq})}$ distribution inside the CL. Understanding these distributions, we can finally conclude with the current distribution and FE^{loc} .

Distribution of HCO_3^- flux and its interaction with OH^-

At moderate currents, flux of HCO_3^- ions into the CL is slightly decreasing along the CL and creates a depleted boundary layer of HCO_3^- in the electrolyte channel (**Figure 4.6a** and **Figure 4.6b**). This depleted boundary layer extends in the direction of the electrolyte flow and increases the diffusional path for HCO_3^- . Thus the HCO_3^- flux entering the CL decreases towards the end of the channel. This variation in HCO_3^- flux, however, is not very strong and the distribution of the R2 net reaction rate is uniform. All the OH^- buffering happens inside the CL.

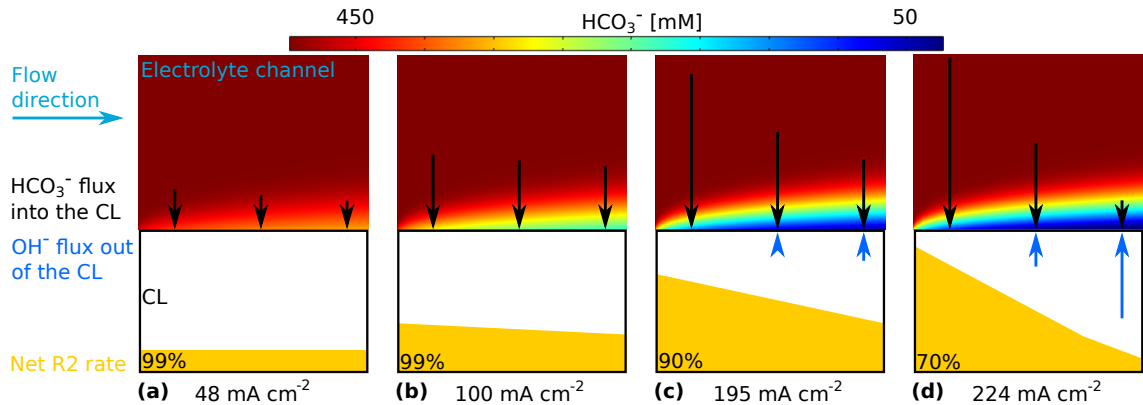


Figure 4.6: Behaviour of HCO_3^- and OH^- ions around and within the CL at various levels of j_{tot} . 2D profile shows $c_{\text{HCO}_3^-}$ distribution in the electrolyte channel. Black arrows show the flux of HCO_3^- ions and their size represents the magnitude of the HCO_3^- flux along the CL. Blue arrows show the flux of OH^- ions and their size represents the magnitude of the OH^- flux along the CL. Yellow stripe inside the CL rectangle shows the magnitude of the R2 net reaction rate and its distribution as a function of CL length. The percentage in the left corner refers to the amount of HCO_3^- reacted in R2 inside the CL with respect to the total amount of HCO_3^- reacted in R2 in both electrolyte channel and the CL.

At high currents, the flux of HCO_3^- ions into the CL deviates strongly between the inlet and the outlet regions and a substantial portion of OH^- escapes the CL (**Figure 4.6d**). In the inlet region, electrochemical reactions produce significant amount of OH^- which creates a significant sink for HCO_3^- in accordance to R2 (the yellow stripe). This results into a strong gradient in $c_{\text{HCO}_3^-}$ and thus a strong flux of the HCO_3^- ions into the CL (the first black arrow). Downstream, the flux of HCO_3^- into the CL decreases substantially (the other two black arrows) due to two reasons. First, the diffusional path for the HCO_3^- ions increases dramatically (2D plot). Second, the HCO_3^- ions are consumed in R2 before they reach the CL. This follows from the R2 rate quickly decreasing which then allows the OH^- ions to escape the CL (blue arrows). To note, both migration and diffusion drive the OH^- ions out of the CL, whereas, only diffusion drives the HCO_3^- ions into the CL. The OH^- ions thus enter the electrolyte channel and react with the HCO_3^- ions. Around 30% of the HCO_3^- ions are consumed outside of the CL (percentage). To summarize, the strong flux of HCO_3^- ions into the CL near the inlet causes the outlet region of the CL to be poorly buffered and the R2 reaction shifts from the CL to the electrolyte channel.

The maximum amount of HCO_3^- entering the CL happens at $j_{\text{tot}} = 195 \text{ mA cm}^{-2}$ (**Figure 4.6c**). Before this point, the production of OH^- ions creates a reasonable HCO_3^- sink and causes the flux of HCO_3^- to increase. After this point, the flux of HCO_3^- ions into the CL decreases. That is because the flux of OH^- ions outside of the CL increases (compare blue arrows in c and d) which thereafter diminishes the flux of HCO_3^- as explained in the paragraph above. This effect increases with increasing current and shows that pH buffering is less effective at high currents.

Distribution of pH and concentration of $\text{CO}_{2(\text{aq})}$ inside the CL at $j_{\text{tot}} = 224 \text{ mA cm}^{-2}$

Understanding the behaviour of HCO_3^- and OH^- ions, we can continue to explain the pH distribution (**Figure 4.7a**). The inlet region shows the lowest pH, because the buffer supply is the highest, while the outlet region shows the highest pH because the buffer supply is the lowest. This correlates well with the R2 rate presented earlier (**Figure 4.6d**), all resulting in the final pH profile. Increasing pH in the positive x -direction follows from the lowering supply of the HCO_3^- ions and a longer diffusion path for OH^- to leave the CL.

We can also compare the pH distribution obtained from our model to the pH distribution reported by

Kas *et al.*⁶ (**Figure 4.7b**). We see that both profiles are very much comparable. This verifies our model, but it also shows that the partially flooded CL (modelled by Kas *et al.*⁶) gives a very similar pH profile as the flooded CL (our model).

In the $c_{\text{CO}_2,(\text{aq})}$ distribution (**Figure 4.7c**), we can identify two distinct regions. First, we focus on a region near the electrolyte/CL boundary where $c_{\text{CO}_2,(\text{aq})}$ is significantly low. This follows from two, a high consumption of $\text{CO}_2,(\text{aq})$ in COER and an inefficient supply of $\text{CO}_2,(\text{aq})$ from the electrolyte channel. We could also say that $\text{CO}_2,(\text{aq})$ originating from the gaseous phase cannot diffuse to this boundary fast enough since it gets quickly consumed in COER or R1.

Second, we identify a region near the CL/GDL boundary where $c_{\text{CO}_2,(\text{aq})}$ reaches the maximum values. This locally increased concentration could be linked to the gas supply. In the current model, the gas is fed in excess which translates to a relatively high p_{CO_2} along the CL and to a rather constant flux of CO_2 across the gas/liquid boundary. This means that both the inlet and the outlet region feel a similar and relatively high flux of CO_2 .

Finally, the pH profile also determines the consumption of $\text{CO}_2,(\text{aq})$ in accordance to R1. However, the variance in $c_{\text{CO}_2,(\text{aq})}$ as a result of pH is hardly observable in **Figure 4.7c**. We can at least visualize the amounts of consumed $\text{CO}_2,(\text{aq})$ by plotting the R1 profile (**Figure D.1**).

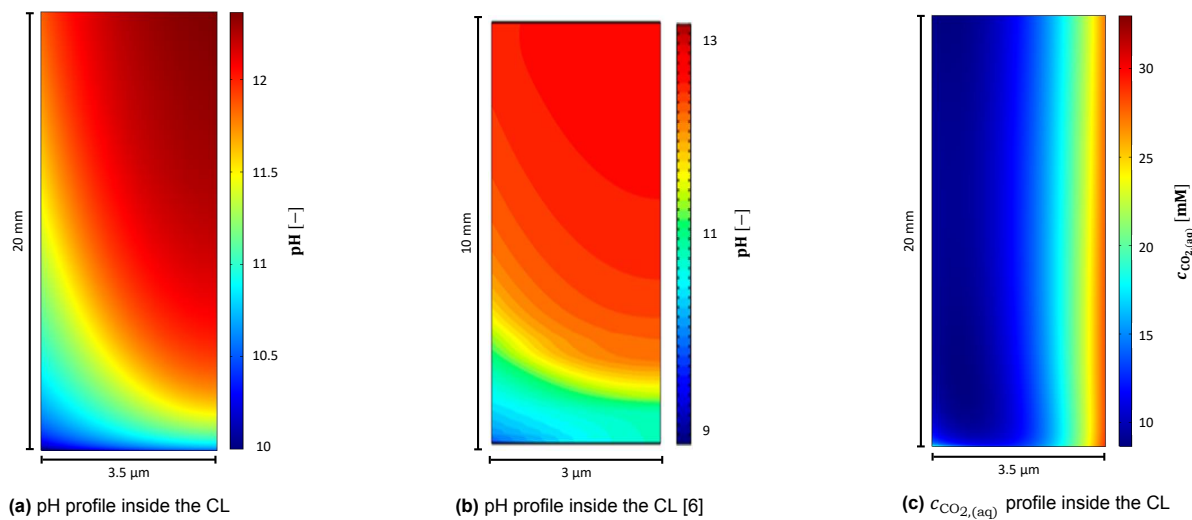


Figure 4.7: (a) pH distribution inside the CL at $j_{\text{tot}} = 224 \text{ mA cm}^{-2}$. (b) pH distribution as obtained by Kas *et al.*⁶ at $j_{\text{COER}} = 240 \text{ mA cm}^{-2}$ (c) $c_{\text{CO}_2,(\text{aq})}$ distribution inside the CL at $j_{\text{tot}} = 224 \text{ mA cm}^{-2}$. In each such plot the electrolyte is located on the left and GDL is on the right. Electrolyte and gas flow from bottom to the top. Here reported profiles can be used to explain the current distribution.

Current density distribution at $j_{\text{tot}} = 224 \text{ mA cm}^{-2}$

Various locally very active regions towards the COER are visible in **Figure 4.8a**. We can identify two such regions. First, a region near the inlet at the electrolyte/CL boundary retains its high performance due to, first and primarily, pH being relatively low (**Figure 4.6**). Second, the supply of $c_{\text{CO}_2,(\text{aq})}$ from the electrolyte plays a role. However, this supply decreases along the direction of the flow (**Figure D.2**) which originates from a longer diffusion pathway and an increasing rate of R1 outside the CL. The increase in rate of R1 follows from the flux of OH^- ions (**Figure 4.6d**). As a result, $j_{\text{COER}}^{\text{loc}}$ decreases along the electrolyte/CL boundary.

The second highly active region towards COER can be found near the CL/GDL boundary. This follows from the efficient supply of CO_2 from the gaseous phase which led to the increased $c_{\text{CO}_2,(\text{aq})}$ (**Figure 4.7c**).

However, $j_{\text{COER}}^{\text{loc}}$ is substantially low in the middle of the CL and further decreases towards the outlet. This follows from the combination of poor supply of $c_{\text{CO}_2,(\text{aq})}$ and a high pH.

Comparison of $j_{\text{COER}}^{\text{loc}}$ as obtained by Kas *et al.*⁶ is provided in **Figure 4.8b**. The major difference between these two profiles follows from Kas *et al.*⁶ using lower gas flow rates. A lower gas flow rate leads to a substantially lower supply of CO_2 along the direction of the flow and thus a substantial decrease in current in the same direction. Nevertheless, the authors considered a partially flooded CL

which means that far ends of the CL should still be fed by a gaseous CO_2 . In this regard, it is surprising to find a similar $j_{\text{COER}}^{\text{loc}}$ distribution.

Finally, **Figure 4.8c** shows the distribution of $j_{\text{HER}}^{\text{loc}}$. This distribution can be directly related to the pH profile, as follows from Equation 4.2 provided that the E is neglected. We see that the pH distribution (**Figure 4.7a**) matches well with $j_{\text{HER}}^{\text{loc}}$ distribution.

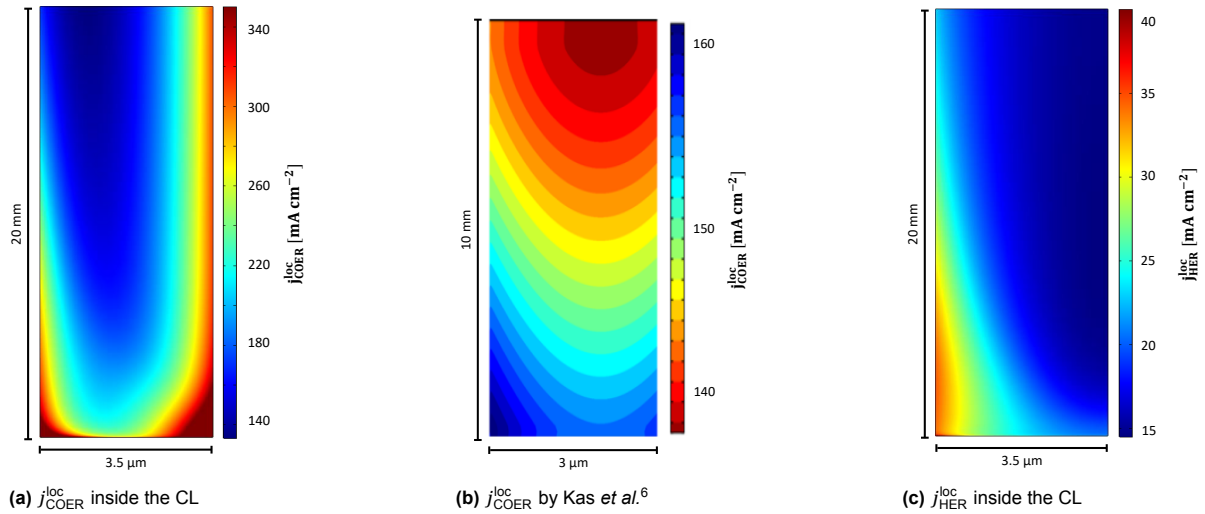


Figure 4.8: (a) and (c) shows $j_{\text{COER}}^{\text{loc}}$ and $j_{\text{HER}}^{\text{loc}}$, respectively, both at $j_{\text{tot}} = 224 \text{ mA cm}^{-2}$. Current density can overshoot in the corners due to edge effects. The scale is therefore manually adjusted, but it can underestimate the current density in these regions. (b) shows $j_{\text{COER}}^{\text{loc}}$ reported by Kas *et al.* at roughly similar electrode potential as the profiles in (a) and (c). Note that these authors used an inverted colour scheme.

Evolution of the FE^{loc} distribution

Here, we identify which parts of the CL are responsible for the decrease in FE **Figure 4.1b**. We can use the local distribution of faradaic efficiency, FE^{loc} (**Figure 4.9**) to identify that. At low current density, the FE^{loc} distribution is uniform which we could relate to the uniform distribution in the net R2 rate (**Figure 4.6a** and **Figure 4.6b**). At higher current density, the situation changes. The FE^{loc} is the least favourable around the electrolyte/CL boundary. This directly correlates with the distribution of the $c_{\text{CO}_2,(\text{aq})}$ (**Figure 4.7c**). We should remark that pH has rather same effect on the current distribution, see Equation 4.1 and Equation 4.2. pH is only slightly favoring HER, thus, pH effects will not be well reflected in the FE^{loc} distribution, unless the R1 becomes very relevant.

Figure 4.9e provides comparison to our model. This profile was reported by Kas *et al.*⁶ at around $j_{\text{COER}} = 750 \text{ mA cm}^{-2}$. The authors considered a high CO_2 conversion which means that the p_{CO_2} and thus the flux of CO_2 into the CL decreases in the flow direction. This explains why FE^{loc} decreases in the flow direction. However, the authors report no visible variations in FE^{loc} in the x -direction. This might be due to two reasons. First, the variations over x -direction are just negligible in respect to the variations over the y -direction. Second, because CL contains both gaseous and liquid phase, far end of the CL could be better supplied by the CO_2 since the resistance to mass transfer in the gaseous phase is significantly lower than in the liquid phase.

Based on the these findings, we see that the mass transfer of $\text{CO}_{2,(\text{aq})}$ into the electrolyte/CL region should be improved. This could be done by optimizing the mass transfer through the CL. Notably, the CL should be partially flooded CL. This would allow the CO_2 gas to reach even the farther end of the CL. As the mass transfer resistance in a gas phase is lower than in the liquid phase, we could expect more CO_2 to dissolve also in the farther region. Another solution might be to reduce the thickness of the CL. Only the high performing parts of CL could be retained. Finally, somehow increasing the diffusivity of the $\text{CO}_{2,(\text{aq})}$ would improve its supply.

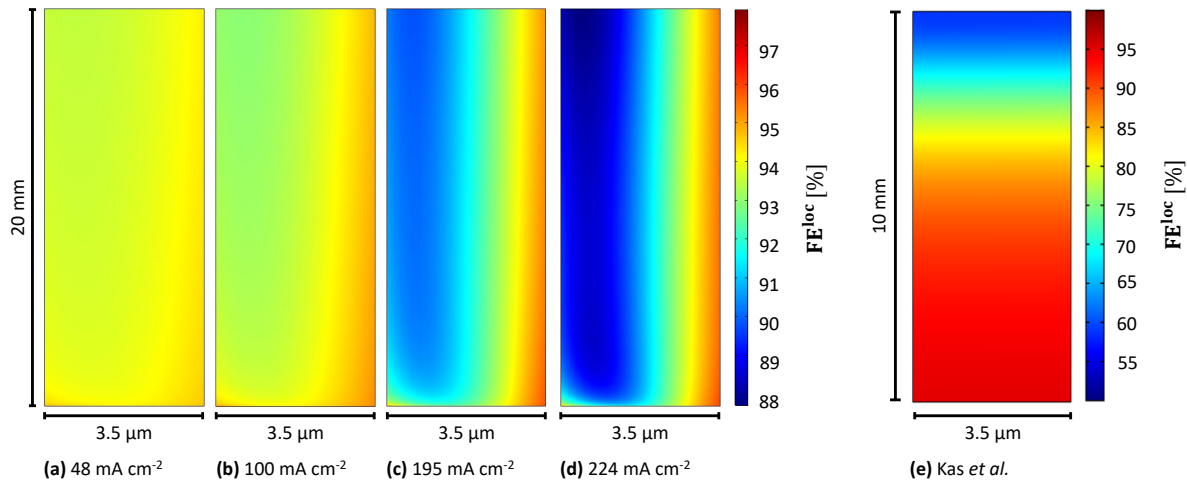
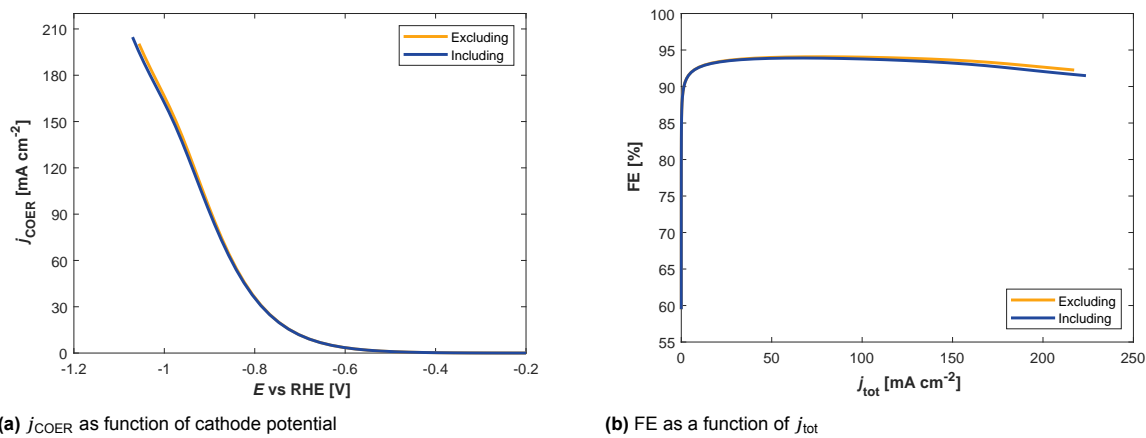


Figure 4.9: (a) to (d) show FE^{loc} inside the CL at different magnitudes of j_{tot} . (e) shows the FE^{loc} as obtained by Kas *et al.*⁶ at $j_{COER} = 750 \text{ mA cm}^{-2}$. Using this figure we can identify the origin of the decreasing FE

4.2.3. Local salting-out effect

The developed model includes local variations in CO_2 solubility which were captured by the Schumpe relation described in the subsection 3.2.2. At higher currents, the ion concentration inside the CL should greatly increase as follows from the stoichiometry of COER and HER (one electron produces one OH^- ion). Consequently, we could expect the solubility of CO_2 to substantially decrease. To quantify this effect, two models, one including and one excluding the salting-out effect are compared and their results are presented in **Figure 4.10**.



(a) j_{COER} as function of cathode potential

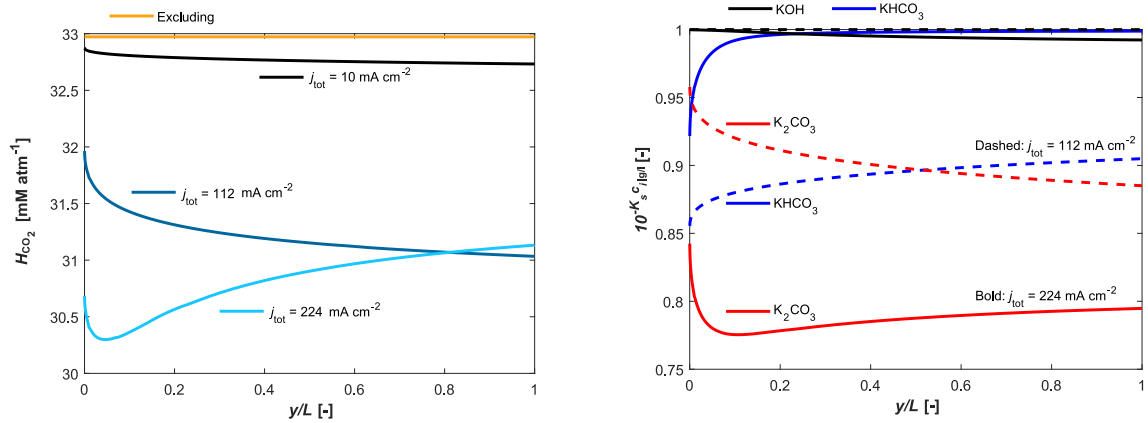
(b) FE as a function of j_{tot}

Figure 4.10: Effect of the salting-out on j_{COER} and FE. Model parameters correspond to the Level 2 model (section 3.5). Excluding refers to a model excluding the salting-out effect, i.e. H_{CO_2} is expressed from Equation 3.28. Including refers to a model including the salting-out effect, i.e. H_{CO_2} is expressed from Equation 3.36.

Including the salting-out effect has a minimal effect on the j_{COER} and FE (**Figure 4.10**). To examine in more detail how the CO_2 solubility changes, **Figure 4.11a** shows how the H_{CO_2} changes along the electrolyser length at various levels of j_{tot} .

Generally H_{CO_2} decreases with increasing j_{tot} (**Figure 4.11a**). However, this is not the case for all examined j_{tot} . At $j_{tot} = 224 \text{ mA cm}^{-2}$, the H_{CO_2} is firstly reduced in the inlet region ($y/L = 0$ to 0.1), but farther down the channel H_{CO_2} starts to increase.

We can explain this behaviour by observing how each individual salt affects the H_{CO_2} (**Figure 4.11b**). In **Figure 4.11b**, according to Equation 3.36, the y -axis represent how much the H_{CO_2} is reduced. That is, $10^{-K_s c_i}$ directly multiplies the uncorrected Henry's constant. If $10^{-K_s c_i}$ were equal to 0.5, this would translate to H_{CO_2} being by 50% lower than its original value calculated from Van 't Hoff equation.



(a) Value of H_{CO_2} when excluding and including the salting-out effect. When included, \bar{H}_{CO_2} is plotted at various j_{tot} . (b) Effect of the 3 different salts on the reduction H_{CO_2} . Dashed lines: $j_{tot} = 112 \text{ mA cm}^{-2}$, bold lines: $j_{tot} = 224 \text{ mA cm}^{-2}$

Figure 4.11: Influence of the salting-out effect on the value of Henry's constant, H_{CO_2} , when plotted as a function of electrolyser length, where $L = 2 \text{ cm}$. (a) shows how the value of H_{CO_2} changes at various magnitudes of j_{tot} in comparison to the fixed value of H_{CO_2} . (b) reveals which salt contributes to the reduction of H_{CO_2} the most and how this changes when going from $j_{tot} = 112 \text{ mA cm}^{-2}$, dashed lines, to $j_{tot} = 224 \text{ mA cm}^{-2}$, bold lines. Contribution of each salt is plotted using the individual terms from the Equation 3.36.

First, we focus on contribution of each salt at $j_{tot} = 112 \text{ mA cm}^{-2}$. $KHCO_3$ reduces the H_{CO_2} the most in the region from $y/L = 0$ to $y/L = 0.5$. However, this effect is diminishing closer to the $y/L = 1$. This follows from the HCO_3^- ions being consumed in R2 and also from the decreasing flux of HCO_3^- ions into the CL (**Figure 4.6b**). On the other hand, CO_3^{2-} ions are produced in the R2 and thus their contribution to the reduction in H_{CO_2} is increasing. However, the effect in H_{CO_2} reduction depends not only on the concentration but also on the Sechenov constant, K_s . Since the $K_{K_2CO_3}$ is nearly two times higher than the K_{KHCO_3} (**Table 3.3**), the H_{CO_2} will suffer from higher reduction in the presence of CO_3^{2-} ions. Consequently, as the CL shifts from the $KHCO_3$ dominated to the K_2CO_3 dominated, the H_{CO_2} will decrease. c_{OH^-} ions itself is still insignificant to be responsible for a change in H_{CO_2} .

Second, we focus on contribution of each salt at $j_{tot} = 224 \text{ mA cm}^{-2}$. Reduction in H_{CO_2} originating from the $KHCO_3$ readily disappears, because most of the HCO_3^- ions are immediately consumed in the R2 (**Figure 4.6d**). The reduction in H_{CO_2} is now fully substituted by K_2CO_3 . However, also the reduction in H_{CO_2} originating from the K_2CO_3 is slowly decreasing towards the outlet. This is because the rate of R2 strongly diminishes towards the outlet (**Figure 4.6d**). Consequently, the production of CO_3^{2-} and also the $c_{CO_3^{2-}}$ decreases towards the outlet (**Figure D.3**). Now, the role of the KOH is more relevant. c_{OH^-} is increasing towards the outlet (**Figure 4.7a**) which follows from the reduction in R2 and ongoing electrochemical reactions. However, the K_{KOH} is the lowest from these 3 salts. Therefore the reduction in H_{CO_2} originating from OH^- ions is not as relevant. All this results in H_{CO_2} increasing towards the outlet.

There is one more effect causing the H_{CO_2} to increase at $j_{tot} = 224 \text{ mA cm}^{-2}$. It is the current density distribution. Production of OH^- ions originating from both the COER and the HER decreases towards the outlet (**Figure D.4a**). This is due to increasing pH and decreasing $c_{CO_2, (aq)}$. As a result, the sum of $c_{HCO_3^-}$, $c_{CO_3^{2-}}$, and c_{OH^-} decreases towards the outlet (**Figure D.4b**) as these ions are transported by both migration and diffusion out of the CL. This shows that total concentration decreases towards the outlet. Subsequently, this decrease in total concentration means that the salting-out effect is getting weaker and thus the H_{CO_2} starts to increase.

To conclude, the changing concentration inside the CL and the increasing current density are found to have minimal effect on the local reduction in the CO_2 solubility. Contrary to the expectation, the solubility of CO_2 does not always show a downward trend, but can also improve.

4.3. Parametric study

In the following subsections we show how different parameters influence electrolyser functionality and we try to provide explanation for the observed phenomena. We aim to generate more understanding and hope to reveal whether any of the considered parameters could improve the electrolyser performance.

4.3.1. Liquid flow rate

To investigate how j_{COER} and FE will change, we model three different flow rates, corresponding to Re of 10, 100, and 200. The results are given in the **Figure 4.12**.

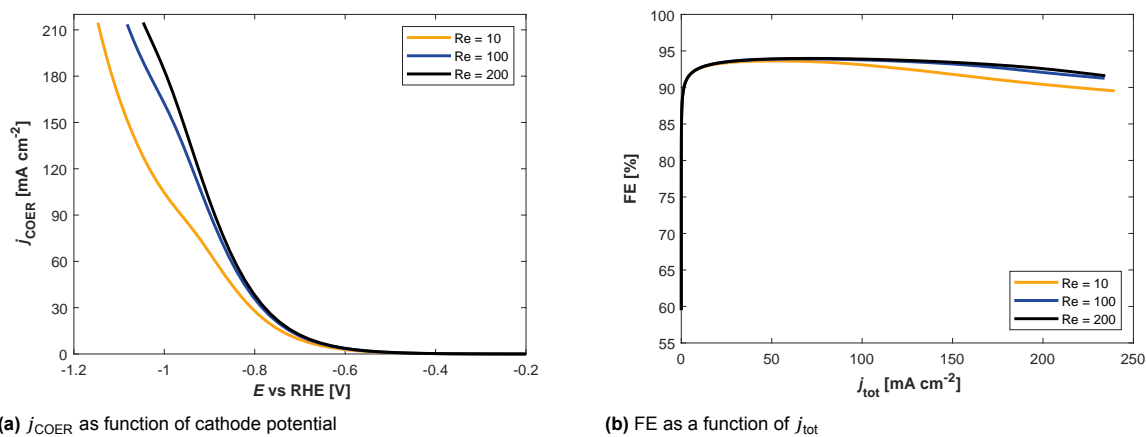


Figure 4.12: Effect of the liquid flow rate. Model parameters correspond to the Level 2 model (section 3.5). The only parameter varied is the Reynolds number, Re.

Electrolyser performance improves in both j_{COER} and FE with increasing liquid flow rate (**Figure 4.12**). We can explain this improvement by firstly investigating the efficiency of the HCO_3^- supply. With increasing liquid flow rate, the flux of HCO_3^- into the CL increases (**Figure 4.14**) which then boosts the R2 reaction rate inside the CL and reduces the increase of the pH. Thus, at the same current density, the pH inside the CL is substantially lower at a higher liquid flow rate (**Figure D.5**).

The value of pH in return influences the electrode potential. According to Equation 4.1, if the pH is higher, a more negative potential is required to reach the same current density. This can thus explain the difference observed in **Figure 4.12a**.

The local pH in the CL also influences the amount of $\text{CO}_{2,(aq)}$ consumed in R1. The higher the pH, the more $\text{CO}_{2,(aq)}$ is consumed (**Figure 4.13**). Lowering the available amount of $\text{CO}_{2,(aq)}$ then favours HER and thus reduces the FE which explains the difference observed in **Figure 4.12b**.

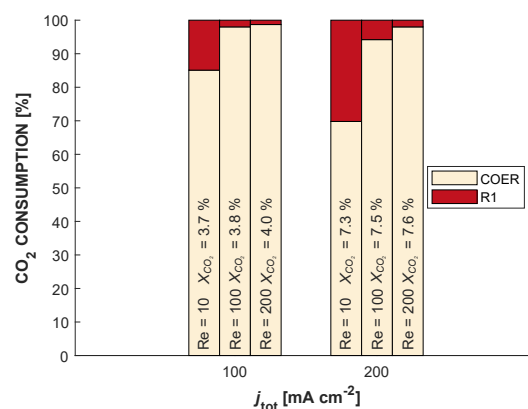


Figure 4.13: Share of CO_2 consumption at different Re and the achieved CO_2 conversion, X_{CO_2} . The higher liquid flow rate enhances the $\text{CO}_{2,(aq)}$ utilisation and slightly improves the X_{CO_2} .

Utilising dimensionless numbers provides another way to quantify the effectiveness of the HCO_3^- supply. Here, we can use two dimensionless numbers: The Peclet number, Pe , and the Sherwood number, Sh . Pe expresses the importance of advection relative to diffusion. Equation 4.3 provides the Pe for the HCO_3^- ions. Sh expresses the magnitude of a molar flux at a boundary relative to the characteristic diffusion. Equation 4.4 provides the Sh for the HCO_3^- ions.

$$Pe_{\text{HCO}_3^-} = \frac{\bar{u}L}{\mathcal{D}_{\text{HCO}_3^-}} \quad (4.3)$$

$$Sh_{\text{HCO}_3^-} = \frac{\mathbf{n} \cdot \mathbf{N}_{\text{HCO}_3^-}}{\mathcal{D}_{\text{HCO}_3^-} (c_{\text{HCO}_3^-}^{\text{initial}} - c_{\text{HCO}_3^-}^{\text{electrolyte/CL}}) / W} \quad (4.4)$$

First, we can calculate the $Pe_{\text{HCO}_3^-}$ for each liquid flow rate (**Figure 4.14**). With increasing $Pe_{\text{HCO}_3^-}$, the convection plays a more significant role and thus the HCO_3^- are replenished in the vicinity of the CL faster. We thus get a thinner boundary layer for the HCO_3^- ions at a higher $Pe_{\text{HCO}_3^-}$.

Second, we can use the definition of $Sh_{\text{HCO}_3^-}$ and evaluate it for each liquid flow rate. **Figure 4.14d** shows the $Sh_{\text{HCO}_3^-}$ when plotted as a function of the electrolyser length. We see that the highest liquid flow rate results in the highest $Sh_{\text{HCO}_3^-}$. This is in line with Lin *et al.*⁵⁴ who report that Sh depends on the $Pe^{1/3}$ even in the presence of a strong bulk reaction. This also verifies that increasing liquid flow rate improves the flux of HCO_3^- ions into the CL.

Using the definition of $Sh_{\text{HCO}_3^-}$ (Equation 4.4), it follows that $Sh_{\text{HCO}_3^-}$ should always be larger than one. However, the $Sh_{\text{HCO}_3^-}$ drops almost to zero for the case where $Re = 10$. This follows from the OH^- ions escaping the CL and reacting away the HCO_3^- ions. Thereafter, the depleted boundary layer forms which makes the HCO_3^- characteristic diffusion (denominator in Equation 4.4) larger than the real flux of the HCO_3^- ions into the CL (nominator in Equation 4.4). The depleted boundary layer at $Re = 10$ (**Figure 4.14a**) should correspond more to the depletion due to reaction than to the depletion due to outflow of the ions. We thus also show that under the certain conditions Equation 4.4 is not applicable to the CO_2 electrolyser. This is because the HCO_3^- boundary layer is not created by diffusion only but the homogeneous reactions too.

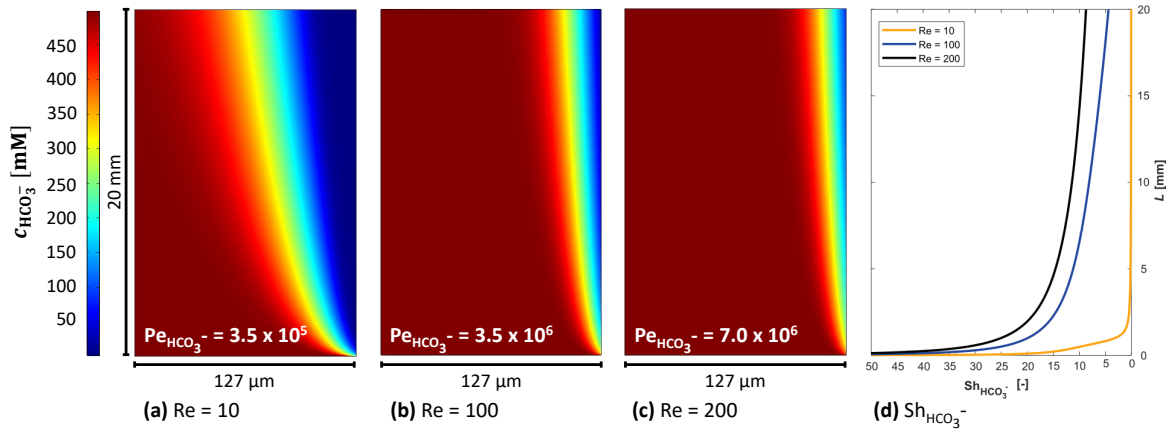
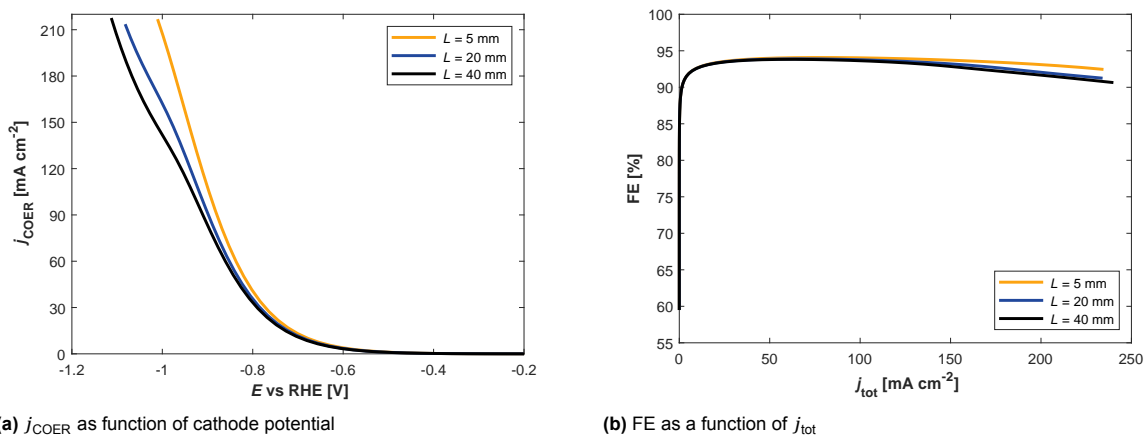


Figure 4.14: (a) to (c) show the distribution of $c_{\text{HCO}_3^-}$ in the electrolyte channel adjacent to the CL on the right. With increasing $Pe_{\text{HCO}_3^-}$, the thickness of the depleted HCO_3^- boundary layer decreases. (d) shows the local $Sh_{\text{HCO}_3^-}$ as a function of the electrolyser length. Decreasing thickness of the boundary layer improves the $Sh_{\text{HCO}_3^-}$ and thus the flux of HCO_3^- ions into the CL. All the results are reported at $j_{\text{tot}} = 200 \text{ mA cm}^{-2}$.

4.3.2. Electrolyser length

The boundary layers extend in the direction of the electrolyte flow and can impede the electrolyser performance. This section now investigates to what extent and how the increasing length of the electrolyser changes its performance.



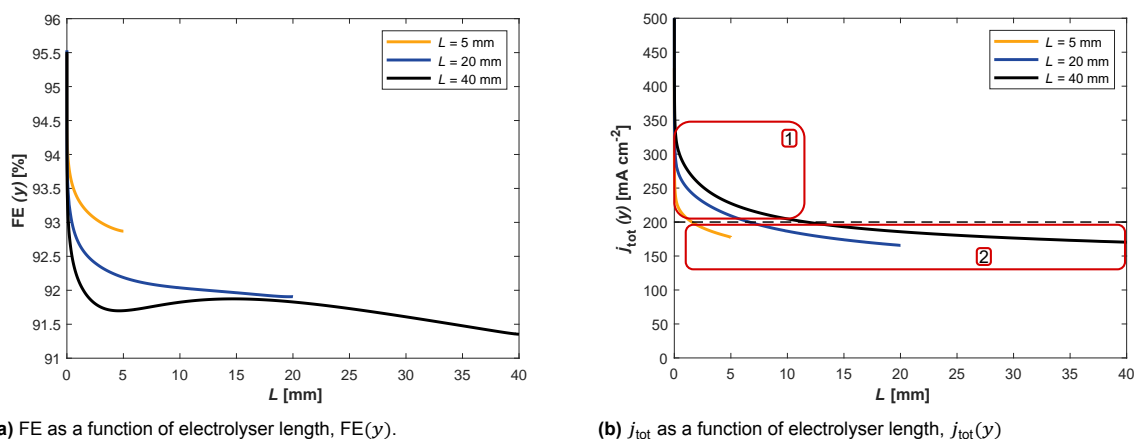
(a) j_{COER} as function of cathode potential

(b) FE as a function of j_{tot}

Figure 4.15: Effect of the electrolyser length. Model parameters correspond to the Level 2 model (section 3.5). The only parameter changing is the electrolyser length, L .

Both j_{COER} and FE decrease with increasing L and this effect is even more pronounced at higher currents (**Figure 4.15**). We can judge the electrolyser performance by investigating the thickness of the HCO_3^- depleted boundary layer (**Figure D.6**). For the given j_{tot} , the boundary layer thickness evolves approximately the same, however, the thickness at the end of the electrolyser is different. The thickness reaches around 30 μm for an electrolyser of 5 mm length, but around 70 μm for an electrolyser of 40 mm length. This leads to a higher pH inside the CL around the outlet region (**Figure D.8a**). The higher pH in the longer electrolyser then leads to a higher $\text{CO}_{2(\text{aq})}$ consumption in R1 (**Figure D.7**). Both these effects decrease j_{COER} and FE and thus explain the **Figure 4.15**.

Another reason for the loss of performance is changing distribution of FE. Plotting a faradaic efficiency as a function of the electrolyser length, $\text{FE}(y)$, reveals that $\text{FE}(y)$ worsens already around the inlet (**Figure 4.16a**).



(a) FE as a function of electrolyser length, $\text{FE}(y)$.

(b) j_{tot} as a function of electrolyser length, $j_{\text{tot}}(y)$

Figure 4.16: (a) faradaic efficiency and (b) total current density as a function of the electrolyser length, $\text{FE}(y)$ and $j_{\text{tot}}(y)$, respectively, (section 3.4). All results are provided at $j_{\text{tot}} = 200 \text{ mA cm}^{-2}$. (a) shows that the longer electrolyser will suffer from lower $\text{FE}(y)$ already around the inlet. (b) reveals that $j_{\text{tot}}(y)$ significantly increases in the inlet region of a longer electrolyser.

To understand why this happens, we need to consider the distribution of current density. Total current density as a function of electrolyser length, $j_{\text{tot}}(y)$, is given in **Figure 4.16b**. The dashed line in **Figure 4.16b** highlights the desired current density and divides thus the length of the CL into two regions. First, a region where $j_{\text{tot}}(y)$ is above the required j_{tot} , second, a region where $j_{\text{tot}}(y)$ is below the required j_{tot} .

To reach the required j_{tot} , $j_{\text{tot}}(y)$ in the region 2 cannot be simply increased since the supply of HCO_3^- ions is lower and pH has inevitably increased. Further, the amount of available $\text{CO}_{2,\text{(aq)}}$ is lower. To meet the required j_{tot} , increasing the applied potential boosts the $j_{\text{tot}}(y)$ in the region 1 where the conditions for COER are more favourable. From **Figure 4.16b** also follows that longer the electrolyser, the more $j_{\text{tot}}(y)$ needs to increase in the region 1.

The more $j_{\text{tot}}(y)$ is increased in the region 1, the higher the production of OH^- . This locally increased OH^- production, however, increases the pH (**Figure D.8a**) and the rate of R1 (**Figure D.8b**). These two negative effects finally cause the $\text{FE}(y)$ to decrease already around the inlet region. Further downstream the $\text{FE}(y)$ decreases due to diminishing buffering strength. Consequently, making the electrolyser longer decreases the $\text{FE}(y)$ not only in the extra added length but throughout the whole CL (**Figure 4.16a**).

4.3.3. Operating pressure

The amount of dissolved CO_2 in the electrolyte and the maximum flux across the gas/liquid interface depend on the operating pressure. Thus, increasing the operating pressure allows feeding significantly more CO_2 which could improve the electrolyser performance. This effect is quantified in **Figure 4.17**.

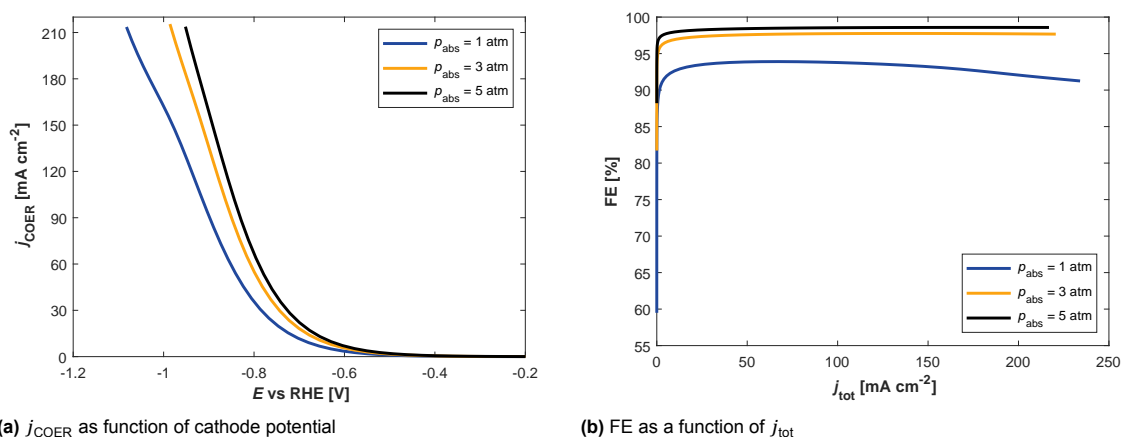


Figure 4.17: Effect of the operating pressure. Model parameters correspond to the Level 2 model (section 3.5). The only parameter changing is the operating absolute pressure, p_{abs} .

Significant improvement in both j_{COER} and FE can be obtained if the electrolyser was operated at higher pressures (**Figure 4.17**). The reason for improved performance can be broken down into two factors. First, and most importantly, the increased supply of the gaseous and liquid CO_2 now efficiently feeds also the side of CL facing the electrolyte. Thus, $j_{\text{COER}}^{\text{loc}}$ distribution substantially improves (**Figure 4.18**). We should also notice that the $j_{\text{COER}}^{\text{loc}}$ distribution now more resembles the pH profile inside the CL (**Figure 4.19**). This similarity probably arises from the electrolyser now being controlled by the pH only rather than by the combined effect of pH and supply of $c_{\text{CO}_{2,\text{(aq)}}$.

The enhanced supply of CO_2 and $\text{CO}_{2,\text{(aq)}}$ also translates to the improvement in FE^{loc} . The drop in FE^{loc} occurring near the electrolyte/CL boundary when operating at 1 atm (**Figure 4.9**) is now completely compensated and the variations in FE^{loc} do not exceed 1% at the two higher operating pressures.

Unfortunately, the current model cannot distinguish between the gaseous or liquid origin of $\text{CO}_{2,\text{(aq)}}$ that reacted in the COER. This means that it cannot be explicitly determined whether it is predominantly $\text{CO}_{2,\text{(aq)}}$ or gaseous CO_2 increasing the activity near the electrolyte/CL boundary.

The second reason why the required E to drive the j_{COER} decreases could be ascribed to the buffering effect of $\text{CO}_{2,\text{(aq)}}$. Each $\text{CO}_{2,\text{(aq)}}$ can neutralize two OH^- ions as follows from the stoichiometry of R1 and R2. Consequently, the pH inside the CL is buffered more efficiently (**Figure 4.19**). However, this

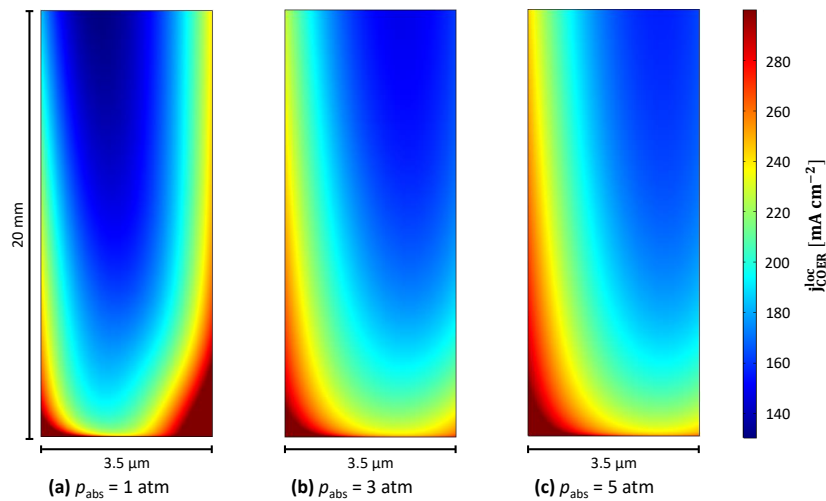


Figure 4.18: Distribution of $j_{\text{COER}}^{\text{loc}}$ inside the CL at various operating pressures p_{abs} . Results are at $j_{\text{tot}} = 200 \text{ mA cm}^{-2}$. The figure shows how the distribution of $j_{\text{COER}}^{\text{loc}}$ improves and shows a similarity to the pH distribution (**Figure 4.19**).

leads to an increased consumption of $\text{CO}_{2,(\text{aq})}$ in the R1 (**Figure D.9**). Supply of $\text{CO}_{2,(\text{aq})}$ is nevertheless still sufficient to compensate for that.

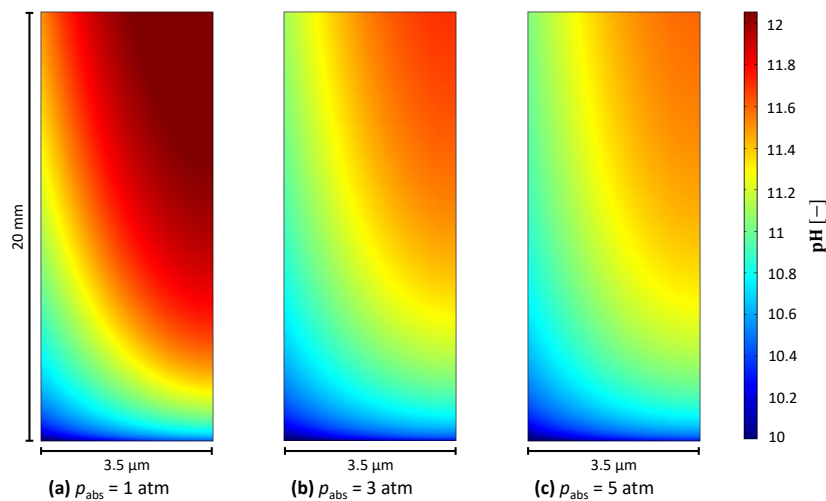


Figure 4.19: pH distribution inside the CL at various operating pressures p_{abs} . Results are at $j_{\text{tot}} = 200 \text{ mA cm}^{-2}$. The amount of produced OH^- is in each case the same. The decrease in pH in (b) and (c) relatively to (a) can be solely attributed to the buffering effect of $\text{CO}_{2,(\text{aq})}$.

To conclude, operating a CO_2 electrolyser at pressures higher than ambient can significantly boost both j_{COER} and FE not only due to high supply of CO_2 but also due to its buffering effect. The drawback of operating at higher pressures follows from the necessity to pressurize the fluid feeds. To determine the most economically efficient operating pressure, the cost of pressurizing the fluids should be weighted against the improved performance.

4.4. CO₂ electrolyser with 1 m length

To make the CO₂ electrolyser a successful technology, it is required to reach higher production rates. To achieve this goal, electrolysers need to be scaled up while still maintaining a high current density and FE. However, the variations along the flow direction may pose a challenge to this task. This gives a rise to the question of how significantly the performance of a small-scale electrolyser changes when moving to a large-scale.

However, the performance of the industrially sized electrolyser has not yet been evaluated experimentally, at least to the best of our knowledge. All the detailed numerical models considered length scales of only tens of mm. We thus identify a gap in the research.

To answer these questions, we present a model of an electrolyser that approaches the industrial scale. The length of such electrolyser is set to 1 m and will be referred to as long electrolyser. We also compare the performance of this electrolyser to its laboratory counterpart. The length of the laboratory electrolyser is set to 4 cm and will be referred to as short electrolyser.

The following sections first discuss the observed performance, then, the final section provides an explanation for the observed phenomena.

4.4.1. Overall performance

A successful CO₂ electrolyser needs to perform well in current density, j_{tot} , faradaic efficiency, FE, and single pass conversion, X_{CO_2} . **Figure 4.20** summarizes all the important metrics and compares the long and short electrolysers.

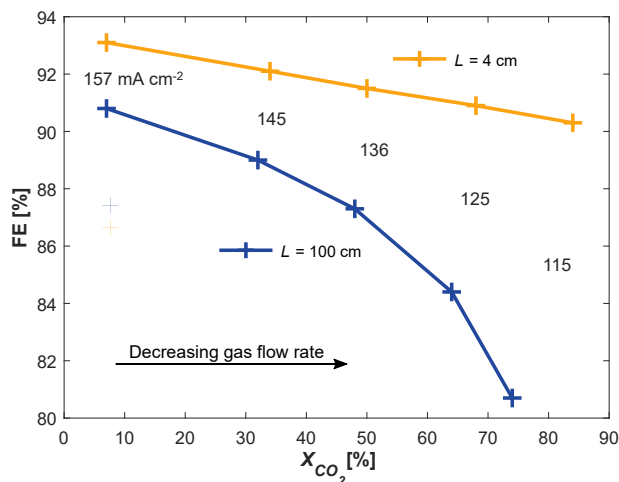


Figure 4.20: Faradaic efficiency, FE, as a function of a single pass conversion, X_{CO_2} , at various total current densities, j_{tot} . The blue line represents the long electrolyser with a length, L , of 100 cm. To reach a higher X_{CO_2} , the applied potential was kept constant at 3.10 V but the gas flow rate was decreased. The yellow line represents the short electrolyser with a length, L , of 4 cm. To reach a higher X_{CO_2} the gas flow rate was adjusted accordingly, that is, decreased by the ratio of the lengths (subsection 3.2.8). To also reach the same j_{tot} , the applied potential was varied from 2.98 V to 2.94 V. Each simulation is marked with a + marker sign and the number in between the blue and the yellow mark corresponds to the obtained j_{tot} . The observed X_{CO_2} reaches values significantly higher than the limit drawn by Kas *et al.*⁶ This is explained in subsection D.3.1. This figure summarizes all the important metrics characterizing the electrolyser performance and compares electrolyser with a 4 cm and 100 cm length.

A major difference between the long and short electrolyser follows from the trend in the FE vs. X_{CO_2} plot (**Figure 4.20**). While the short electrolyser exhibits a linear decrease in FE with increasing X_{CO_2} , the long electrolyser shows a rather logarithmic dependence. If we focus on the point of the highest X_{CO_2} , we find a 10% difference in both FE, and X_{CO_2} when comparing the small to the large-scaled electrolysers. This shows that both FE and X_{CO_2} achieved in the small-scale electrolyser will be significantly different at the large-scale. The FE vs X_{CO_2} trend further shows that it may be very challenging to achieve both high FE and X_{CO_2} at the same time.

Another trade-off that the long electrolyser will have to face is between X_{CO_2} and j_{tot} (**Figure 4.20**). With increasing X_{CO_2} , it is not only the FE that decreases but also j_{tot} . However, this drop j_{tot} is not so significant in the short electrolyser. That is because the applied potential in the short electrolyser had

to be decreased to match the j_{tot} of the long electrolyser. If the applied potential was kept constant, as in the long electrolyser, the short electrolyser could also reach a higher j_{tot} . This would however come at expense of FE (**Figure D.10**).

When operating at low X_{CO_2} , the behaviour of long electrolyser approaches the behaviour the short electrolyser. The difference in conversion is almost negligible and the FE is lower by only 2.3%. However, if the applied potential were the same in both electrolysers, the current density achieved in the short electrolyser would be by roughly 60 mA cm^{-2} higher. We conclude that the small-scale electrolysers can, into a certain extent, reflect their larger counterparts.

Based on these findings, we can draw two general conclusions. First, the performance of the small-scale GDE based electrolysers needs to be greatly improved if these small-scale electrolysers should ever be successfully scaled up. Second, we can infer that the conclusions drawn from a small-scale electrolysers are not well applicable to the large-scale electrolyser, at least at high X_{CO_2} . This especially applies to the numerical models which transfer their findings to the long scale.

To understand where the differences in the performance are coming from, we can evaluate j_{tot} and FE locally. We will thus focus only on two models in the next sections. We choose to compare the cases with the highest X_{CO_2} . This is because the macroscopic differences (FE, j_{tot}) between the two length scales are the highest, so the microscopic differences (local FE, j_{tot}) should be the most apparent. Also because in terms of gas separation, this highest X_{CO_2} would be favoured. The two discussed models thus correspond to the right most data points in the **Figure 4.20**.

4.4.2. Performance within the catalyst layer

To reveal how the performance inside the electrolyser changes, we can visualize the faradaic efficiency as a function of the electrolyser length, $\text{FE}(y)$, (**Figure 4.21**). To complete the picture, we also plot the total current density as a function of the electrolyser length, $j_{\text{tot}}(y)$, (**Figure 4.22**).

Faradaic efficiency as a function of the electrolyser length

The short electrolyser shows a seemingly sharp decrease in $\text{FE}(y)$ over its whole 4 cm length (**Figure 4.21**).

We attribute this drop in $\text{FE}(y)$ to the decreasing p_{CO_2} (**Figure 4.25**). The lower p_{CO_2} then results in a lower flux of CO₂ across the gas/liquid interface and into the CL. This lower flux of CO₂ means that the amount of available CO_{2(aq)} will be lower which thereafter decreases the j_{COER} and thus the FE. On the other hand, the long electrolyser has the decreasing p_{CO_2} distributed over the whole 100 cm length. Thus, the first 4 cm experience a relatively higher p_{CO_2} , and are better supplied by the gaseous CO₂.

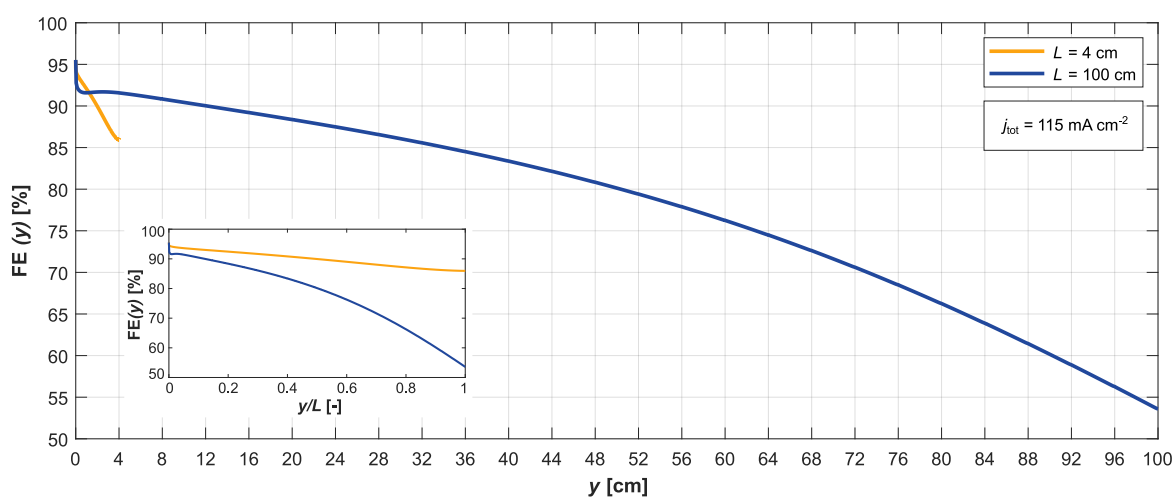


Figure 4.21: FE as function of the electrolyser length, $\text{FE}(y)$. The embedded figure plots the $\text{FE}(y)$ as a function of normalized length of the electrolyser. The figure shows the long electrolyser, $L = 100 \text{ cm}$, and the short electrolyser, $L = 4 \text{ cm}$. Both results correspond to $j_{\text{tot}} = 115 \text{ mA cm}^{-2}$. The figure here reveals that the long electrolyser retains high performance only for the first few centimeters.

The $\text{FE}(y)$ distribution shows substantial difference between the two electrolysers (**Figure 4.21**). First, the $\text{FE}(y)$ in the short electrolyser keeps above 90% for about a half of its length. Compare that to

the long electrolyser which maintains $FE(y)$ over 90% for only the first 12 cm. Second, we focus on the outlet region. The shorter electrolyser ends with the $FE(y)$ being over 85%, while the $FE(y)$ drops to almost 50% in the long electrolyser. In other words, the outlet region of the long electrolyser is responsible for the production of almost 1:1 CO:H₂ gas mixture. To conclude, $FE(y)$ in the long electrolyser is for most of its length, around 70 cm, below the minimum $FE(y)$ observed in the short electrolyser.

Using the normalized figure, we can conclude that it is the whole CL which is responsible for the higher drop in FE (**Figure 4.20**). However, it is predominantly the regions outside the inlet contributing the most.

Total current density as a function of the electrolyser length

The **Figure 4.22** reveals the distribution of current density over the CL. First, we focus on the first 4 cm. The long electrolyser shows average $j_{tot}(y)$ slightly over 200 mA cm⁻² across this length. In case of the short electrolyser, the first 4 cm correspond to its whole length and the average $j_{tot}(y)$ over this length is only 115 mA cm⁻². Such a high difference in the $j_{tot}(y)$ may lead to a worse performance (**Figure 4.16**).

Second, we focus on the outlet regions. $j_{tot}(y)$ drops to only slightly a slightly lower value in the long electrolyser in comparison to the short electrolyser. The $j_{tot}(y)$ is thus not showing a great deterioration in the long electrolyser. However, the difference in $j_{tot}(y)$ between the inlet and outlet regions is significantly higher in the long electrolyser. Such uneven current distribution is undesirable. It also propagates into the GDL. As Kas *et al.* point out, the uneven distribution of current in GDL can cause the electrode to deteriorate faster.

We further show at what length the electrolyser achieves the 50% of its total CO production (**Figure 4.22**). We find that the first 33 cm of the electrolyser are responsible for the half of the CO produced, while it takes another 2/3 of the electrolyser to produce the remaining half of the CO. This distribution is shifted more to the middle in case of the short electrolyser. It takes the first 41% of the total length to produce the half of CO. This again highlights that making the electrolyser longer only moves the production more to the inlet region while the remaining parts are less active.

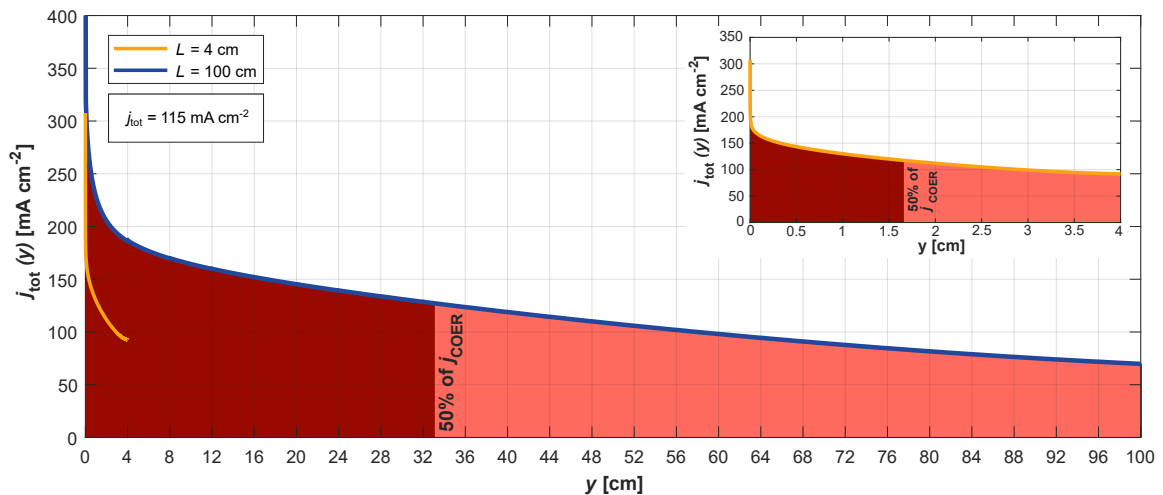


Figure 4.22: j_{tot} as a function of electrolyser length, $j_{tot}(y)$. The figure shows the long electrolyser, $L = 100$ cm, and the short electrolyser, $L = 4$ cm. Both results correspond to $j_{tot} = 115$ mA cm⁻². The dark red area shows the length which is responsible for the first 50% of the j_{COER} . That is here COER consumes the first 50% of the total amount of electrons consumed in COER. The light red area shows the length which is responsible for remaining 50% of the j_{COER} . That is here COER consumes the next half of its total amount of electrons. The embedded figure shows the same but for the short electrolyser.

To conclude, we find that, first, scaling up the electrolyser length results in higher variations in both $FE(y)$ and $j_{tot}(y)$ between the inlet and the outlet. This means that the distribution in a longer electrolyser will be less uniform. Second, the long electrolyser can retain the $FE(y)$ above the minimum observed in the short electrolyser only for the first 30 cm. Third, scaling up the electrolyser length

means shifting the CO production more towards the inlet region. These findings highlight that making the electrolyser longer only moves the performance more to the inlet region while the added regions become less active.

4.4.3. Produced gas mixture

Separation of the gas products plays an important role in the CO₂ electrolyzers. The goal is to maximize the amount of CO and minimize the amount of CO₂ at the outlet. This is partially reflected by the X_{CO_2} . However, it is interesting to visualize the exact composition of the produced gas mixture (**Figure 4.23a**).

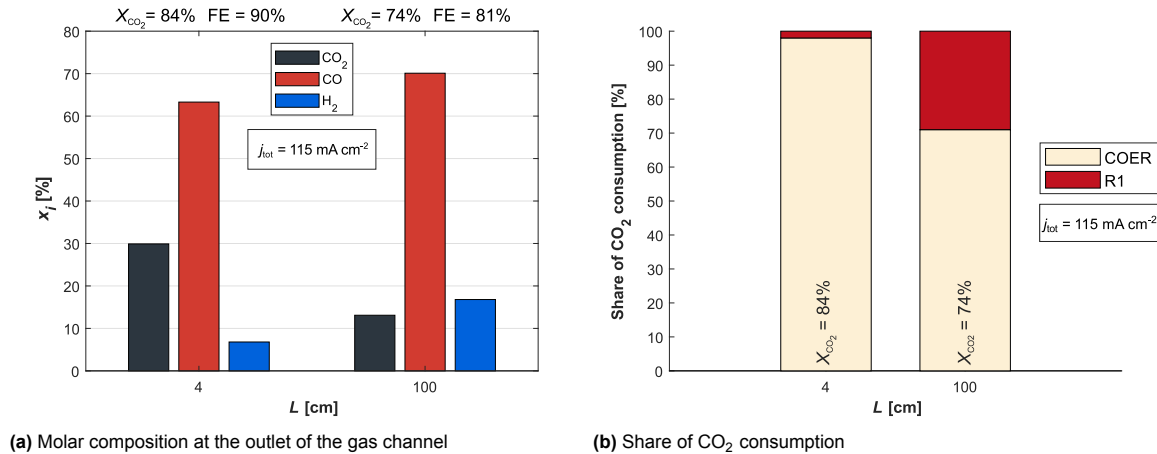


Figure 4.23: The figure shows the long electrolyser, $L = 100 \text{ cm}$, and the short electrolyser, $L = 4 \text{ cm}$. Both results correspond to $j_{\text{tot}} = 115 \text{ mA cm}^{-2}$.

Although the short electrolyser shows more favourable FE and X_{CO_2} , the gas mixture produced in the long electrolyser seems more favourable in terms of separation (**Figure 4.23a**). The CO molar fraction, x_{CO} , is about 5% higher and the CO₂ molar fraction, x_{CO_2} , is about 15% lower in the long electrolyser. This may seem in contradiction with the reported FE and X_{CO_2} . However, we can explain this as follows. First, the amount of CO₂ consumed in the R1 is substantially greater in the long electrolyser (**Figure 4.23b**). This increased consumption then decreases the absolute amount of CO₂ at the outlet of the gas channel. As a result this causes the fraction of CO to be relatively higher. This happens although the FE is lower. The fraction of H₂ at the outlet of the long electrolyser is also greater, which follows from the earlier argument and from the lower FE.

To conclude, the separation of the gaseous mixture produced in the longer electrolyser may be more favourable as the fraction of CO at the outlet is higher. However, more CO₂ is lost to the electrolyte. The regeneration of the electrolyte should thus also be considered. This means that we cannot unambiguously claim that a longer the electrolyser will favor a cheaper separation overall.

4.4.4. Understanding the reduction in performance

To understand why $j_{\text{tot}}(y)$ is substantially higher in the inlet region, and why $\text{FE}(y)$ falls to substantially lower values in the long electrolyser, we should understand what happens in the vicinity of the CL. Here we divide the analysis into two sections. First, we focus on what is happening outside of the CL. Second, we focus on the inside of the CL, we use the previous knowledge, and explain the final pH distribution. Finally, we briefly explain the observed changes in the performance.

Flux of HCO_3^- and OH^- and partial pressure of CO₂ at the boundaries of the CL

Flux of HCO_3^- dominates in the short electrolyser while flux of OH^- dominates in the long

The consumption of HCO_3^- and production of OH^- inside the CL leads to the flux of these species taking a certain distribution along the electrolyte/CL interface. As more HCO_3^- gets consumed inside the CL, the concentration gradient between the CL and the bulk of the electrolyte increases. As this gradient increases, the diffusional flux of HCO_3^- into the CL increases and more HCO_3^- ions enter the CL. The OH^- flux follows the analogous reasoning but its concentration is higher inside the CL. Therefore, diffusional flux will force OH^- out of the CL.

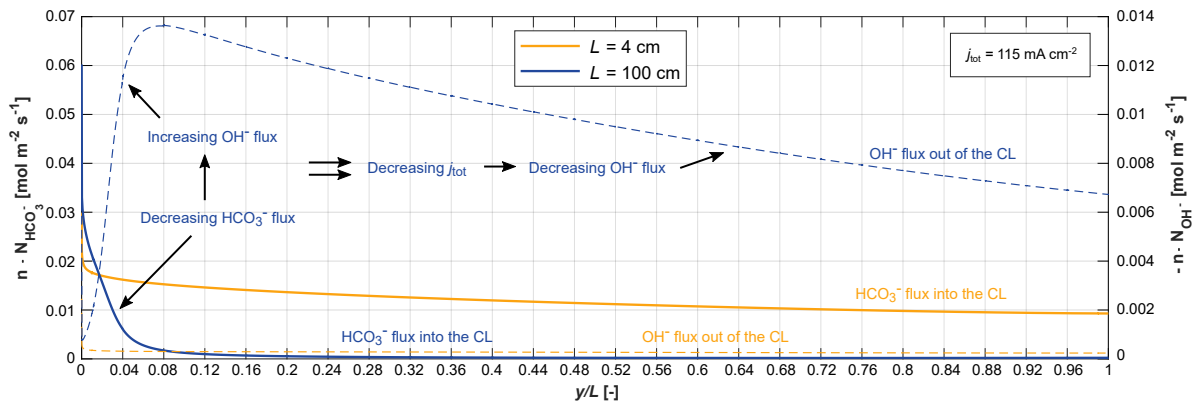


Figure 4.24: Bold lines: molar flux of HCO_3^- ions into the CL, $\mathbf{n} \cdot \mathbf{N}_{\text{HCO}_3^-}$. Dashed lines: molar flux of OH^- ions out of the CL, $-\mathbf{n} \cdot \mathbf{N}_{\text{OH}^-}$. Both fluxes are evaluated at the electrolyte/CL boundary. The flux of OH^- has a positive value due to the way y -axis is defined. The figure shows the long electrolyser, $L = 100$ cm, and the short electrolyser, $L = 4$ cm. Both results correspond to $j_{\text{tot}} = 115 \text{ mA cm}^{-2}$. Both fluxes are for a better visualization plotted against the normalized length of the electrolyser.

Although both electrolyzers operate at the same j_{tot} , they both show very different distribution of the HCO_3^- and OH^- flux. The short electrolyser shows the flux of HCO_3^- ions into the CL only slightly decreasing throughout its whole length. This can be attributed to a lower thickness of the depleted boundary layer of HCO_3^- ions. In the shorter channel, this boundary layer does not evolve to as large thickness as in the longer channel. This then allows maintaining the flux of HCO_3^- ions across the whole electrolyser length. As these HCO_3^- ions enter the CL, the OH^- ions are consumed inside the CL. This causes only a minimal amount of OH^- ions to leave the CL.

In the case of the long electrolyser, we can distinguish two specific regions. First, we deal with a region from $y/L = 0$ to roughly $y/L = 0.04$. The flux of HCO_3^- just near the inlet is maximal and quickly decreases. The flux of OH^- ions out of the CL then starts to increase substantially. This is a direct consequence of the locally increased $j_{\text{tot}}(y)$ which for this region is slightly over 200 mA cm^{-2} (**Figure 4.22**). Such high $j_{\text{tot}}(y)$ generates substantial amount of OH^- ions which consume significant amount of HCO_3^- in the R2 homogeneous reaction. This results into a strong flux of HCO_3^- ions into the CL. However, this flux quickly decreases due to two reasons. First, the diffusional path for HCO_3^- has greatly increased. Second, OH^- ions leaving the CL consume the HCO_3^- before they can reach the CL. The OH^- flux out of the CL can then increase further and finally prevails over the flux of HCO_3^- ions.

Such flux distribution has already been described earlier. For a long electrolyser, phenomena in this region correspond to **Figure 4.6d**. This follows from the average $j_{\text{tot}}(y)$ of 200 mA cm^{-2} . In comparison, the short electrolyser over the region of the same length (4 cm, whole electrolyser length) reaches the average $j_{\text{tot}}(y)$ of 115 mA cm^{-2} . For a short electrolyser, phenomena in this region correspond to **Figure 4.6b**. We thus stress that the flux distribution in both electrolyzers is strikingly different already in the inlet region.

The second distinct region in the long electrolyser is identified from $y/L = 0.04$ to $y/L = 1$. In this region, the flux of HCO_3^- ions into the CL is approaching zero, while the flux of OH^- outside of the CL is dominating. This follows from two reasons: first, the HCO_3^- ions flowing in the CL vicinity were all mostly already consumed in the first region; second, the diffusion path for the HCO_3^- is significantly larger and thus the OH^- ions are now leaving the CL. These OH^- ions are then consuming the HCO_3^- ions in the bulk of the electrolyte channel. We thus show that in the second region, the flux of HCO_3^- ions into the CL is almost non-existent. This means that the electrolyte does not provide any buffering to the CL but acts only as a sink for the OH^- ions.

We can also notice that the flux of OH^- ions is decreasing in the second region. This follows from the $j_{\text{tot}}(y)$ distribution (**Figure 4.22**). As the $j_{\text{tot}}(y)$ decreases towards the outlet, so does the generation of OH^- ions. The lower generation of OH^- ions then inherently cause the flux of these ions outside of the CL to decrease.

Long electrolyser shows a lower CO₂ partial pressure despite the lower single-pass conversion

To better reflect the real function of the electrolyser, we reduced the gas flow rate to maximize the single-pass conversion of our electrolyser. This leads to a substantial variation of CO₂ flux across the gas/liquid interface between the inlet and outlet. Since this flux is proportional to p_{CO_2} , as follows from Equation 3.26, we provide the p_{CO_2} distribution in **Figure 4.25**.

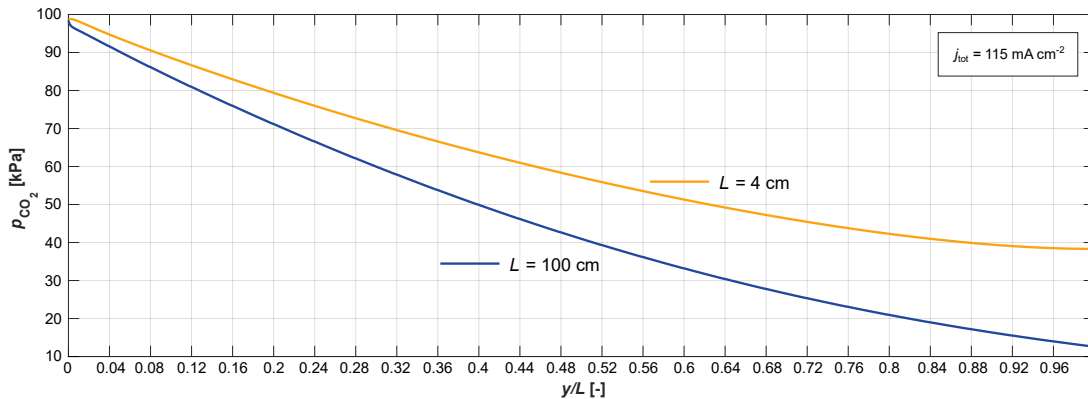


Figure 4.25: CO₂ partial pressure, p_{CO_2} , at the CL/GDL boundary. The figure shows the long electrolyser, $L = 100$ cm, and the short electrolyser, $L = 4$ cm. Both results correspond to $j_{\text{tot}} = 115 \text{ mA cm}^{-2}$. For a better visualization plotted against the normalized length of the electrolyser.

p_{CO_2} is always lower in the long electrolyser and this difference is only increasing. To explain this, we can again use the two region analysis from the above. In the first region, from $y/L = 0$ to roughly $y/L = 0.04$, we could argue that the lower p_{CO_2} originates from the higher $j_{\text{COER}}(y)$ (**Figure D.11**). The higher $j_{\text{COER}}(y)$ requires a higher flux of CO₂ from the gaseous phase and thus lowers the p_{CO_2} . In the second region, i.e. from $y/L = 0.04$ to $y/L = 1$, the 100 cm electrolyser still shows a lower p_{CO_2} although the $j_{\text{COER}}(y)$ is lower in comparison to the short electrolyser (**Figure D.11**). This difference can be explained through the larger consumption of CO₂ in the homogeneous R1 (**Figure 4.23b**). The rate of R1 is higher for the long electrolyser, because the buffering efficiency has been significantly reduced. This creates a sink for the CO_{2,(aq)} and forces additional gaseous CO₂ to enter the CL. As a result, this decreases the p_{CO_2} .

Average pH inside the CL differs by whole 2 units

Here the **Figure 4.26** shows pH distribution inside the both electrolysers.

First, we focus on the short electrolyser (**Figure 4.26a**). Previously we have shown that the flux of HCO₃⁻ ions into the CL is almost uniform throughout the whole length of the CL (**Figure 4.24**). This provides the buffering capacity to the whole CL and the distribution of R2 is uniform (**Figure 4.6b**). This restricts the pH from increasing sharply throughout the whole CL. The strength of the buffering capacity can be also better understood by realising that the j_{tot} is same in both electrolyser.

Second, we focus on the long electrolyser (**Figure 4.26b**) and we again divide the analysis into two regions. First, we focus on the first 4 cm. The extremely high flux of HCO₃⁻ ions into the CL just near the inlet causes the R2 rate to increase dramatically (**Figure 4.24** and **Figure 4.6d**). However, this inflow of HCO₃⁻ quickly decreases and the R2 rate diminishes (**Figure 4.6d**). The pH is thus firstly restricted by the flux of HCO₃⁻ ions but its evolution is less and less restricted in the downstream direction. All this results into the observed pH profile. To remark, this pH distribution is very similar to the one reported earlier in **Figure 4.7a** which corresponded to electrolyser of 2 cm and $j_{\text{tot}} = 224 \text{ mA cm}^{-2}$.

If we now focus on a region from the 4 cm mark until the outlet, we find that the pH is almost constant. In this region, the flux of HCO₃⁻ does not play a role and the only buffering originates from the consumption of CO_{2,(aq)} in R1. However, this effect is rather weak since the net R2 rate is still significantly diminished (**Figure D.12**). Therefore, this region of the CL is very poorly buffered and we could claim that most of the produced OH⁻ ions are also leaving the CL. This means that the pH profile will not further change dramatically.

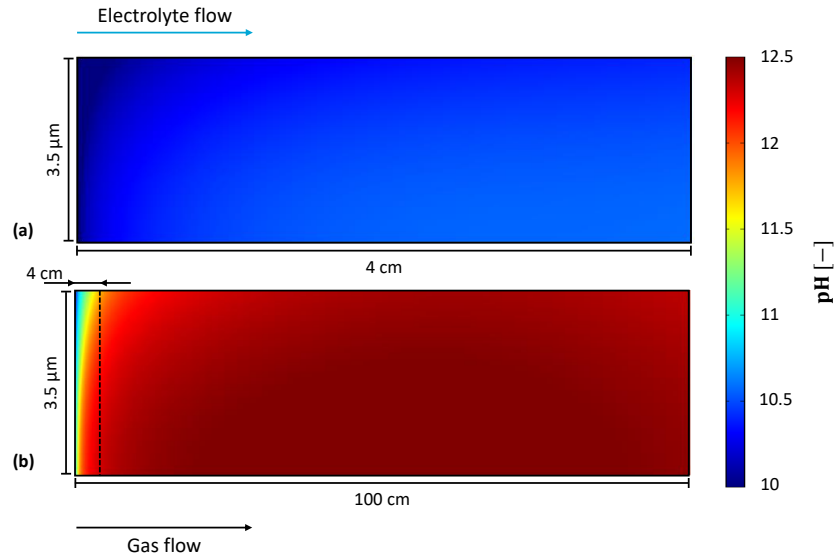


Figure 4.26: pH distribution inside the CL. The figure shows in (a) the long electrolyser, $L = 100$ cm, and in (b) the short electrolyser, $L = 4$ cm. Both results correspond to $j_{\text{tot}} = 115 \text{ mA cm}^{-2}$. Dashed line in (b) highlights the end of the first subcell which length is 4 cm.

Explaining the observed changes in the performance

Finally, we can use the pH distribution (**Figure 4.26b**) to explain the observed performance in the long electrolyser. First, the high pH results in high consumption of $\text{CO}_{2,\text{(aq)}}$ in the R1 (**Figure 4.23b**). Second, the consumption of $\text{CO}_{2,\text{(aq)}}$ in R1 reduces the amount of available $\text{CO}_{2,\text{(aq)}}$ for the COER. This is further enhanced by the decreasing p_{CO_2} (**Figure 4.25**) and thus both result in the decreasing trend in $j_{\text{COER}}(y)$ (**Figure D.11**). With the decreasing $j_{\text{COER}}(y)$, we then get a decreasing trend in $\text{FE}(y)$ (**Figure 4.21**). This is because the HER is not influenced by the reactant supply (Equation 4.2).

The difference in the performance between the short and the long electrolyser can also be attributed to the pH profile. If we follow the implications from the above paragraph, we can say that all these will have a significantly lower effect on the small-scale. This means that the consumption of $\text{CO}_{2,\text{(aq)}}$ will be lower, and both $j_{\text{COER}}(y)$ and FE will be higher. The lower pH also results in a less negative potential required to achieve the same j_{COER} (Equation 4.1). This contributes to the reason why we had to decrease the applied potential to match the j_{tot} (**Figure 4.20**).

4.5. Strategies to improve the performance of long electrolyzers

The following sections present two suggestions on how the GDE electrolyser performance could be enhanced. Firstly, an idea is presented, followed by an overview of the results. A section is concluded with an investigation on the observed trends.

4.5.1. Fluid flow configuration

CO₂ electrolyzers can be operated in a regime with the gaseous and electrolyte stream flowing in the same direction referred to as the co-current configuration. However, the local pH increases in the flow direction, while FE and $j_{tot}(y)$ are decreasing (**Figure 4.7a** and **Figure 4.21** or **Figure 4.22**). The decreasing performance along the flow direction is further affected by the falling p_{CO_2} .

However, operating the electrolyser with gas and electrolyte streams flowing in the opposite direction could mitigate these effects. This regime will be referred to as counter-current. The idea is, that near the electrolyte inlet, p_{CO_2} should be at its minimum, but the electrolyte will provide most of its buffering capacity. Thus, CO_{2,(aq)} should be effectively utilised in COER around the inlet. Near the electrolyte outlet, p_{CO_2} should be at its maximum, but the electrolyte buffer capacity is exhausted. Thus, a high flux of gaseous CO₂ into the CL could compensate for the higher amounts of CO_{2,(aq)} being consumed in R1.

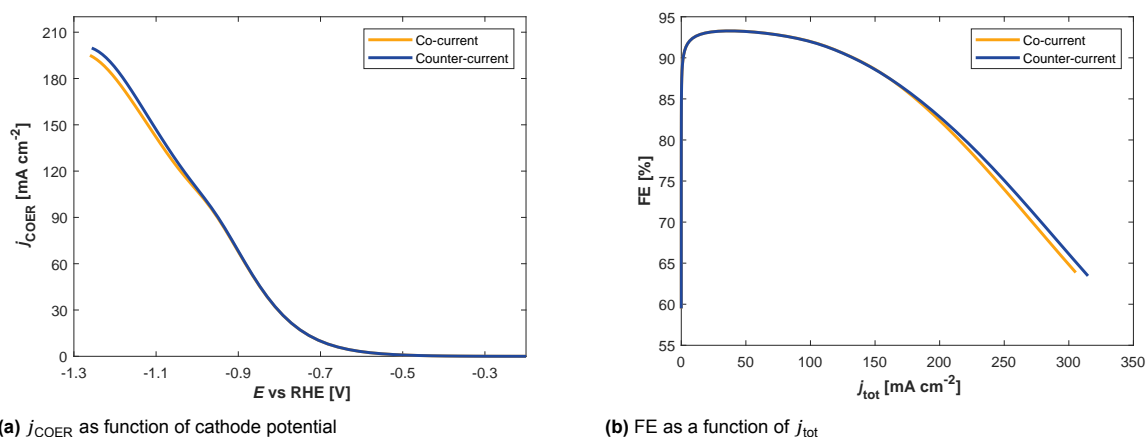


Figure 4.27: Effect of the flow orientation. Co-current refers to the co-current regime, and counter-current refers to the counter-current regime. To reflect a real operation of the electrolyser, its length is set to 10 cm and the assumed CO₂ conversion to 80% (subsection 3.2.8). The remaining model parameters correspond to that of the Level 2 model.

Operating the electrolyser in the counter-current regime has very little influence on its total performance (**Figure 4.27**). To understand why we do not see any significant change in the performance, we should investigate the local variations inside the CL. We can distinguish distinct regions inside the CL which show high activity towards the COER (**Figure 4.28**).

First, we focus on regions 2 and 6. The enhanced activity in these regions can be attributed to the supply of the gaseous CO₂. However, the FE^{loc} decreases in the direction of the gas flow. This can be linked to a decreasing p_{CO_2} , which lowers the flux of CO₂ into the CL in accordance to Equation 3.26.

Regions 1 and 4 show enhanced activity as a result of the electrolyte flow. We ascribe this increase in FE^{loc} to a higher supply of HCO₃⁻ ions, which limit the increase of the pH and boost the j_{COER} in accordance to Equation 4.1. Another benefit of the newly supplied electrolyte is the initially dissolved CO_{2,(aq)}. A new supply of CO_{2,(aq)} increases its concentration in the CL and thus improves the j_{COER} . **Figure D.14** shows these variations in pH and $c_{CO_2,(aq)}$.

If we consider the size of the region 4, we see why the counter-current regime does not lead to any significant improvement in the electrolyser performance. The region 4 does not span far in the downstream direction, but is restricted to only 1 to 2 cm. This tells us that the performance of the CL is driven predominantly by the p_{CO_2} . The fresh electrolyte can only boost the performance in a very narrow region.

Finally, the regions 3 and 5 show a lower activity. This follows from the combined effect of a worse buffering strength, the reduction in p_{CO_2} , and inefficient mass transfer of CO_{2,(aq)} through the CL.

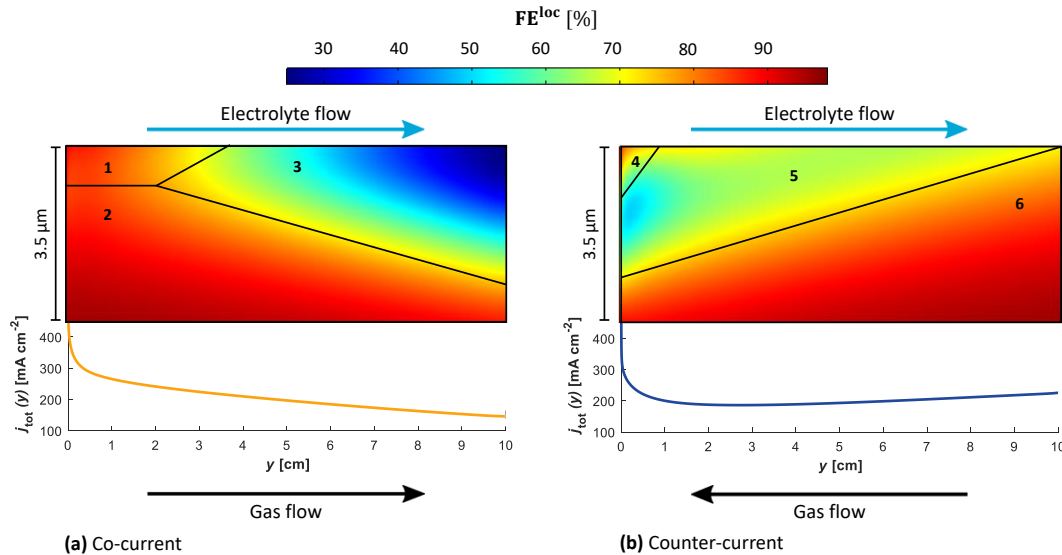


Figure 4.28: FE^{loc} distribution inside the CL for (a) co-current regime and (b) counter-current regime. Below the 2D profile we provide the $j_{\text{tot}}(y)$ distribution where the x-axis correlates with the 2D plot above. All results are provided at $j_{\text{tot}} = 200 \text{ mA cm}^{-2}$. Distinct regions inside the CL are labeled with numbers.

We should also notice that the counter-current regime shows a more stable $j_{\text{tot}}(y)$ and FE^{loc} . Both these metrics reach lower minimal values in the co-current regime. Counter-current regime thus exhibits a better utilisation of the CL. Also, the more evenly distributed $j_{\text{tot}}(y)$ could mitigate the potential issues arising from the uneven distribution of current density. To illustrate, Kas *et al.* point out that uneven distribution of current could accelerate electrode degradation and cause flooding of the GDL.

Based on the large region 3 with low FE^{loc} , one might expect a lower overall FE (Figure 4.27b). The contribution of this region to the overall FE is, however, relatively low because the $j_{\text{tot}}(y)$ is much lower towards the end of the electrolyser. This follows from the way FE is calculated. The overall FE uses the overall j_{COER} and j_{HER} . It is not calculated by averaging the local FE, FE^{loc} .

4.5.2. Variable catalyst loading

A substantial part of the CL is not utilised properly (region 3 in Figure 4.28). We could say that the catalyst in this region is unnecessarily supporting the HER. In fact, Weng *et al.*⁹ has previously shown that it is possible to boost the j_{COER} by decreasing the catalyst loading (Figure 2.6). It is interesting to see what effect this can have in our 2D model. The variation of the catalyst loading is explained in Figure 4.29.

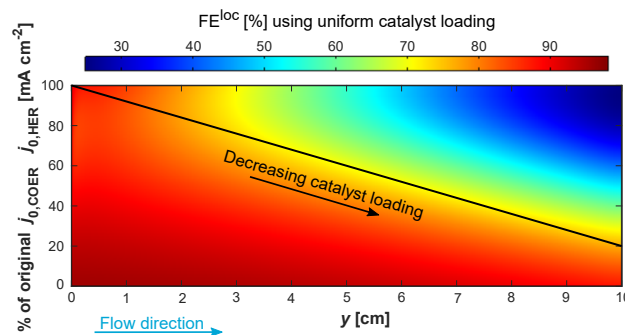


Figure 4.29: Variation of the local catalyst loading by scaling the exchange current densities $j_{0,\text{COER}}$ and $j_{0,\text{HER}}$. At the inlet, where the activity towards the COER is the highest, the catalyst loading is at 100%. This means that $j_{0,\text{COER}}$ and $j_{0,\text{HER}}$ are set to 100% of their original value. Towards the outlet, activity inside the CL decreases which is reflected by linearly decreasing both exchange current densities. At the outlet, $j_{0,\text{COER}}$ and $j_{0,\text{HER}}$ reach 20% of their original values. In the background, FE^{loc} corresponds to the uniform catalyst distribution (co-current simulation).

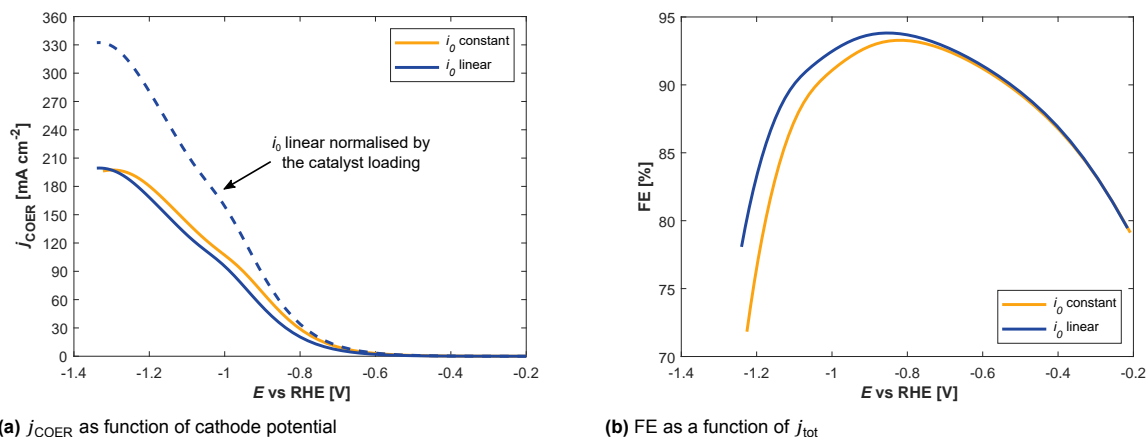
(a) j_{COER} as function of cathode potential(b) FE as a function of j_{tot}

Figure 4.30: Effect of the variable catalyst loading. i_0 constant refers to the model where catalyst loading was not varied. i_0 linear refers to the model where the catalyst loading was decreased linearly. To reflect a real operation of the electrolyser, its length is set to 10 cm and the assumed CO_2 conversion to 80% (subsection 3.2.8). The remaining model parameters correspond to that of the Level 2 model. To normalise the j_{COER} by the catalyst loading, its value reported by the model was divided by 60%. This follows from the distribution of exchange current density which translates to a 40% lower catalyst loading. The normalised and i_0 constant lines both report j_{COER} per the same amount of catalyst, but not necessarily per exactly 1 g of catalyst.

Using the variable catalyst loading leads to lower j_{COER} almost throughout the whole potential window (**Figure 4.30a**). However, the variable catalyst loading slightly prevails only at the most negative potentials starting around -1.2 V. We can compare this finding with the finding published by Weng *et al.*⁹ (**Figure 2.6**). Weng *et al.*⁹ report the j_{COER} to only start to prevail at potentials more negative than -1.1 V vs RHE. This approximately agrees with our finding.

So far we have normalised the current by the area, if we, however, additionally normalise the current density by the amount of catalyst used, we find that j_{COER} can improve by more than 100 mA cm^{-2} (dashed line in **Figure 4.30a**). Similarly as increasing the current density allows to build a shorter electrolyser and therefore reduce the purchase cost, increasing the current density per amount of catalyst used allows to use lesser amount of catalyst and therefore reduce the purchase cost. The results here show that by carefully setting the catalyst loading, amount of CO produced per one gram of catalyst can be significantly increased. This has a potential to improve the cost effectiveness of the CO_2 electrolyser.

The reduced catalyst loading also reports a higher FE (**Figure 4.30b**). To understand why this happens and what is going on inside the CL, we should investigate how the current distribution behaves.

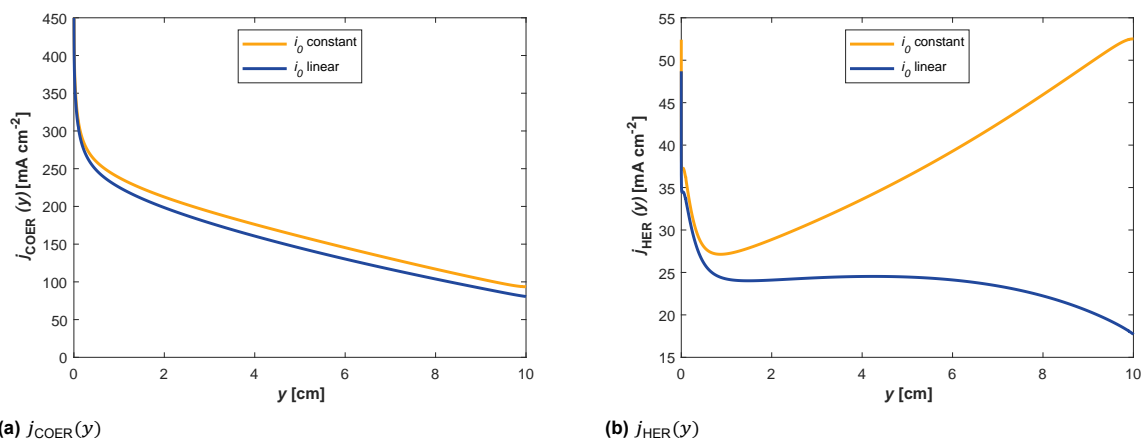
(a) $j_{\text{COER}}(y)$ (b) $j_{\text{HER}}(y)$

Figure 4.31: (a) j_{COER} as a function of the electrolyser length, $j_{\text{COER}}(y)$. (b) j_{HER} as a function of the electrolyser length, $j_{\text{HER}}(y)$. Both results are at -1.16 V vs. RHE. For i_0 constant this corresponds to $j_{\text{tot}} = 205 \text{ mA cm}^{-2}$. For i_0 linear this corresponds to $j_{\text{tot}} = 177 \text{ mA cm}^{-2}$.

Changing the catalyst loading predominantly affects HER rather than COER (**Figure 4.31a**). For the unchanged catalyst loading, the outlet part of the electrolyser is highly active towards HER. However, if we linearly decrease the catalyst loading, $j_{\text{HER}}(y)$ can be reduced. This is because j_{HER} is independent of the reactant concentration (Equation 4.2). Then, decreasing the $j_{0,\text{HER}}$ inherently leads to a lower $j_{\text{HER}}(y)$.

The reason why $j_{\text{COER}}(y)$ is less influenced by the catalyst loading can be attributed to multiple factors. First, for the same electrode potential, but a lower catalyst loading, the total current density will be lower. This shows the **Figure 4.31**, where the sum of the current densities is always lower for the case of variable catalyst loading. This causes less OH^- to be produced and thus the pH to be slightly lower (**Figure D.15**). Second, the lower pH then translates to a lower consumption of $\text{CO}_{2,(\text{aq})}$ in R1 and more $\text{CO}_{2,(\text{aq})}$ is available for the COER (**Figure D.15**). However, against these two beneficial factors acts the reduced $j_{0,\text{COER}}$. As a result, we argue that the distribution of $j_{\text{COER}}(y)$ follows from the balance between these two factors.

For the reported current distribution the FE is increased by as much as 5%. Origin of so enhanced FE follows from the factors stated above. Additionally, one more factor plays a role. When the catalyst loading is reduced, this allows to maintain relatively higher concentration of $\text{CO}_{2,(\text{aq})}$ inside the CL. This is because less $\text{CO}_{2,(\text{aq})}$ is consumed in R1 and in COER). Higher concentration of $\text{CO}_{2,(\text{aq})}$ around the catalyst surface then favours COER over HER (Equation 4.1 and Equation 4.2).

To conclude, here we show that carefully engineering the catalyst distribution throughout the CL could lead to improvements in both FE and j_{COER} . We also show that amount of CO produced per gram of catalyst is significantly higher which could reduce the purchase cost.

5

Conclusion

In this thesis project, we have developed a numerical 2D model of a gas diffusion based CO_2 electrolyser. The model was used to assess the electrolyser performance in terms of current density and faradaic efficiency (FE) under different parameters and configurations.

Through the model validation, we reached a good match in the description of FE. In terms of the current-voltage relationship, the model predicts an exponential growth, but experiments show a linear trend over the considered magnitude. We hypothesised that the developed model misses the ohmic contribution which could be found in the phenomena that were neglected in the model, such as bubble formation in the electrolyte channel.

First, the model showed a deviation from the thermodynamically predicted current density already below 1 mA cm^{-2} which have been assigned to the increasing pH inside the CL. With increasing current density, the distribution of HCO_3^- flux into the CL deviates more and more between the inlet and outlet regions and could be even surpassed by the flux of OH^- out of the CL. This leads to a distinct pH distribution inside the CL which at high currents (200 mA cm^{-2}) diagonally increases from 10.1 at the inlet to 12.2 at the outlet, closer to the gas/liquid interface.

We have identified that the decrease in FE observed at high currents originates from the region of the CL closer to the electrolyte. While the regions closer to the gaseous phase retain high performance (311 mA cm^{-2} , 95% FE), the further end of the CL suffers from mass transfer limitations (250 mA cm^{-2} , 89% FE).

The local variations in the CO_2 solubility showed almost no effect on the overall performance. We have varied Henry's constant as a function of local concentration inside the CL, however, even at the highest currents, the Henry's constant is reduced by only 7% at maximum.

Parametric study

Liquid flow rate

A higher liquid flow rate is shown to improve both current density and FE. We have correlated this improvement with the thickness of the depleted boundary layer of HCO_3^- ions. The higher liquid flow rate reduces this thickness and allows for a better buffering within the CL. Average pH inside the CL decreases from 12.6 at $\text{Re} = 10$ to 11.0 at $\text{Re} = 200$ at 200 mA cm^{-2} . We have shown that at low liquid flow rates ($\text{Re} = 10$) and high currents (200 mA cm^{-2}), the Sherwood number for HCO_3^- ions can reach values significantly lower than 1. This has been explained by the distribution of OH^- flux along the electrolyte/CL boundary.

Electrolyser length

An increasing electrolyser length is shown to negatively influence its performance. We have prescribed this observation to two factors. First, the depleted layer of HCO_3^- ions increases with increasing electrolyser length. At the electrolyte outlet, this layer is wider by a factor of 2 when increasing the electrolyser length from 5 mm to 40 mm. Second, the longer electrolyser underperforms in the outlet part which forces the inlet part to reach a higher current density. This increased current density is shown to decrease the FE in this region due to higher production of OH^- ions.

Operating pressure

Increasing the operating pressure is shown to shift the maximal current from the region around the gas/liquid boundary to the region around the electrolyte/CL boundary. This has been linked to the pH distribution inside the CL. We hypothesised that the current density is limited only by the pH at high operating pressures. This could be due to similarities between the current and pH distribution. However, negative effects arising from higher pressures were not included.

Long electrolyser

We have further adjusted the developed model to investigate behaviour of a long electrolyser (100 cm, industrial) and we have compared its performance to a short electrolyser (4 cm, laboratory). At very low CO_2 conversion, these electrolyser are similar in terms of performance. When increasing the CO_2 conversion, FE decreases significantly faster in the long electrolyser. At 115 mA cm^{-2} this difference is as big as 10%. The achieved CO_2 conversion is also lower, by around 10%. The long electrolyser also requires a higher applied potential to match the current density of a short electrolyser.

The long electrolyser has shown a significantly stronger deviation in FE between the inlet and outlet. At the end of the electrolyser the FE drops to almost 50%. When further coupled with the uneven distribution of current density, we have reported that it takes only the first 33 cm to produce half of the total CO production. This shows that when adding extra length to the long electrolyser, this extra length only adds a fraction of its potential performance.

The origin of so reduced performance has been explained by the pH distribution within the CL. Even at the same current density (115 mA cm^{-2}), the average pH inside the long electrolyser is 12.4 while the pH in the short electrolyser is by 2.0 units lower. We have explained this by the distribution of HCO_3^- and OH^- flux along the electrolyte/CL boundary and the partial pressure of CO_2 .

Strategies to improve the performance of long electrolysers

By setting the fluid flow into the counter-current regime, we have investigated what effect the combination of low partial pressure of CO_2 with a high supply of HCO_3^- ions, and vice versa, has on the electrolyser performance. However, when comparing the results to the co-current regime, we have found no substantial improvement in current density or FE. This was explained by the small size of the region where electrolyte brings a beneficial effect. One advantage following from the counter-current regime lies in more evenly distributed current density and FE. This could be important in cases where uneven current distribution influences the stability of the electrode.

Decreasing the catalyst loading along the flow direction has been shown to positively influence FE, and at the most negative potentials, also the current density. We have also shown that the amount of CO produced per 1 g of catalyst significantly increased. As the catalyst loading decreased, we have explained that this can suppress the evolution of H_2 while the evolution of CO remains almost unchanged. We claimed that the lower current density leads to a lower production OH^- ions and thus to a lower pH. Thereafter, the lower pH, and the higher amount of available CO_2 , maintained the CO evolution almost unchanged, although less catalyst was used. Carefully engineering the catalyst distribution over the length of CL could not only help to increase the FE in the outlet regions but could also improve the cost-effectiveness of the CO_2 electrolyser.

6

Recommendations

Modelling a CO₂ electrolyser

The major drawback of the developed model is its incapability to capture the ohmic losses. Further development should prioritize solving this issue. We have pointed out that this missing contribution could originate from two. First, it is the position of the reversible hydrogen electrode (RHE). The position of RHE should be defined and resistance arising from the distance between the RHE and CL should be included. Second, the resistance originating from the gas evolution in the electrolyte channel should be included. Including the two-phase flow might be necessary. Finally, the effect of the microporous layer (MPL) in terms of gas diffusion should be included. MPL could also contribute to the ohmic drop. Gas solubility could be better addressed. We assumed the CO₂ solubility to be determined by the concentration on the gas/liquid interface. Future study could average the concentration over x axis in the whole CL and use this value.

The model could be further extended to reflect the whole CO₂ electrolyser. Modelling the whole electrolyser would allow to directly compare the current vs cell voltage relationship. It could also help to identify the missing ohmic contribution.

It would be also interesting to investigate the effect bubble evolution arising at the cathode, the effect of various kinetic parameters (concentration term in Butler-Volmer equation does not have to relate only to a power of one¹⁰), the effect of excluding the pH from equilibrium potential (Kas *et al.*⁶), the effect of liquid present in the GDL, and others. Comparing the results of these simulations to a large set of experimental data could identify which additional phenomena are occurring inside the electrolyser. Knowing these, one could better explain and optimize the electrolyser operation.

We showed that the long electrolyser does not perform well in terms of both current and FE. Future studies could utilise the settings of this model to investigate the effect of unusual cell configurations.

Physical CO₂ electrolyser

Using the distribution of FE inside the CL, we have shown that regions farther away from the gaseous phase could be better supplied with CO₂. Experimental research should focus on the arrangement and composition of the CL that would allow to feed the gaseous CO₂ even to the distant regions.

From the parametric study follows that the only parameter that can significantly enhance the electrolyser performance is the operating pressure. The experimental research should focus on the development of electrolyser cells that would show stable operation under high pressures. Pressurizing the fluids and the gain in the performance should be economically assessed in detail.

The decrease in FE is inevitable as the partial pressure of CO₂ decreases along the flow direction. We have shown that the variable catalyst loading could potentially overcome some of these issues. Future experimental studies could focus on the engineering of a non-uniform catalyst layer. Perhaps, even a combination of different catalysts could mitigate the rate of H₂ evolution around the outlet of the CL.

Acknowledgments

Foremost, I would like to thank my supervisors, Lorenz Baumgartner and Joe Blake. I am really grateful for all the time you put into this project. I have learned a lot from you and I look forward to using this knowledge in the future. I also enjoyed working with you both and I am truly happy this project happened.

I would also like to thank David Vermaas for the guidance and for leading the EFS group.

Another thank you goes to all the people in the EFS group. I was happy having you in the weekly meetings and sharing the time with you outside of office hours.

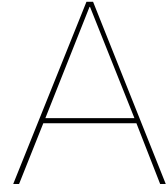
A special thank you belongs to my parents. Without the support of my parents, I would not be able to spend time doing things I like.

I would also like to thank all my friends in Delft who make the student life more fun.

Bibliography

- (1) Goldemberg, J., *World energy assessment. Energy and the challenge of sustainability*, New York, NY, 2001, p 528.
- (2) Kibria, M. G.; Edwards, J. P.; Gabardo, C. M.; Dinh, C. T.; Seifitokaldani, A.; Sinton, D.; Sargent, E. H. *Advanced Materials* **2019**, *31*, 1–24.
- (3) Jouny, M.; Luc, W.; Jiao, F. *Industrial and Engineering Chemistry Research* **2018**, *57*, 2165–2177.
- (4) Smith, W. A.; Burdyny, T.; Vermaas, D. A.; Geerlings, H. *Joule* **2019**, *3*, 1822–1834.
- (5) De Luna, P.; Hahn, C.; Higgins, D.; Jaffer, S. A.; Jaramillo, T. F.; Sargent, E. H. *Science* **2019**, *364*, DOI: 10.1126/science.aav3506.
- (6) Kas, R.; Star, A. G.; Yang, K.; Van Cleve, T.; Neyerlin, K. C.; Smith, W. A. *ACS Sustainable Chemistry and Engineering* **2021**, *9*, 1286–1296.
- (7) Yang, Z.; Li, D.; Xing, L.; Xiang, H.; Xuan, J.; Cheng, S.; Yu, E. H.; Yang, A. *ACS Sustainable Chemistry & Engineering* **2021**, *9*, 351–361.
- (8) Wu, K.; Birgersson, E.; Kim, B.; Kenis, P. J. A.; Karimi, I. A. *Journal of The Electrochemical Society* **2015**, *162*, F23–F32.
- (9) Weng, L. C.; Bell, A. T.; Weber, A. Z. *Physical Chemistry Chemical Physics* **2018**, *20*, 16973–16984.
- (10) Weng, L. C.; Bell, A. T.; Weber, A. Z. *Energy and Environmental Science* **2019**, *12*, 1950–1968.
- (11) Kotb, Y.; Fateen, S.-E. K.; Albo, J.; Ismail, I. *Journal of The Electrochemical Society* **2017**, *164*, E391–E400.
- (12) El-Shafie, O. A.; El-Maghraby, R. M.; Albo, J.; Fateen, S. E. K.; Abdelghany, A. *Industrial and Engineering Chemistry Research* **2020**, *59*, DOI: 10.1021/acs.iecr.0c02358.
- (13) Hori, Y. In *Modern Aspects of Electrochemistry*, Vayenas, C. G., White, R. E., Gamboa-Aldeco, M. E., Eds.; Springer New York: New York, NY, 2008, pp 89–189.
- (14) Endrődi, B.; Bencsik, G.; Darvas, F.; Jones, R.; Rajeshwar, K.; Janáky, C. *Progress in Energy and Combustion Science* **2017**, *62*, 133–154.
- (15) Zhang, W.; Qin, Q.; Dai, L.; Qin, R.; Zhao, X.; Chen, X.; Ou, D.; Chen, J.; Chuong, T. T.; Wu, B.; Zheng, N. *Angewandte Chemie International Edition* **2018**, *57*, 9475–9479.
- (16) Sun, X.; Zhu, Q.; Kang, X.; Liu, H.; Qian, Q.; Zhang, Z.; Han, B. *Angewandte Chemie International Edition* **2016**, *55*, 6771–6775.
- (17) Burdyny, T.; Smith, W. A. *Energy and Environmental Science* **2019**, *12*, 1442–1453.
- (18) Salvatore, D. A.; Weekes, D. M.; He, J.; Dettelbach, K. E.; Li, Y. C.; Mallouk, T. E.; Berlinguette, C. P. *ACS Energy Letters* **2018**, *3*, 149–154.
- (19) Reyes, A.; Jansonius, R. P.; Mowbray, B. A. W.; Cao, Y.; Wheeler, D. G.; Chau, J.; Dvorak, D. J.; Berlinguette, C. P. *ACS Energy Letters* **2020**, *5*, 1612–1618.
- (20) Whipple, D. T.; Finke, E. C.; Kenis, P. J. *Electrochemical and Solid-State Letters* **2010**, *13*, 109–111.
- (21) Jeanty, P.; Scherer, C.; Magori, E.; Wiesner-Fleischer, K.; Hinrichsen, O.; Fleischer, M. *Journal of CO2 Utilization* **2018**, *24*, 454–462.
- (22) Pärnamäe, R.; Mareev, S.; Nikonenko, V.; Melnikov, S.; Sheldeshov, N.; Zabolotskii, V.; Hamelers, H. V.; Tedesco, M. *Journal of Membrane Science* **2021**, *617*, DOI: 10.1016/j.memsci.2020.118538.

- (23) Bard, A. J.; Faulkner, L. R., *ELECTROCHEMICAL METHODS Fundamentals and Applications*, 2nd; Harris, D., Swain, E., Aiello, E., Eds.; John Wiley & Sons, Inc.: 2001, p 833.
- (24) Nesbitt, N. T.; Burdyny, T.; Simonson, H.; Salvatore, D.; Bohra, D.; Kas, R.; Smith, W. A. *ACS Catalysis* **2020**, *10*, 14093–14106.
- (25) Nesbitt, N. T.; Smith, W. A. *Journal of Physical Chemistry C* **2021**, *125*, 13085–13095.
- (26) Jerkiewicz, G. *ACS Catalysis* **2020**, *10*, 8409–8417.
- (27) Gupta, N.; Gattrell, M.; MacDougall, B. *Journal of Applied Electrochemistry* **2006**, *36*, 161–172.
- (28) Schulz, K. G.; Riebesell, U.; Rost, B.; Thoms, S.; Zeebe, R. E. *Marine Chemistry* **2006**, *100*, 53–65.
- (29) Hashiba, H.; Weng, L. C.; Chen, Y.; Sato, H. K.; Yotsuhashi, S.; Xiang, C.; Weber, A. Z. *Journal of Physical Chemistry C* **2018**, *122*, 3719–3726.
- (30) Taylor, R.; Krishna, R., *MULTICOMPONENT MASS TRANSFER*; John Wiley & Sons, Inc.: 1993, p 580.
- (31) Deen, W. M., *ANALYSIS OF TRANSPORT PHENOMENA*, 2nd; Oxford University Press USA: 2012, p 606.
- (32) COMSOL Multiphysics® v. 5.5., *Chemical Reaction Engineering Module User's Guide*.
- (33) Bruggeman, D. A. G. *Annalen der Physik* **1935**, *416*, 636–664.
- (34) Chung, D.-W.; Ebner, M.; Ely, D.; Wood, V.; García, E. *Modelling Simul. Mater. Sci. Eng.* **2013**, *21*, 4009–.
- (35) Sander, R. *Atmospheric Chemistry and Physics* **2015**, *15*, 4399–4981.
- (36) Atkins, P.; Paula, J. d., *ATKIN'S PHYSICAL CHEMISTRY*, 8th; Oxford University Press: 2006, p 1053.
- (37) Setschenow, J. *Zeitschrift für Physikalische Chemie* **1889**, *4U*, 117–125.
- (38) Schumpe, A. *Chemical Engineering Science* **1993**, *48*, 153–158.
- (39) Weisenberger, S.; Schumpe, A. *AIChE Journal* **1996**, *42*, 298–300.
- (40) Rawlings, J. B.; Ekerdt, J. G., *Chemical Reactor Analysis and Design Fundamentals*, 2nd; Nob Hill Publishing: 2004.
- (41) COMSOL Multiphysics® v. 5.3., *Electrochemistry Module User's Guide*.
- (42) In *Flow through Heterogeneous Geologic Media*, Carroll, K. C., Khaleel, R., Yeh, T.-C., Eds.; Cambridge University Press: Cambridge, 2015, pp 32–68.
- (43) Neuman, S. P. *Acta Mechanica* **1977**, *25*, 153–170.
- (44) COMSOL Multiphysics® v. 5.3., *CFD Module User's Guide*.
- (45) Carman, P. C. *Chemical Engineering Research and Design* **1997**, *75*, S32–S48.
- (46) Larrazábal, G. O.; Ma, M.; Seger, B. *Accounts of Materials Research* **2021**, *2*, 220–229.
- (47) Verma, S.; Lu, X.; Ma, S.; Masel, R. I.; Kenis, P. J. *Physical Chemistry Chemical Physics* **2016**, *18*, 7075–7084.
- (48) El-Kharouf, A.; Mason, T. J.; Brett, D. J.; Pollet, B. G. *Journal of Power Sources* **2012**, *218*, 393–404.
- (49) <https://webbook.nist.gov/cgi/cbook.cgi?ID=C7732185> NIST Chemistry WebBook, Water.
- (50) <https://webbook.nist.gov/cgi/cbook.cgi?ID=124-38-9>; NIST Chemistry WebBook, Carbon dioxide.
- (51) Yang, K.; Kas, R.; Smith, W. A.; Burdyny, T. *ACS Energy Letters* **2021**, *6*, 33–40.
- (52) Koopman, C. Scale-up Limitations of Carbon-based Gas Diffusion Electrodes (GDEs) for Electrochemical CO₂ Reduction, 2021.
- (53) Yan, Z.; Hitt, J. L.; Zeng, Z.; Hickner, M. A.; Mallouk, T. E. *Nature Chemistry* **2021**, *13*, 33–40.
- (54) Lin, T. Y.; Baker, S. E.; Duoss, E. B.; Beck, V. A. *Industrial and Engineering Chemistry Research* **2021**, *60*, 11824–11833.
- (55) COMSOL Blog; Schlegel, F. Understanding Stabilization Methods, 2014.



Initial values

The following tables present the initial values for the other 3 modelled cases.

Table A.1: Non-saturated electrolyte, 0.5 M KHCO_3 , $p_{\text{abs}} = 1 \text{ atm}$

Variable	Initial value	Unit	Variable	Initial value	Unit
$c_{\text{CO}_2,(\text{aq})}$	5.19	mM	ϕ_l	0	V
$c_{\text{HCO}_3^-}$	489.63	mM	ϕ_s	-0.49	V
$c_{\text{CO}_3^{2-}}$	5.19	mM	ω_{CO_2}	99.99	%
c_{OH^-}	$2.21 \cdot 10^{-3}$	mM	ω_{CO}	0.001	%
c_{H^+}	$4.52 \text{ e} - 6$	mM	ω_{H_2}	0.001	%
p	0	Pa	ω_{N_2}	0.008	%

Table A.2: Electrolyte in equilibrium with 3 atm CO_2 , 0.5 M KHCO_3 , $p_{\text{abs}} = 3 \text{ atm}$

Variable	Initial value	Unit	Variable	Initial value	Unit
$c_{\text{CO}_2,(\text{aq})}$	98.87	mM	ϕ_l	0	V
$c_{\text{HCO}_3^-}$	499.43	mM	ϕ_s	-0.41	V
$c_{\text{CO}_3^{2-}}$	0.28	mM	ω_{CO_2}	99.99	%
c_{OH^-}	$1.18 \cdot 10^{-4}$	mM	ω_{CO}	0.001	%
c_{H^+}	$8.45 \cdot 10^{-5}$	mM	ω_{H_2}	0.001	%
p	0	Pa	ω_{N_2}	0.008	%

Table A.3: Electrolyte in equilibrium with 5 atm CO_2 , 0.5 M KHCO_3 , $p_{\text{abs}} = 5 \text{ atm}$

Variable	Initial value	Unit	Variable	Initial value	Unit
$c_{\text{CO}_2,(\text{aq})}$	164.78	mM	ϕ_l	0	V
$c_{\text{HCO}_3^-}$	499.66	mM	ϕ_s	-0.40	V
$c_{\text{CO}_3^{2-}}$	0.17	mM	ω_{CO_2}	99.99	%
c_{OH^-}	$7.11 \cdot 10^{-5}$	mM	ω_{CO}	0.001	%
c_{H^+}	$1.41 \cdot 10^{-4}$	mM	ω_{H_2}	0.001	%
p	0	Pa	ω_{N_2}	0.008	%

B

Optional solver configurations

The following describes different modifications to the way model can be solved. These methods are supposed to improve model convergence and enable the model to converge even at high current densities. Most of these methods helped to improve the convergence, but were still unsuccessful at currents higher than 80 mA cm^{-2} . These methods are not included in the final model.

Reaction rate ramping

Concentration of species inside the electrolyte channel could be solved when excluding the homogeneous reactions. However, homogeneous reactions play crucial role in the electrolyser performance.⁶ Thus, the solver sequence as visualized in **Figure B.1** was proposed and tested.

		Potential sweep						
		aux	0	0.25	0.5	0.75	1	...
Reaction ramp	f							
	1×10^{-8}		1	10	19	28	37	...
	1×10^{-7}		2	11	20	29	38	...
	1×10^{-6}		3	12	21	30	39	...
	1×10^{-5}		4	13	22	31	40	...
	1×10^{-4}		5	14	23	32	41	...
	1×10^{-3}		6	15	24	33	42	...
	1×10^{-2}		7	16	25	34	43	...
	1×10^{-1}		8	17	26	35	44	...
	1		9	18	27	36	45	...

Figure B.1: Solver sequence coupling reaction ramp and potential stepping. Blue arrows represent the way at which the simulations were solved and the numbers then represent separate simulations. Green arrows represent the way at which the initial values were transferred between the simulations. f is a factor multiplying the reaction rate, aux represents potential stepping. Simulations highlighted in red are the desired results.

In this approach, rate of the homogeneous reactions is in each step increased by a factor, f , of 10 (blue vertical arrows) until the rate constants reach their original values. Initial values are loaded from the previous step. To achieve higher current density, potential is increased step by step (aux) and in each of these steps the reaction ramp starts again with the lowest reaction rate.

The advantage here is that the concentrations in the electrolyte and CL are with each reaction ramp step updated to a higher reaction rate while using initial values that should be close to the next solution. However, this approach still does not converge at high currents. It commonly crashes step or two before $f = 1$. To note, reaction ramp was set up as auxiliary sweep. This means that f was further refined if the simulation at the next value of f did not converge.

Manual scaling

At high currents, the variations in concentration can span across wide orders of magnitude. That is significantly different from the initial state. Since scaling relates to the relative error, it should be properly set. However, during the potential sweep, the log file did not report scales for the dependent variables to be adjusting. This was observed for a case when automatic damping was used.

Thus, we could expect a proper scaling to improve the convergence. We can estimate the scales for the dependent variables as follows. 1, model without the homogeneous reaction is solved across the desired potential range. 2, at each potential, the maximum value of each variable is saved. 3, this maximum is expressed as a function of applied potential. 4, this dependency is fitted with appropriate polynomial. 5, the obtained polynomial function is introduced into the model. 6. The final model is run with the homogeneous reactions and the potential sweep while scaling for each variable at each potential is determined from the prescribed polynomial function.

However, this method proved not very efficient. Further, at higher current densities, still a substantial difference in the magnitudes of the dependent variables was observed when including and excluding the homogeneous reactions. This means that scaling determined from the model without homogeneous reactions is still not well applicable to the model with homogeneous reactions. This is because the magnitude of the variables still changes substantially.

Equilibrium reactions and equilibrium flux of H^+

The other option how to describe the fast homogeneous reactions, R1 and R4, is to use the equilibrium constants. However, no substantial improvement in the solver convergence was achieved. This might be due to equilibrium being a strict condition. Especially, enforcing the equilibrium constraint around the anode was identified as a root of the problem.

To combat the issues in the local environment of the anode, H^+ flux was modified such that it is entering the electrolyte channel already in equilibrium with CO_3^{2-} and HCO_3^- according to R4. To achieve this, concentration near the anode boundary was used to calculate a new equilibrium constant. Then, the ratio between the new equilibrium constant and the tabulated value of the equilibrium constant was computed. Then, the ion flux into the electrolyte boundary was distributed as a source of H^+ and CO_3^{2-} , and a sink of HCO_3^- . However, no substantial improvement was observed. This might be due to an overstrict boundary condition which requires high tolerance.

Stabilization methods

Numerical instabilities can arise in cases where the model is driven by convection (applies to the electrolyte channel). This then leads to oscillation in the solution. Consider species transport equation, it was shown that under certain conditions, numerical instabilities arise when Peclet number, Pe , (Equation B.1) is higher than one.⁵⁵

$$Pe = \frac{\|\mathbf{u}\|h}{2D} \quad (B.1)$$

Above, h represents mesh element size. To reduce the oscillations, solvers adds two stabilization methods by default. These lower the Pe by adding an artificial diffusion to the Equation B.1. However, less artificial diffusion is added when a solution is closer to the exact solution.⁵⁵

Another available stabilization is isotropic diffusion. It adds a constant amount of artificial diffusion no matter how close to the solution is to the exact solution. Here, the Pe is modified into Equation B.2.⁵⁵

$$Pe = \frac{\|\mathbf{u}\|h}{2D + 2\delta h\|\mathbf{u}\|} \quad (B.2)$$

Above, δ represents a tuning parameter controlling the amount of added artificial diffusion. When high enough δ was used, model converged even at higher currents. However, the concentration profiles were too heavily influenced (**Figure B.2**). Consequently, it was decided not use the isotropic diffusion since the species distribution inside the channel and in the CL is a crucial and desired result.

Adaptive meshing

Based on stabilization method above, it could be said that the meshing is a primary issue defying the model from convergence. As the species get created or consumed near the electrode boundaries, the size of the boundary layer region changes. This means, that manually refined mesh is only applicable to a small range of current density.

To automatically refine the meshing we tested the built in COMSOL function, adaptive mesh refinement. This function automatically refines the mesh in regions of high errors. However, this method

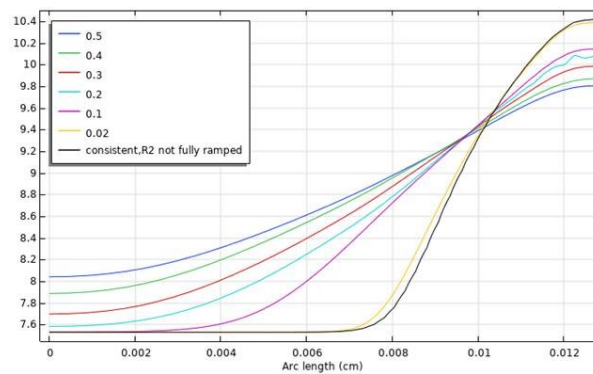


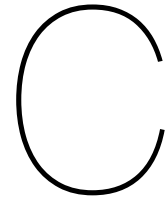
Figure B.2: Effect of isotropic diffusion on the pH profile (y -axis) at the outlet of the electrolyte channel (x -axis) for different tuning factors δ . Consistent refers to a stabilization method that adds less artificial diffusion when a solution is closer to the exact solution.

was extremely time consuming and thus abandoned in favor of later described methods.

Other methods

To close up, additional adjustments were tested too see how the convergence improves. These include:

- Using a segregated solver to decouple concentration and potential variables. Coupling between the variables and thus the computational time and oscillations were slightly reduced.
- To enforce the positive concentrations, all the reaction terms were corrected as: $\max(0, c_i)$ (common suggestion). No significant improvement in convergence was observed.
- Using higher order discretization methods. When scaling up the geometry model becomes extremely computationally expensive.
- The model should experience less numerical instability when convection is lower (Equation B.1). Thus, Re was ramped up similarly to the reaction ramp (**Figure B.1**).
- Any combination of the above.



Model validation

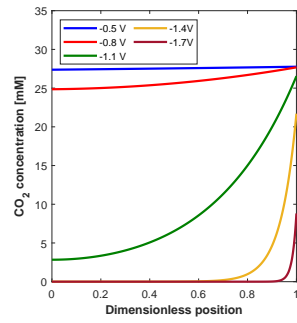
In this chapter we provide validation of different models. First, the validation of 1D model is presented. Second, validation of the model describing the long electrolyser is presented. Finally, more details on the validation of the small-scale model are provided.

C.1. 1D model

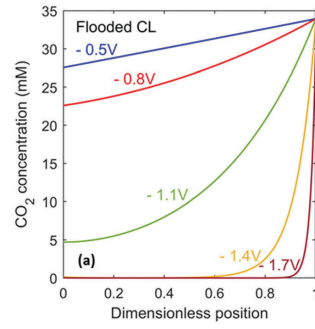
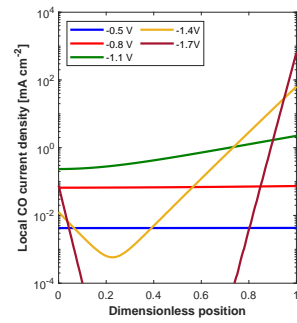
We firstly developed a 1D model according to the model developed by Weng *et al.* To validate our model, we can just compare our results to the result report by these authors. This comparison is provided in the figures on the next page.

The dimensionless position refers to the width of the CL. 0 thus refers to the electrolyte/CL boundary and 1 refers to the gas/liquid boundary. All potentials are reported against RHE.

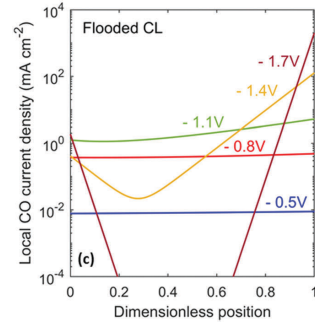
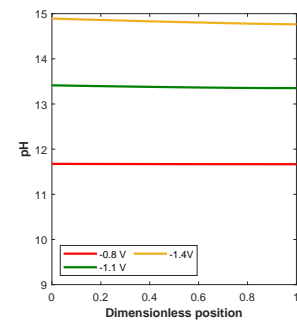
We have not investigated the differences between the two models in more detail. This is because the aim of this work was to develop a more elaborate 2D model. Thus, the precise validity of the 1D model is not crucial.



(a) Our 1D model

(b) Weng *et al.*⁹Figure C.1: $c_{\text{CO}_2,(\text{aq})}$ distribution inside the CL

(a) Our 1D model

(b) Weng *et al.*⁹Figure C.2: $j_{\text{COER}}^{\text{loc}}$ distribution inside the CL

(a) Our 1D model

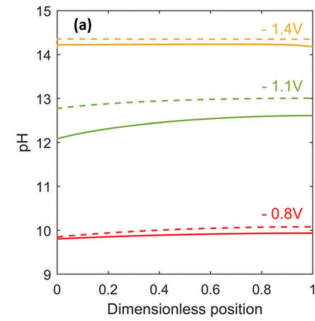
(b) Weng *et al.*⁹ dashed lines: partly flooded CL

Figure C.3: pH distribution inside the CL

C.2. Long electrolyser

The boundary conditions used in the model of the long electrolyser (**Table 3.4**) do not reflect the real physical connection between the subcells. These are rather mathematical approximations. Thus, here we reveal the impact of merging the three subsequent subcells. To achieve this, we compare two models. These models are identical up to one being composed of three subcells. The results are presented in **Table C.1** and **Figure C.4**.

Variable	Subcells	Full	Unit
j_{COER}	146.6	145.8	mA cm^{-2}
j_{HER}	19.9	20.1	mA cm^{-2}
FE	88.0	87.9	%

Table C.1: Comparison between the Subcells and Full models. Subcells model represents an electrolyser that is composed of three subcells each with a length of 4 cm. Full model represents an electrolyser that was modeled as a whole.

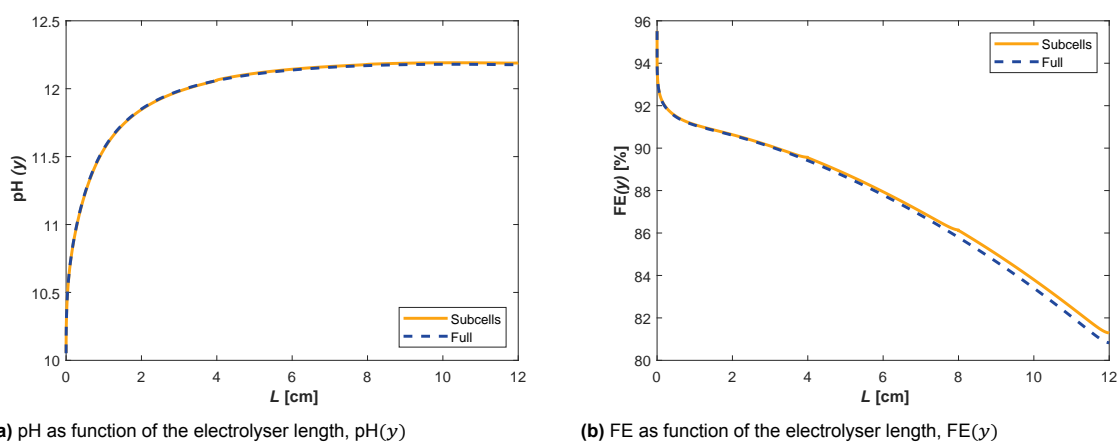


Figure C.4: Comparison between the Subcells and Full models. Subcells model represents an electrolyser that is composed of three subcells each with a length of 4 cm. Full model represents an electrolyser that was modeled as a whole.

C.2.1. Numerical and analytical predictions

Sherwood-Reynolds-Schmidt correlation

The Sherwood-Reynolds-Schmidt correlation is defined in Equation C.1. From this correlation we can compute the mass transfer coefficient, $k_{\text{HCO}_3^-}$ and then from the mass transfer coefficient the thickness of the boundary layer, L_{bl,HCO_3^-} (Equation C.2).

$$k_{\text{HCO}_3^-} = \frac{D_{\text{HCO}_3^-}}{L} 0.664 \left(\frac{\rho_l \bar{u} L}{\mu_l} \right)^{1/2} \left(\frac{\mu_l}{\rho_l D_{\text{HCO}_3^-}} \right)^{1/3} \quad (\text{C.1})$$

$$L_{bl,\text{HCO}_3^-} = \frac{D_{\text{HCO}_3^-}}{k_{\text{HCO}_3^-}} \quad (\text{C.2})$$

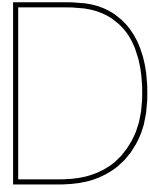
$c_{\text{CO}_2,(\text{aq})}$ distribution inside the CL

To calculate distribution of the dissolved CO_2 inside the CL, we used the equations below. These equations were derived by Joe Blake. $c_{\text{CO}_2,(\text{aq})\text{CL/GDL}}$ refers to the $c_{\text{CO}_2,(\text{aq})}$ at the CL/GDL boundary.

$$k = \epsilon_{l,\text{CL}} k_1 c_{\text{OH}^-}(y) + \frac{a}{2F} \frac{j_{0,\text{COER}}}{c_0^*} e^{-\frac{\eta_{a,\text{COER}} F \alpha_{\text{COER}}}{RT}} \quad (\text{C.3})$$

$$M_T = \sqrt{\frac{W_{\text{CL}}^2 k}{D_{\text{CO}_2,(\text{aq})}^{\text{eff}}}} \quad (\text{C.4})$$

$$c_{\text{CO}_2,(\text{aq})} = c_{\text{CO}_2,(\text{aq})\text{CL/GDL}} \frac{\cosh(M_T(1-x/L))}{\cosh(M_T)} \quad (\text{C.5})$$



Supporting results

D.1. Phenomena governing the electrolyser performance

D.1.1. Behaviour at higher current density $> 10 \text{ mA cm}^{-2}$

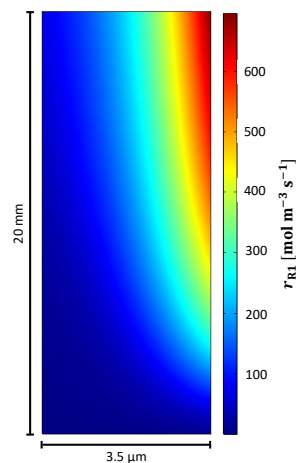


Figure D.1: Distribution of the R1 net reaction rate inside the CL at $j_{\text{tot}} = 224 \text{ mA cm}^{-2}$. More $\text{CO}_{2,(\text{aq})}$ is consumed in the outlet region closer to the CL/GDL boundary. This matches well with the pH distribution (**Figure 4.7a**). Lower consumption near the electrolyte/CL boundary follows from already low $c_{\text{CO}_{2,(\text{aq})}}$ in this region (**Figure 4.7c**).

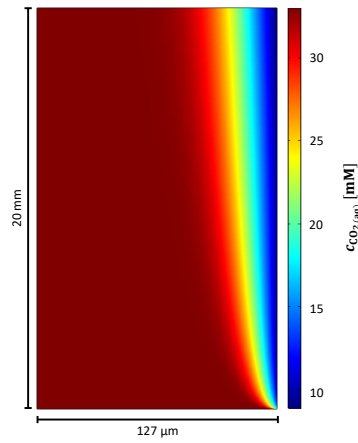


Figure D.2: $c_{\text{CO}_2(\text{aq})}$ inside the right half of the electrolyte channel at $j_{\text{tot}} = 224 \text{ mA cm}^{-2}$. $\text{CO}_{2(\text{aq})}$ creates a depleted boundary layer in the electrolyte channel for two reasons. First, $\text{CO}_{2(\text{aq})}$ is being consumed in CL which creates gradient in $c_{\text{CO}_2(\text{aq})}$ and thus a diffusional flux into the CL. Second, portion of the OH^- ions leaving the CL react with $\text{CO}_{2(\text{aq})}$ via R1. This flux of OH^- increases in the flow direction as well, thus, contributing to the distinct $c_{\text{CO}_2(\text{aq})}$ profile.

D.1.2. Local salting-out effect

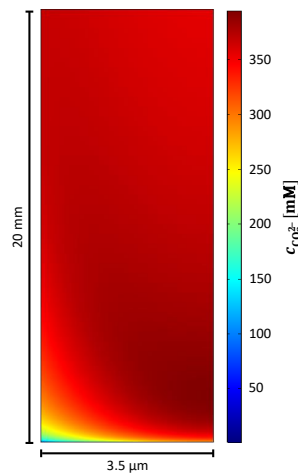
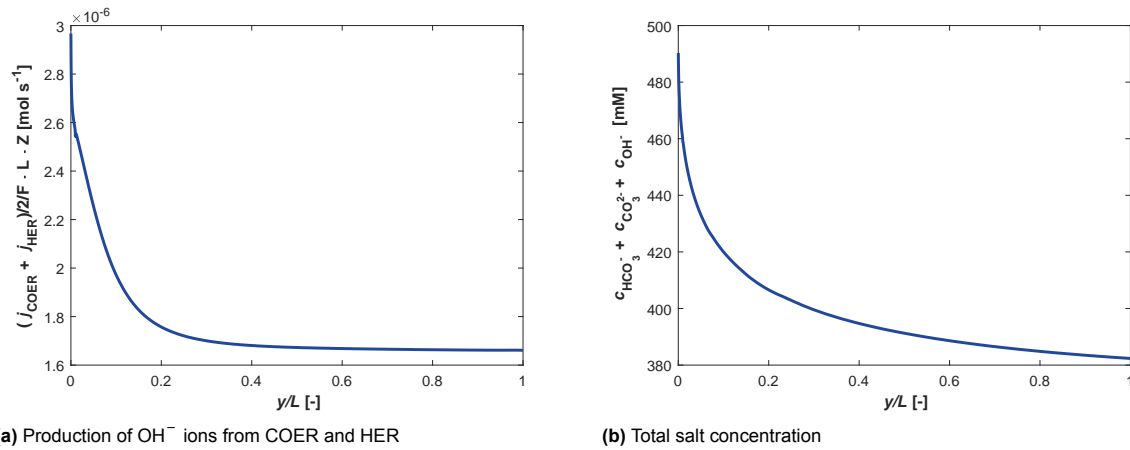


Figure D.3: $c_{\text{CO}_3^{2-}}$ inside the CL at $j_{\text{tot}} = 224 \text{ mA cm}^{-2}$. Notice how $c_{\text{CO}_3^{2-}}$ firstly strongly increases, the dark red area, but later towards the outlet its $c_{\text{CO}_3^{2-}}$ starts to decrease, the dark red changes to light red.

(a) Production of OH^- ions from COER and HER

(b) Total salt concentration

Figure D.4: (a) the total production of OH^- ions originating from the COER and the HER (b) sum of $c_{\text{HCO}_3^-}$, $c_{\text{CO}_3^{2-}}$, and c_{OH^-} which is equal to the total salt concentration. Both (a) and (b) correspond to the CL/GDL boundary and to $j_{\text{tot}} = 224 \text{ mA cm}^{-2}$. The model includes the salting-out effect and the length of the electrolyser is 2 cm. (a) proves that generation of OH^- ions is decreasing towards the outlet and (b) proves that the total salt concentration decreases towards the outlet.

D.2. Parametric study

D.2.1. Liquid flow rate

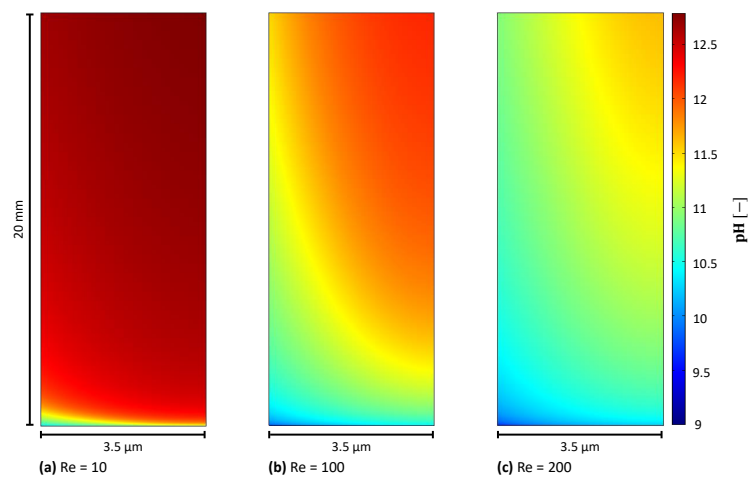


Figure D.5: pH profile inside the CL at different electrolyte flow rates at $j_{\text{tot}} = 200 \text{ mA cm}^{-2}$. A higher pH at a lower liquid flow rate is a consequence of the lowered flux of HCO_3^- ions.

D.2.2. Electrolyser length

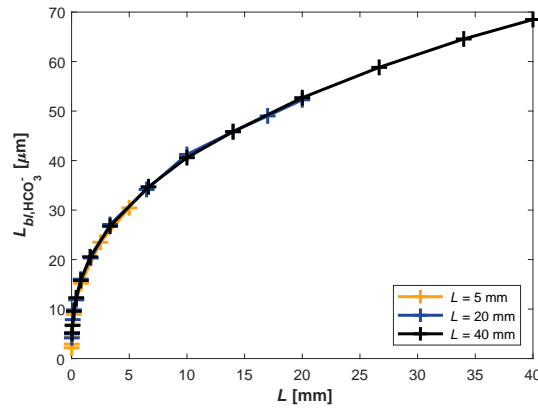


Figure D.6: Evolution of the the boundary layer thickness of HCO_3^- ions, L_{bl,HCO_3^-} , as a function of the electrolyser length L . All approximately at $j_{\text{tot}} = 200 \text{ mA cm}^{-2}$. This thickness was determined for a number of discrete points by calculating the coordinates of the point inside the electrolyte channel where $c_{\text{HCO}_3^-}$ reached 99% of its $c_{\text{HCO}_3^-}$ initial. We see that L_{bl,HCO_3^-} evolves approximately the same across the common electrolyser length. The longer the electrolyser, the longer L_{bl,HCO_3^-} at the outlet of the channel.

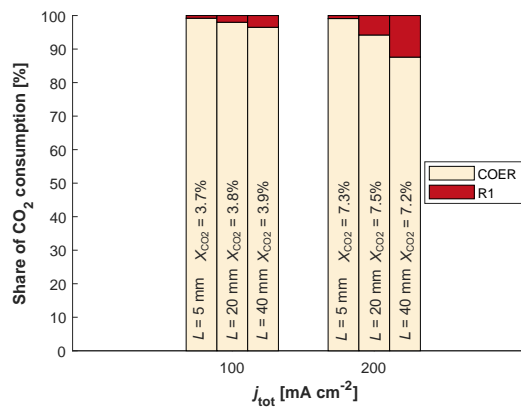


Figure D.7: Share of CO_2 consumption and achieved CO_2 conversion, X_{CO_2} . Increasing length of the electrolyser results in worse utilization of $\text{CO}_{2,(aq)}$, that is, to more $\text{CO}_{2,(aq)}$ being consumed in R1. The variation in X_{CO_2} arises from the fact that j_{tot} is not exact but can deviate up to 5 mA cm^{-2} .

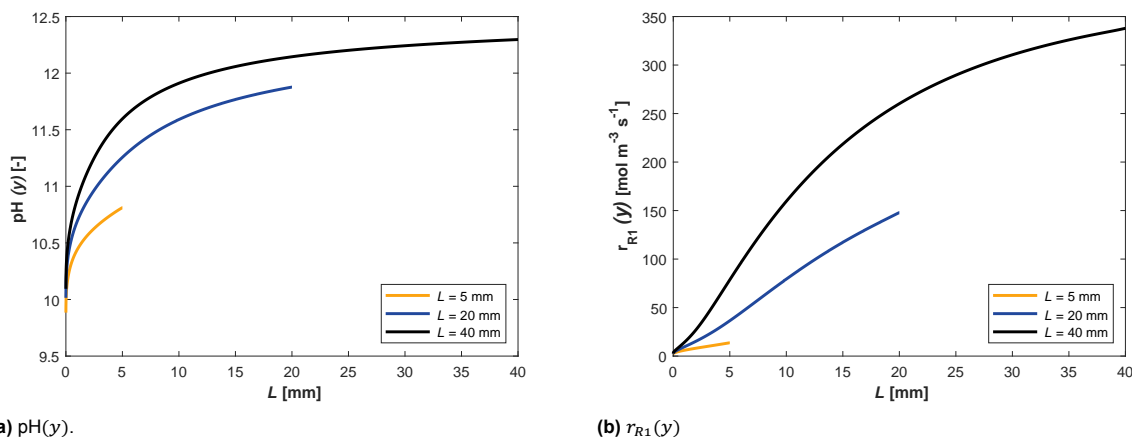


Figure D.8: (a) pH as a function of electrolyser length, $\text{pH}(y)$. (b) r_{R1} as function of electrolyser length, $r_{R1}(y)$. (a) increasing the electrolyser length leads to a higher pH already in the inlet region. pH is overall higher in the longer electrolyser. (b) higher production of OH^- also significantly increases the $r_{R1}(y)$ and thus decreases the amount of available $\text{CO}_{2(aq)}$ for the COER.

D.2.3. Operating pressure

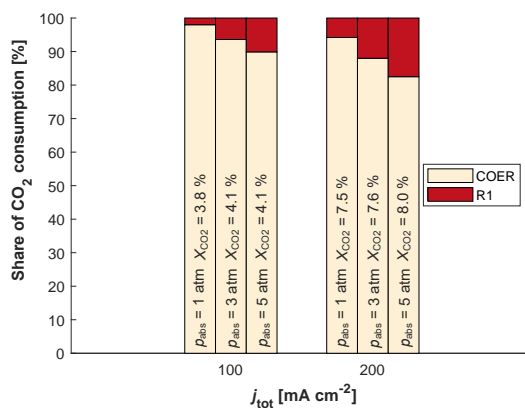


Figure D.9: Share of CO_2 consumption and achieved CO_2 conversion X_{CO_2} . With increasing p_{abs} , both solubility and supply of $\text{CO}_{2(aq)}$ increase and thereafter consumption in R1 increases. X_{CO_2} increases as a result of a higher FE (Figure 4.17b).

D.3. CO₂ electrolyser with 1 m length

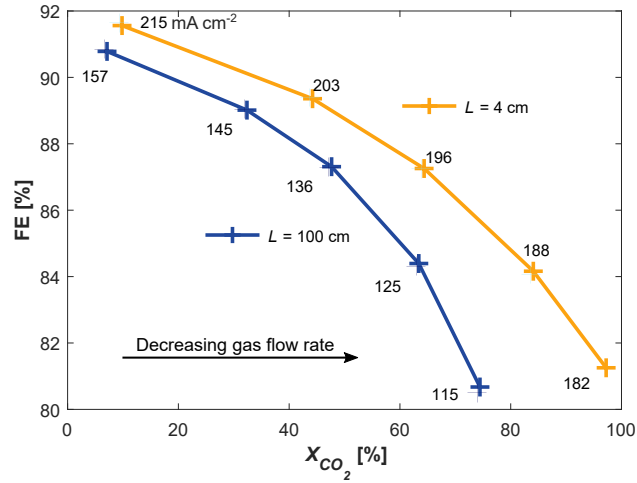


Figure D.10: Faradaic efficiency, FE, as a function of a single pass conversion, X_{CO_2} , at various total current densities, j_{tot} . The blue line represents the long electrolyser with a length, L , of 100 cm. To reach a higher X_{CO_2} , the applied potential was kept constant but the gas flow rate was decreased. The yellow line represents a small-scale counterpart with a length, L , of 4 cm. To reach a higher X_{CO_2} the gas flow rate was adjusted accordingly, that is, decreased by the ratio of the lengths. In both cases, the applied potential was kept unchanged. From this figure follows that small-scale electrolyser can reach higher j_{tot} at the same applied potential. This, however, comes at expense of FE, but the X_{CO_2} is now also improved. Both electrolysers now show similar trend.

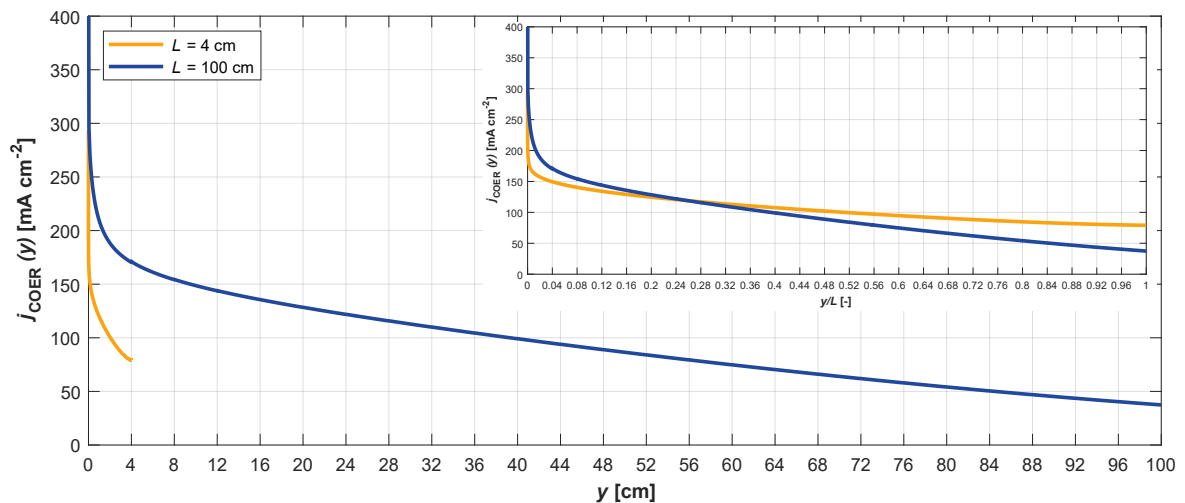


Figure D.11: j_{COER} as a function of electrolyser length, $j_{\text{COER}}(y)$. The figure shows the long electrolyser, $L = 100$ cm, and the short electrolyser, $L = 4$ cm. Both results correspond to $j_{\text{tot}} = 115 \text{ mA cm}^{-2}$. The embedded figure shows $j_{\text{COER}}(y)$ as a function of normalized electrolyser length.

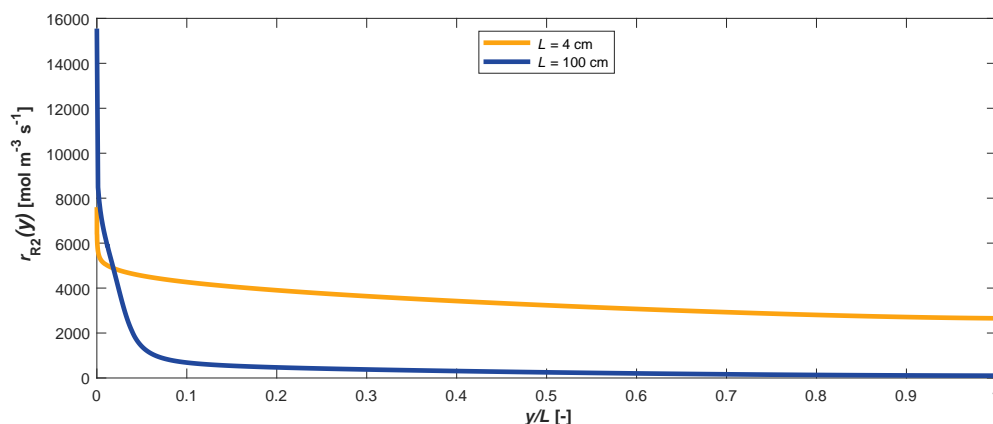


Figure D.12: R2 net reaction rate, r_{R2} , as a function of electrolyser length, $r_{R2}(y)$. The figure shows the long electrolyser, $L = 100$ cm, and the short electrolyser, $L = 4$ cm. Both results correspond to $j_{tot} = 115 \text{ mA cm}^{-2}$. In case of the short electrolyser, $r_{R2}(y)$ slowly linearly decreases which follows from the favorable flux of HCO_3^- ions into the CL (**Figure 4.24**). In case of the long electrolyser, the flux of HCO_3^- ions into the CL rapidly diminishes (**Figure 4.24**). Further downstream the flux of HCO_3^- ions into the CL is almost non-existent. This distribution of HCO_3^- flux leads to the extremely low $r_{R2}(y)$. $\text{CO}_{2(aq)}$ can now contribute a significant part of $r_{R2}(y)$.

D.3.1. Reaching high single pass conversions

Single pass conversion, X_{CO_2} , reaches substantially high values in our model (**Figure 4.20**). However, Kas *et al.*⁶ reports the X_{CO_2} not to surpass 70% (**Figure D.13**).

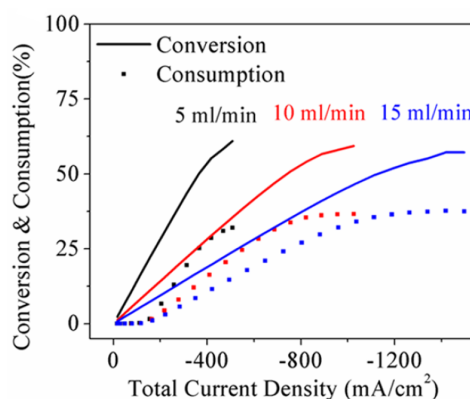


Figure D.13: Single pass conversion, conversion, and consumption of $\text{CO}_{2(aq)}$ in R1, consumption, as reported by the model developed by Kas *et al.*⁶ Flow rate in the figure corresponds to the gas flow rate. Figure adopted from Kas *et al.*⁶

We propose two arguments which can explain this difference in X_{CO_2} . First, if we were to calculate the Re, at which these authors assume the electrolyte to flow, we find that $\text{Re}=8$. In our model of the long and the short electrolyses, we assume the $\text{Re}=200$. We can now use our previous finding which has shown that very low Re results in a significantly higher consumption of $\text{CO}_{2(aq)}$ in R1 (**Figure 4.13**). This means that if we have also operated the electrolyser at very low Re, we would have seen more $\text{CO}_{2(aq)}$ being consumed in R1 and this would result in a lower X_{CO_2} .

Second, and more importantly, Kas *et al.*⁶ assumes the electrolyte feed not to be in the equilibrium with 1 atm of CO_2 . Thus, the authors use an electrolyte which has a significantly lower amount of initially dissolved $\text{CO}_{2(aq)}$. However, we find that $\text{CO}_{2(aq)}$ can act as an important source for COER, especially at high X_{CO_2} (**Table D.1**). This contribution to X_{CO_2} is thus missing in the work by Kas *et al.*⁶

From the definition of X_{CO_2} (Equation 3.95) follows that the dissolved $\text{CO}_{2(aq)}$ entering the electrolyser via the liquid phase, is not accounted for in the calculation of X_{CO_2} . Consequently, we normalize the CO production by an incomplete source of CO_2 . This means that we could eventually reach X_{CO_2} even over 100 %.

Table D.1: Contribution to X_{CO_2} when broken down to the contribution from the gaseous phase and the initially dissolved $\text{CO}_{2,(\text{aq})}$ in the electrolyte. All reported results are taken from the short electrolyser. Since the balance over the CL must close, then, to estimate the contribution of the electrolyte $\text{CO}_{2,(\text{aq})}$ and the gaseous CO_2 to the X_{CO_2} , we can immediately divide amount of CO_2 entering the CL by the amount of CO_2 entering the gas channel. X_{CO_2} is higher than the two separate contributions, because it accounts for $\text{CO}_{2,(\text{aq})}$ lost in R1.

Assumed conversion %	j_{tot} mA cm^{-2}	$\text{CO}_{2,(\text{aq})}$ from the electrolyte entering the CL mol s^{-1}	CO_2 from the gas entering the CL mol s^{-1}	r_{R1} mol s^{-1}	CO produced in COER mol s^{-1}	CO_2 entering the gas channel mol s^{-1}	Contribution to X_{CO_2} from the electrolyte %	Contribution to X_{CO_2} from the gaseous phase %	X_{CO_2} %
160	115	1.91E-07	4.67E-07	1.66E-09	6.56E-07	7.77E-07	24.58	60.10	84.42
120	125	1.85E-07	5.19E-07	2.07E-09	7.02E-07	1.04E-06	17.89	50.14	67.84
80	136	1.80E-07	6.03E-07	2.96E-09	7.80E-07	1.55E-06	11.60	38.80	50.21
50	145	1.70E-07	6.68E-07	4.08E-09	8.34E-07	2.49E-06	6.85	26.88	33.56
10	157	1.49E-07	7.61E-07	6.77E-09	9.03E-07	1.24E-05	1.20	6.14	7.28

D.4. Strategies to improve the performance of long electrolysers

D.4.1. Fluid flow configuration

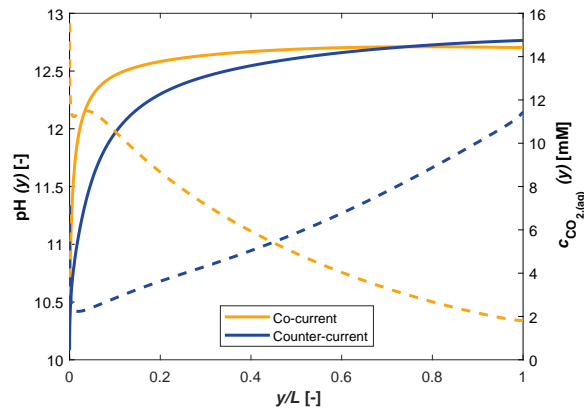


Figure D.14: Bold: pH as a function of the electrolyser length $\text{pH}(y)$. Dashed: $c_{\text{CO}_{2,(\text{aq})}}(y)$ as a function of the electrolyser length, $c_{\text{CO}_{2,(\text{aq})}}(y)$. Profiles are normalized by the electrolyser length, L , which is 10 cm. Both results are at $j_{\text{tot}} = 200 \text{ mA cm}^{-2}$. Electrolyte in both regimes enters at $y/L = 0$. The gas enters at $y/L = 1$ in the countercurrent regime. In the case of the countercurrent regime, we can see a lower rate of $\text{pH}(y)$ increase around the electrolyte inlet which follows from the locally lower $j_{\text{tot}}(y)$. $\text{pH}(y)$ towards the electrolyte outlet, i.e. $y/L = 1$, increases as follows from the combination of depleted electrolyte buffering capacity and increasing $j_{\text{tot}}(y)$. $c_{\text{CO}_{2,(\text{aq})}}(y)$ correlates with the direction in which the gas is fed into the electrolyser. $c_{\text{CO}_{2,(\text{aq})}}(y)$ locally strongly increases around $y/L = 0$ in the countercurrent regime which originates from the initially dissolved $\text{CO}_{2,(\text{aq})}$ supplied by the electrolyte.

D.4.2. Variable catalyst loading

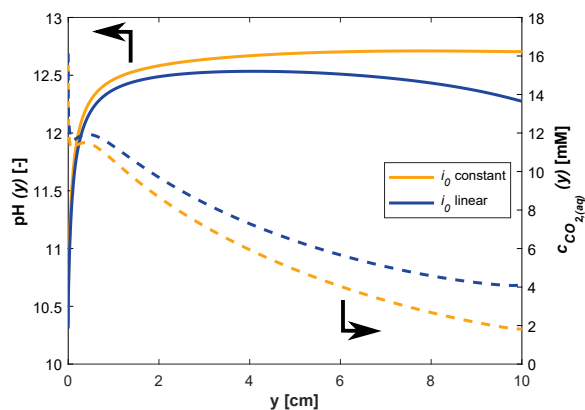


Figure D.15: (a) Bold: pH as a function of the electrolyzer length, $\text{pH}(y)$. Dashed: $c_{\text{CO}_2(\text{aq})}$ as function of the electrolyzer length, $c_{\text{CO}_2(\text{aq})}(y)$. Both results are at -1.16 V vs. RHE . For i_0 constant this corresponds to $j_{\text{tot}} = 205 \text{ mA cm}^{-2}$. For i_0 linear this corresponds to $j_{\text{tot}} = 177 \text{ mA cm}^{-2}$. In case of the i_0 linear, the lower j_{tot} leads to a lower production of OH^- ions, this then decreases the pH. Lower pH reduces the consumption of $\text{CO}_2(\text{aq})$ in R1 and enables the $c_{\text{CO}_2(\text{aq})}$ reach higher values.